Ultrafast imaging of nonlinear terahertz dynamics in semiconductors

by

Charles E. Jensen

A thesis submitted in partial fulfillment of the requirements for the degree of

Master of Science

Department of Physics

University of Alberta

Abstract

Ultrafast terahertz (THz) microscopy is an emerging field of research that leverages the imaging of picosecond electric field transients to explore free carrier responses from a near-field perspective. This thesis presents the first effort made to use an electro-optic imaging system to probe the subpicosecond changes in electron conductivity that can be induced by the intervalley scattering of conduction band electrons. Intervalley scattering will lower the overall conductivity in n-doped $In_{0.53}Ga_{0.47}As$ thin films. The lowering of conductivity (and the subsequent enhancement of transmission) is herein referred to absorption bleaching. A near-field approach is necessary to properly understand intervalley scattering, since subpicosecond modulations in material conductivity give rise to a rectified THz pulse. Imaging in the near-field enables us to capture the rectified components of the transmitted electric fields before diffraction occurs. The presence of the rectified components is emphasized by looking to the time-domain evolution of the total electric field transmitted electric fields.

We use a standard open aperture z-scan to characterize absorption bleaching in n-doped $In_{0.53}Ga_{0.47}As$ thin films. This is the baseline from which a near-field electro-optic imaging z-scan is compared. Contrasting the baseline measurements to the results of the imaging z-scan, we find that the energies calculated from the ultrafast imaging z-scan follow nearly the

same trend as the benchmark measurements. This marks the first evidence that a near-field electro-optic measurement of a transmitted THz electric field contains signatures which indicate THz-induced intervalley scattering is occurring in $In_{0.53}Ga_{0.47}As$ thin films.

In previous work, it was shown that the rectification of THz pulses can produce an asymmetric waveform, which, when integrated does not converge to zero. For the first time, we experimentally measure this on sub-picosecond time-scales by using a near-field electro-optic sampling system to measure THz waveforms in the near-field. Intense THz pulses passing through only a semi-insulating InP wafer are shown to possess no net asymmetry, whereas intense THz pulses passing through a negatively doped $In_{0.53}Ga_{0.47}As$ epilayer grown on a lattice matched InP substrate are shown to diverge significantly. To interpret this result, we invoke a dynamic Drude model of conductivity that can be used to simulate nonlinear transmission. We find that the simulation is able to generate integrated THz electric fields that share similar features to those from experiment. This indicates that intervalley scattering is a material process that is capable of inducing subpicosecond changes in the transmitted electric field of intense THz pulses.

Preface

I hereby declare that except where specific reference is made to the work of others, the contents of this dissertation are original and have not been submitted in whole or in part for consideration for any other degree or qualification in this, or any other University. This dissertation is the result of my own work and includes nothing which is the outcome of work done in collaboration, except where specifically indicated in the text.

Charles E. Jensen

I would like to dedicate this thesis to my wonderful friends and family. It is through your support that I get the opportunity to explore God's creation at the highest of level.

Acknowledgements

It has been an immense pleasure working under my supervisor, Dr. Frank Hegmann. Thank you for your enthusiasm and patience. Frank has an incredible way of explaining physics that makes difficult concepts easy to grasp. I am grateful for the conversations we've had, and for the opportunity to work in one of the best THz research groups in the world.

I want to thank David Purschke for all of the time he spent tutoring me in the ways of THz research. Thank you for being the first to volunteer to edit anything I write, and always trying hard to provide constructive feedback. You are an inspiration for many of us in the lab, and I deeply appreciate all of your support.

Thank you to all of the summer students which I have had the pleasure to work with. Chenxi, thank you for helping me take endless waveforms, and teaching me that if I can find something here, China has their own version of it already. Dan, your thoughtful conversations surrounding a wide variety of topics is greatly appreciated. Chris and Kaylee, thank you for your company and help whenever I needed an extra hand. Thank you Chris for the many hours of thought-provoking conversation. I will deeply miss having you as an office mate. Kameron, your commenting skills are borderline magical, and have helped me immensely in fitting my near-field data to the dynamic Drude model.

Working with Beipei and Dave Fortin has been a real privilege. Thank you for helping me design a working sample holder, as well as machining stage components and providing top-notch programming advice. You are a talented technicians, and I couldn't have done this without your support.

I would like to thank Ayesheshim for his help before he left. Your advice about taking time to do alignment was on-point. Haille Sharum, thank you for leaving such neat and tidy notes. Your hard work in setting up the imaging system is very much appreciated, and I couldn't have made this much progress without it.

Special thanks to my lab mates Mary, Cameron, Vedran and Alex, who always lent an ear to hear my thoughts on various topics.

Finally, I would like to thank my parents for their constant support, my brother for encouraging me to keep going, and my friends Jimmy, Ketty, Rachel, Sydney, Ben, Keith and Waison for reminding me that there's more to life than work.

Table of contents

List of figures

List of tables

Chapter 1

Introduction

The imaging of spatio-temporal characteristics of physical phenomena has origins dating back to the Sallie Gardner experiment conducted by Eadweard Muybridge in 1878 [1]. In this experiment, the mechanics of a galloping horse were demonstrated by putting together a series of still-frame images taken as a horse galloped along a track. This provided irrefutable proof that horses do not gallop with both front hoofs outstretched. The connection between the Muybridge experiment and the thesis at hand, is that time-domain imaging is still being used today, albeit in different bands of the electromagnetic spectrum. In this thesis, we will restrict our discussion to time-resolving the electric fields of intense pulses of light within the terahertz (THz) band of the electromagnetic spectrum. These pulses typically have frequencies between 0.1 and 3 THz, as shown in Fig. 1.1.

Nearly 100 years after the Muybridge experiment, the first images in the THz region of the electromagnetic spectrum were taken [2]. The utility of imaging in this regime was recognized for applications in measuring the spectral fingerprints of gases with permanent dipole moments, contrasting bone from fatty tissue, and uncovering dangerous objects that would be otherwise concealed at optical wavelengths [2]. In 1995, coherent time-domain detection of pulsed THz radiation was used to measure the spatio-temporal evolution of THz pulses, as they transmitted through a semiconductor integrated circuit, and a leaf at various stages of drying [3]. By raster

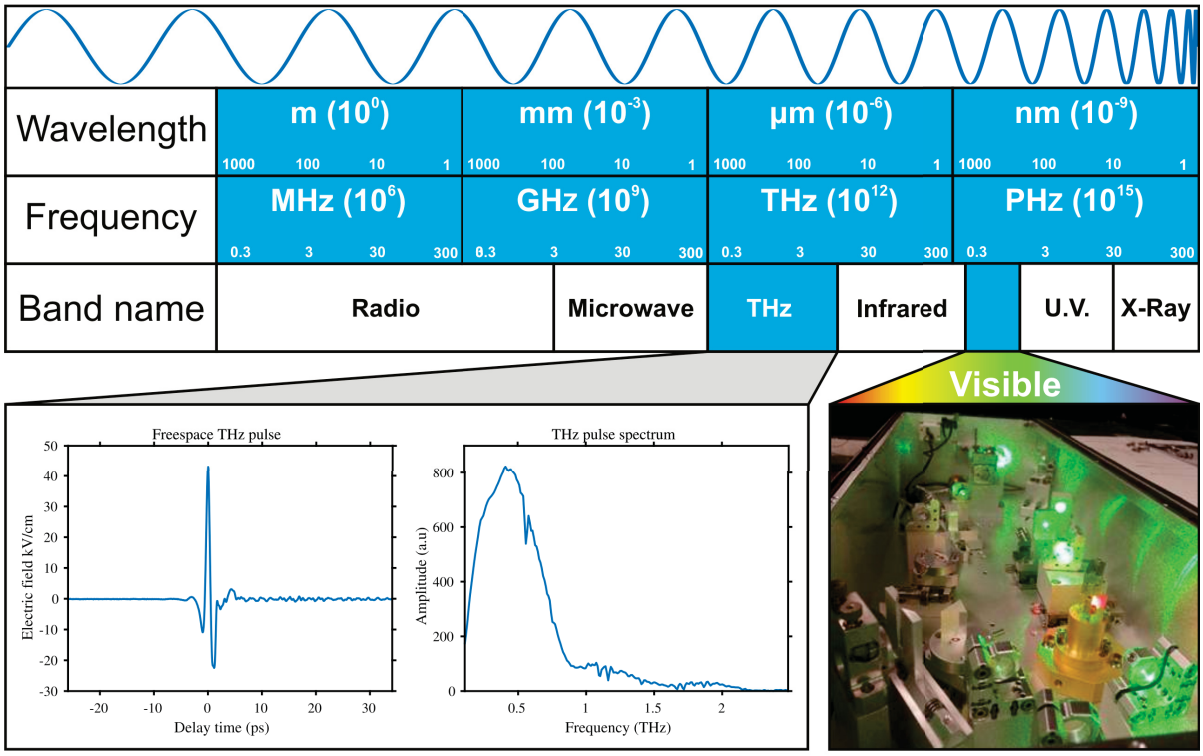

Fig. 1.1 The electromagnetic spectrum, with emphasis on the THz and visible spectral bands. A standard THz pulse is shown on the bottom left, alongside it's Fourier amplitude spectrum.

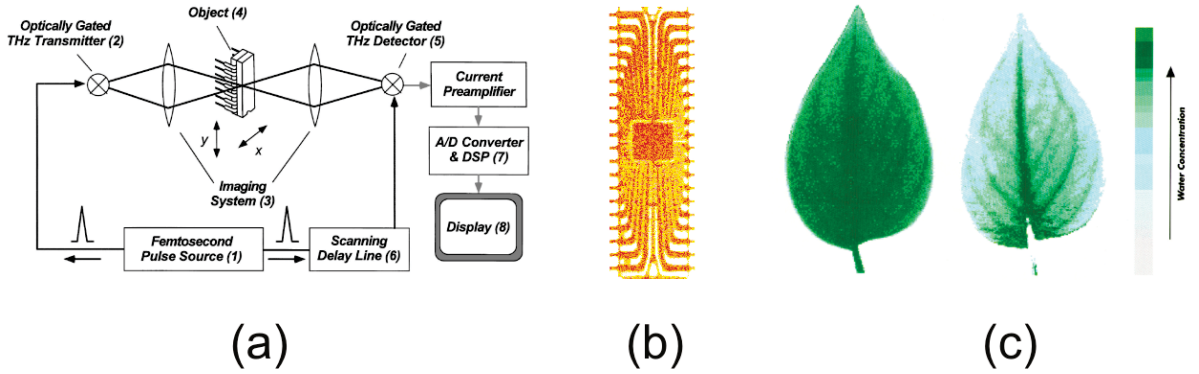

Fig. 1.2 Key results from Ref. [3]. (a) Diagram of the raster scanning method used by Hu and Nuss to create THz images. (b) THz image of an integrated circuit. (c) THz images of a drying leaf. The left image of (c) was taken close to the time that the leaf was picked, and the right image was taken 48 hours later. (Adapted from [3])

scanning samples across the focus of a THz pulse (Fig. 1.2 (a)), the time-domain transmission waveforms could be measured pixel-by-pixel. Thus, a movie of THz transmission through a sample could be reconstructed. By Fourier transforming the time-domain waveforms, the spectral images could be easily calculated, and are used to highlight regions of high reflectivity (Fig. 1.2 (b)), as well as regions of high absorption (Fig. 1.2 (c)).

In recent years, THz researchers are taking advantage of electro-optic techniques to perform time-domain imaging on sub-picosecond time scales [4, 5], far surpassing the millisecond time scales of Sallie Gardner's day. The spatial resolution of THz imaging systems have also improved, as near-field microscopes are able to achieve $\lambda/600$ at 0.1 THz using electro-optic methods [6], $\lambda/1000$ by coupling THz pulses to atomic force microscopes [7], and even atomic resolution by coupling THz pulses to scanning tunneling microscope tips [8, 9]. In the present work, we are interested in using an electro-optic THz imaging system to capture the spatial and temporal profiles of a THz pulse as it emerges through various semiconductors. Our reason for doing so is to extend the work on near-field THz imaging into the realm of high-field electron transport in n-doped $In_{0.53}Ga_{0.47}As$, which, to our knowledge, no one has done before. Doing this we hope to identify intervalley scattering of conduction band electrons as the physical

origin of the near-field dipole radiation patterns seen in previous work [10].

In June of 2009 it was demonstrated that a transient enhancement of transmission (absorption bleaching) occurs when an intense few-cycle THz pulse passes through photoexcited GaAs [11]. The mechanism driving absorption bleaching was found to be intervalley scattering of conduction band electrons, which built on the work done by Razzari et al. [12]. Razzari et al. showed that n-doped InGaAs samples exhibit a similar transient absorption bleaching induced solely by the presence of intense THz pulses [12]. Expanding on these results near the surface of the sample, Ayesheshim K. Ayesheshim used a microwave coaxial probe to measure the THz waveforms near the surface of a sample identical to the one used by Razzari et al. [10]. Although bandwidth limited by the electronic probe, Ayesheshim measured transmitted THz waveforms, and through simulations, he was able to connect intervalley scattering to the rectification of THz pulses that traversed n-doped $In_{0.53}Ga_{0.47}As$ thin-films. Using an electro-optic imaging system to chieve subpicosecond time resolution of the transmission of intense THz pulses, we hope to overcome the bandwidth limitation of the microwave coaxial probe. Furthermore, the rectification of intense THz pulses was not seen in the far-field THz waveforms since low-frequency components diffract very quickly from the surface of transmission [10]. This makes a near-field approach absolutely necessary in our present effort to capture the rectified components of an intense THz pulse passing through an n-doped $In_{0.53}Ga_{0.47}As$ epilayer on subpicosecond timescales.

In Chapter 2 of this thesis, we discuss the principles behind generating and detecting THz radiation. Chapter 3 connects the theoretical framework from Chapter 2 to the electro-optic imaging system. Chapter 4 builds the dynamic Drude model of the intervalley scattering of conduction band electrons, establishing the connection between material conductivity and transmissivity. In Chapter 5 we present the results of benchmark open-aperture z-scans, and use these as a comparison for the results of an ultrafast imaging z-scan. This is the first demonstration that an electro-optic imaging system can be a novel method for characterizing the

field-dependent behavior of nonlinear transmission. In chapter 5 we also use a near-field electro-optic sampling system to observe the subpicosecond rectification of an intense THz pulse. We then present the results of a first attempt to use a dynamic Drude model of conductivity to explain the rectification of intense THz pulses. In Chapter 6 conclusions and outlook are presented.

Chapter 2

Generation and detection of intense THz pulses

2.1 Generating THz pulses

2.1.1 Generation Principle: Optical rectification

Maxwell's equations can be combined in such a way as to provide the classical description of light and its propagation through matter. The derivation of the following wave equation is relegated to Appendix B.4. For now, let's proceed with analyzing the nonlinear wave equation in order to get a feel for the components that are responsible for the generation of intense THz pulses.

In general, the wave equation presented in eqn. 2.1 encompasses the linear ($\mathbf{P}^{(1)}$) and nonlinear effects of a macroscopic polarization ($\mathbf{P}_{\mathrm{NL}}$) induced by an external electric field ($\mathbf{E}$) that is propagating at the speed of light (c)

$$\nabla^2\mathbf{E} - \frac{1}{c^2}\frac{\partial^2\mathbf{E}}{\partial t^2} = \underbrace{\mu_o\frac{\partial^2\mathbf{P}^{(1)}}{\partial t^2}}_{\text{Linear term}} + \underbrace{\mu_o\frac{\partial^2\mathbf{P}_{\mathrm{NL}}}{\partial t^2}}_{\text{Nonlin. term}}. \tag{2.1}$$

By bringing over the linear term onto the left hand side, and noting that $(1+\chi^{(1)}) = \varepsilon^{(1)}$ and $\mathbf{P}^{(1)} = \varepsilon_o \chi^{(1)} \mathbf{E}$, we arrive at the nonlinear wave equation for an electric field in matter

$$\nabla^2 \mathbf{E} - \frac{\varepsilon^{(1)}}{c^2} \frac{\partial^2 \mathbf{E}}{\partial t^2} = \mu_o \frac{\partial^2 \mathbf{P}_{\mathrm{NL}}}{\partial t^2}. \tag{2.2}$$

On the left hand side, the only alteration that occurs is the coefficient $1/c^2$ becoming $\varepsilon^{(1)}/c^2$. This signifies that to first order the presence of matter slows down the propagation of light by a factor $c \to c/\sqrt{\varepsilon^{(1)}} = c/n$. Furthermore, the right hand side behaves mathematically as a source term that is characterized by the nonlinear polarization effects induced by the applied electric field. At weak fields, only the linear term is important, and the right hand side is effectively zero. In the high field limit we can expand the nonlinear terms into higher order polynomials of ever increasing electric field order

$$\mathbf{P}_{\mathrm{NL}} = \frac{1}{2}\varepsilon_o \chi^{(2)} \mathbf{E}(r,t)\mathbf{E}(r,t) + \frac{1}{6}\varepsilon_o \chi^{(3)} \mathbf{E}(r,t)\mathbf{E}(r,t)\mathbf{E}(r,t) + \ldots \tag{2.3}$$

where, $\chi^{(n)}$ is the n^{th}-order susceptibility tensor. In a noncentrosymmetric material, the lowest-order contribution to the polarization is second order in electric field strength ($\mathbf{E}^2$ term in eqn. 2.3) [13]. Optical rectification is a second order nonlinearity, and so noncentrosymmetric materials like ZnTe and stoichiometric $LiNbO_3$ (sLN) are used to generate THz pulses. Since the second order term is the dominating term in the nonlinear expansion of eqn. 2.3, the nonlinear polarization can be approximated as as

$$P_{\mathrm{NL}} \approx \frac{1}{2}\varepsilon_o \chi^{(2)} |E(r,t)|^2. \tag{2.4}$$

Equation 2.4 will be used as the source term in eqn. 2.2. Considering the case of a noncentrosymmetric material experiencing a pulsed electric field having a carrier frequency ω_o, and a Gaussian envelope characterized by the duration τ,

$$E(t) = E_o e^{-t^2/\tau^2} \cos(\omega_o t) \tag{2.5}$$

the nonlinear polarization takes the form of a rectified field [13, 14]. Another way to phrase this is that there exist amplitudes centered on zero frequency, which is easily seen by substituting eqn. 2.5 into eqn. 2.4, as,

$$P_{\mathrm{NL}} = \frac{E_o^2 \varepsilon_o \chi^{(2)}}{4} \left(\underbrace{e^{-2t^2/\tau^2}}_{\text{Zero centered}} + \underbrace{e^{-2t^2/\tau^2} \cos\left(2\omega_o t\right)}_{\text{Freq. doubled}} \right). \tag{2.6}$$

Therefore in noncentrosymmetric media, there is a transient, rectified polarization that occurs. This is a key element in generating radiation through optical rectification, as it can be shown that far away from the transient polarization, an electric field can be detected with the form [14–16]

$$E \propto \frac{\partial^2 P_{\mathrm{NL}}}{\partial t^2} \tag{2.7}$$

and the THz electro-magnetic radiation comes from the rectified component of this

$$E_{\mathrm{THz}} \propto \frac{\partial^2 P_{\text{Zero centered}}}{\partial t^2} \propto \left[\frac{16t^2}{\tau^4} - \frac{4}{\tau^2} \right] e^{-2t^2/\tau^2}. \tag{2.8}$$

Figure 2.1 shows the progression from optical stimulus, to THz pulse. Note that in eqn. 2.8 the coefficient is a quadratic polynomial, and that it contains roots at $\pm\tau/2$. Between these roots, the function is negative, giving rise to the negative electric fields seen in Fig. 2.1 (d).

2.1.2 Phase matching with tilted-pulse fronts

MgO doped (0.6%*mol*) stoichiometric lithium niobate (sLN) is used as the THz generation medium for three main reasons: a large band gap, a high optical damage threshold and a large electro-optic coefficient. The large band gap of sLN ensures that there is a low occurrence of multi-photon absorption during the THz generation process, which helps to minimize the excitation of free charge carriers and the subsequent THz absorption [17]. sLN also possesses a large electro-optic coefficient which serves to boost the efficiency of converting optical pulses

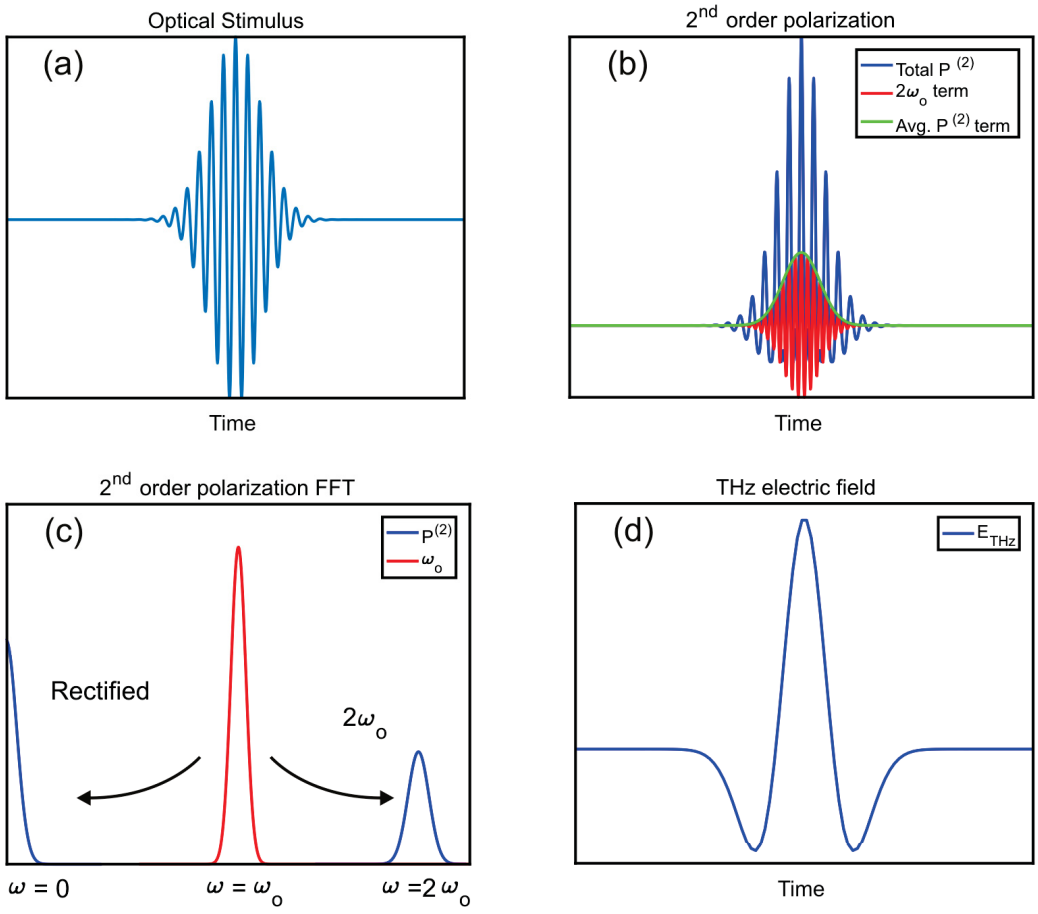

Fig. 2.1 Highlighting the progression from optical stimulus to THz pulse. (a) An optical stimulus with the gaussian profile and center frequency ω_o. (b) The components of the second order polarization from eqn. 2.4 in the time-domain. (c) Showing the frequency domain polarization function of eqn. 2.4. d) The time-domain THz waveform described by eqn. 2.8.

into THz radiation [5, 17, 18]. Finally, the introduction of MgO doping enhances the optical damage threshold [10].

The primary concern in using sLN to generate THz pulses is the mismatch in velocity between the optical stimulus group velocity (v_{vis}^{gr}) and the generated THz phase velocity (v_{THz}^{ph}), ie, $v_{vis}^{gr} \neq v_{THz}^{ph}$. Consequently, when an optical pulse is tightly focused onto a sLN crystal, THz generation is restricted to the case that the beam waist of the focused optical pulse is smaller than the distance it travels in one optical pulse duration, ie,

$$w < v_{vis}^{gr} \tau \tag{2.9}$$

where w is the optical beam waist, and v_{vis}^{gr} is the group velocity of the optical pulse, and τ is the optical pulse duration [19]. As the pulse moves forward, and optical rectification occurs, a Cherenkov-like cone of THz radiation is emitted [20, 21], which proves to be suboptimal for efficient generation of THz pulses in a collinear geometry [19]. In Fig. 2.2 (a), a diagram of the Cherenkov-like cone is shown, highlighting the relationship between the phase velocity of the THz pulse and the optical group velocity. v_{vis}^{gr} is larger than v_{THz}^{ph}, and with some simple geometry, it's easy to show that

$$\cos(\theta_C) = \frac{v_{THz}^{ph}}{v_{vis}^{gr}} \tag{2.10}$$

The velocity mismatch causes the generated THz pulse to slowly propagate behind the optical stimulus, and therefore constructive interference only occurs along a Cherenkov-like cone.

Hebling et al. were the first to overcome the velocity mismatch problem in 2002, through use of a tilted pulse-front scheme [19]. The main idea of a tilted-pulse front is shown in Fig. 2.2 (b), where the aim is to avoid focusing the optical stimulus, and instead achieve velocity-matching by adding a slope to the pulse front. THz generation is optimized this way, since tilting the optical pulse front creates an extended surface of THz generation, so long as the new pulse front is tilted to the Cherenkov angle θ_C [19]. Fig. 2.3 demonstrates how we create tilted

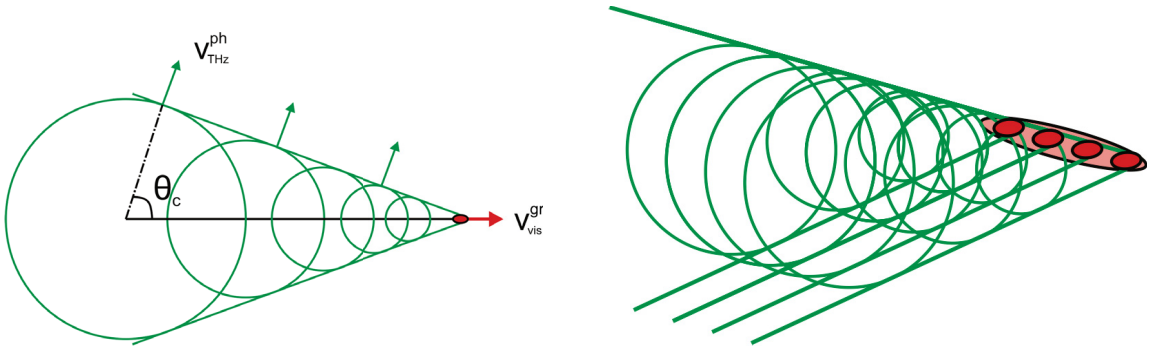

(a) (b)

Fig. 2.2 THz generation from focused pulse and tilted pulse front. (a) Tightly focused optical pulse creating a THz Cherenkov cone, resulting from the velocity mismatch between optical and THz wavelengths. (b) Schematic of a tilted-pulse front slanted at the optimal angle for THz generation. Each point on the tilted-pulse front acts as a source similar to (a).

optical pulse fronts of optical excitation in sLN. Light pulses are directed onto a diffraction grating, and the pulse front is tilted according to the path length difference of the first diffraction maximum ($m = 1$), which depends on the angle of incidence (α), the diffraction angle (β) and the diffraction grating period (d)

$$\sin(\alpha) + \sin(\beta) = \frac{m\lambda}{d}. \tag{2.11}$$

Let us label the diffracted spot size d_2. Doing so allows us to write the pulse-front-tilt-angle as

$$\tan(\gamma_2) = \frac{d\,(\sin(\alpha) + \sin(\beta))}{d_2}. \tag{2.12}$$

After the pulse has been tilted, it then passes through a lens. The lens serves to collect the diffracted pulse front, and image it onto the sLN

$$\tan(\gamma_3) = \frac{d_2}{d_3}\tan(\gamma_2), \tag{2.13}$$

where d_3 is the pulse width on the sLN, and γ_3 is the new pulse-front tilt angle. The demagnification ratio is defined as d_2/d_3. Finally, this pulse front arrives at the sLN. since the pulse is

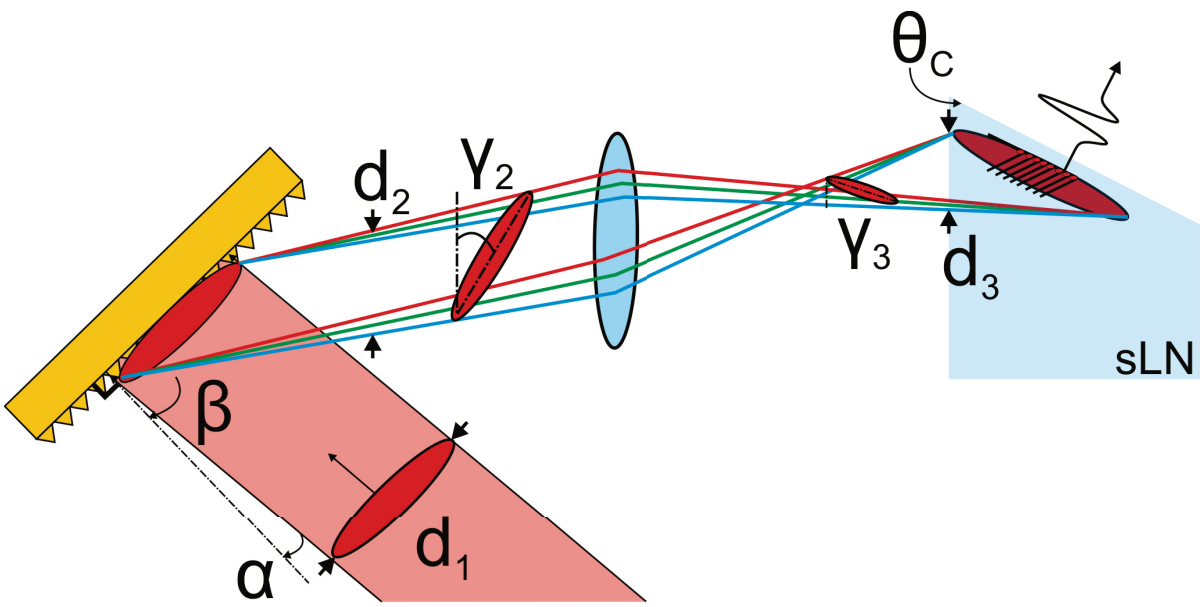

Fig. 2.3 Schematic of the tilted pulse-front scheme used to generate intense THz pulses. The red beam indicates a 50fs pulse of light with wavelength components centered around 800nm. The blue crystal is $LiNbO_3$, and the black arrow indicates the direction of THz propagation.

tilted, one side of the pulse front arrives sooner than the other. This means that the index of refraction for sLN will retard the progression of the early arriving side first, compressing the pulse front by a factor of $1/n_O$. The tilt angle (γ_4) inside the sLN crystal is thus given by

$$\tan(\gamma_4) = \frac{\tan\gamma_3}{n_O} \tag{2.14}$$

where, n_O is the index of refraction for sLN at $800nm$ (≈ 2.26).

Now, working back from what we know, the cut angle of the sLN is made to match the Cherenkov angle, $\theta_C = 63^o$ meaning that $\gamma_4 = 63^o$, from which it is possible to work out the incident angle required for the optimal tilted pulse front [10].

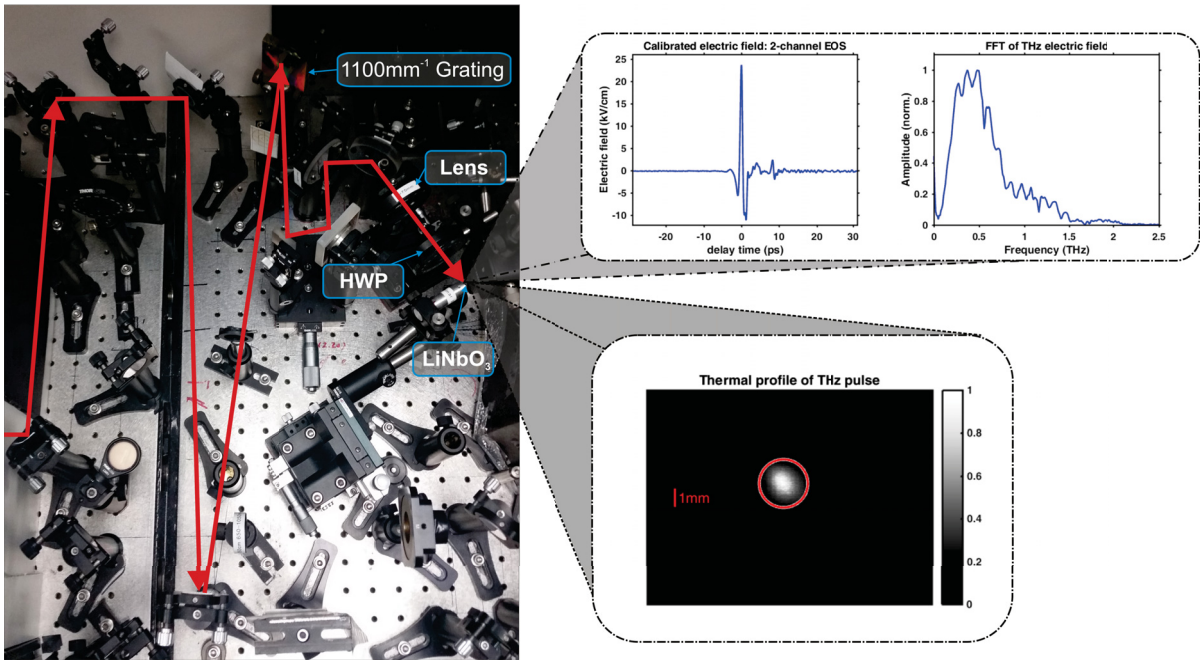

Fig. 2.4 Picture of the THz generation path. 50fs pulses (red beam path) are directed towards a 1100mm^{-1} difraction grating. The pulse front is tilted, by the grating and imaged onto the $LiNbO_3$ crystal. A half wave plate (HWP) is used to rotate the electric field polarization from horizonal to vertical. Inset is a typical THz pulse generated by optical rectification in the $LiNbO_3$. The time-domain waveform is accompanied by the frequency spectrum, centered near 0.5 THz. A typical thermal profile of a THz pulse is show. This image is captured using a pyroelectric array, and demonstrates a typical 1/e^2 diameter of 2 mm.

2.1.3 Table-top diagram

At peak performance, using a grating with a groove density of $1100mm^{-1}$, this system is capable of producing free space THz pulses with a 1.78ps duration with frequencies centered at 0.5THz. With pulse energies of $1.2\mu J$, the peak electric fields can be as high as 100kV/cm (c.f. eqn. B.3).

2.2 Principles of single channel detection

Single channel detection is the mechanism we employ to resolve the time evolution of an electric field in a near-field fashion. Whether it is through electro-optic imaging, or single

channel lock-in detection, the principles remain the same. In general what we're attempting to do is turn the electric field of a THz pulse - which changes on picosecond (ps) timescales - into the intensity variation of an optical pulse that photodetectors can measure (such as photodiodes or CCD arrays).

To begin, let's start off with the more familiar touchstone of Malus' law. Malus' law informs us of the intensity of light that exits linear polarizers, having an angle between their transmission axes of θ. The output intensity is given by

$$I_{\text{out}} = I_{\text{in}} \cos^2(\theta) \tag{2.15}$$

where I_{out} is the exiting intensity and I_{in} is the intensity incident to the first polarizer. Crossed polarizers ($\theta = \pi/2$) do not allow any intensity to pass through, while uncrossed polarizers ($\theta = 0^o$) will permit all incident intensity to pass through. In single channel detection, the polarizers are crossed. The input polarizer has its transmission axis oriented vertically, allowing vertically polarized light to pass through. The output polarizer (analyzer) is oriented with its transmission axis in the horizontal orientation, allowing only horizontally polarized light to pass through. Theoretically, no light should exit this assembly. However, by inserting an electro-optic crystal such as GaP or ZnTe between the crossed polarizers, an electric-field-dependent modification to eqn. 2.15 arises (remember, $\theta = \pi/2$)

$$I_{\text{out}} = I_{\text{in}} \cos^2\left(\frac{\pi}{2} + \frac{\Delta\Phi}{2}\right) = I_{\text{in}} \sin^2\left(\frac{\Delta\Phi}{2}\right), \tag{2.16}$$

where, $\Delta\Phi = \phi_{\text{int}} + \phi_{\text{ext}}$ is the total phase shift induced by the birefringence of the electro-optic crystal. In practice we use the electric field-dependent nature of the phase change $\Delta\Phi$ to control the amount of light exiting the cell. Turn up the electric field applied to the electro-optic crystal in Fig 2.5, and you increase the output intensity.

The property of electro-optic crystals that is sensitive to the applied electric field is the index of

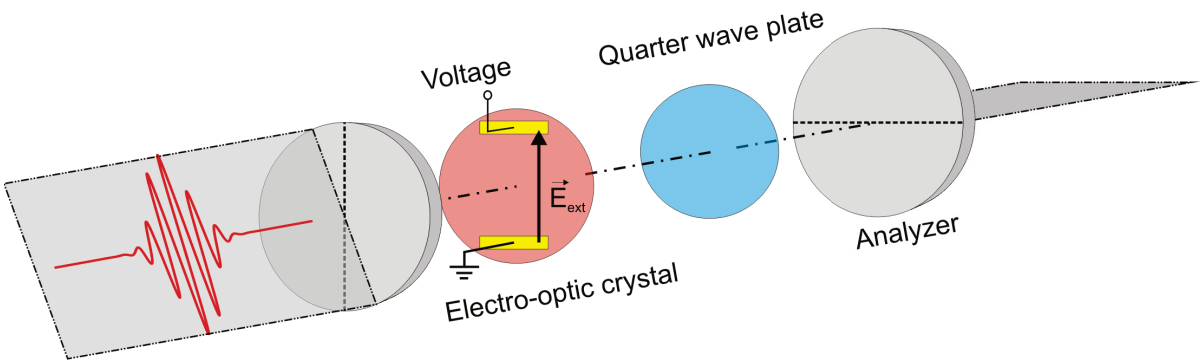

Fig. 2.5 A schematic of a Pockel cell. A voltage is applied to the electro-optic crystal between 2 crossed polarizers. The electric field changes the birefringent properties of the electro-optic crystal, providing control over how much light leaves the cell. With the quarter wave plate absent, the arrangement is in E^2-mode. With the quarter wave plate present, the assembly is in E-mode.

refraction along one axis. The birefringence of a crystal comes from the sum of two parts: the intrinsic birefringence associated with the structure of the crystal (ϕ_{int}), and the birefringence induced by an external electric field (ϕ_{ext}) which comes from the linear electro-optic effect. For crystals like ZnTe, there is little-to-no intrinsic birefringence, and so $\phi_{\text{int}} = 0$. Typically ZnTe is oriented so that the [110] axis is aligned to the direction of the THz propagation, and so the externally induced phase shift is proportional to the applied electric field. This can be expressed as [16, 22]

$$\phi_{\text{ext}} = \frac{\pi d n_o^3 r_{41}}{\lambda} E_{\text{ext}}. \tag{2.17}$$

where d is the crystal thickness, n_o is the crystal index of refraction for an optical pulse, E_{ext} is an applied external electric field, λ is the vacuum wavelength of the sampling pulse and r_{41} is an electro-optic coefficient (represented using compressed notation [13]) that comes from the electro-optic tensor.

The nature of the phase changes mentioned above is heavily dependent on the orientation of the electro-optic crystal chosen, and the strength of the applied electric field (E_{ext}). For example,

choosing a [110] oriented ZnTe crystal, eqn. 2.16 becomes

$$I_{\text{out}} = I_{\text{in}} \cos^2\left(\frac{\pi}{2} + \frac{\pi d n_o^3 r_{41}}{2\lambda} E_{\text{ext}}\right), \tag{2.18}$$

which, for small electric fields gives an output intensity that is proportional to the square of the external electric field

$$I_{\text{out}} \approx I_{\text{in}} \left(\frac{\pi d n_o^3 r_{41}}{2\lambda} E_{\text{ext}}\right)^2 - \mathscr{O}\left(E_{\text{ext}}^4\right). \tag{2.19}$$

Given the quadratic sensitivity to the presence of an electric field, we refer to this assembly as E^2-mode. Figure 2.6 (a) shows how the quadratic approximation results in an E^2 transmission function for small electric fields. The strong dependence on the applied electric field makes E^2-mode an excellent choice for overlapping a THz pulse with a near infrared sampling pulse. However, the added contrast comes with a price - insensitivity to the positive or negative nature of the applied electric field. We will need an additional optical element in order to produce intensity modulations that are proportional to the external electric field.

If we could introduce a phase shift in eqn. 2.18 that moves the ouput intensity function to either the left or right by $\pi/4$, we could shift the output intensity function towards a linear detection regime. A quarter wave plate does the trick if we insert it between the electro-optic crystal and the analyzer. This results in an extra $\pi/4$ term appearing in eqn. 2.18, as

$$I_{\text{out}} = I_{\text{in}} \cos^2\left(\frac{\pi}{2} + \frac{\pi}{4} + \frac{\pi d n_o^3 r_{41}}{2\lambda} E_{\text{ext}}\right). \tag{2.20}$$

Thus, when expanded into its Taylor series, eqn. 2.20 has the form

$$I_{\text{out}} = I_{\text{in}} \left(\frac{1}{2} + \frac{\pi d n_o^3 r_{41}}{2\lambda} E_{\text{ext}} + \mathscr{O}\left(E_{\text{ext}}^3\right)\right) \tag{2.21}$$

which demonstrates a linear dependence on the external electric field. Fig. 2.6 (b) shows the linear regime of detection, stemming from eqn. 2.20 and eqn. 2.21.

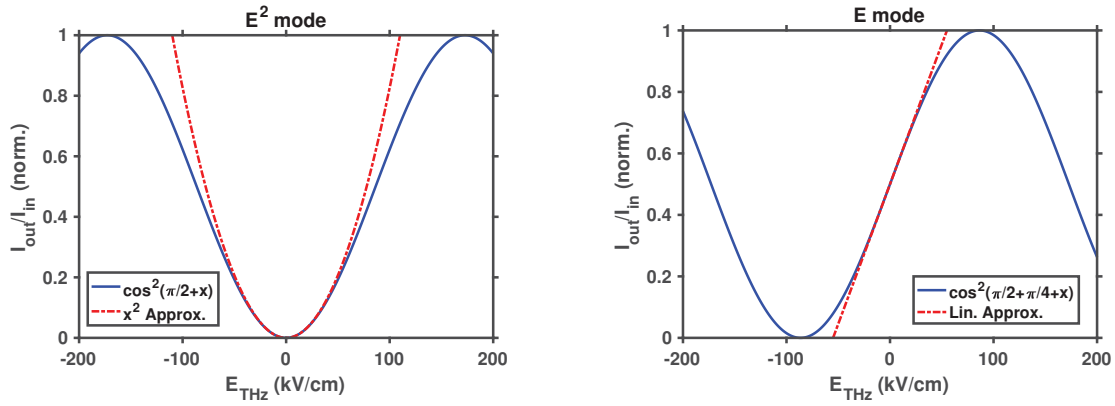

(a) (b)

Fig. 2.6 E^2-mode and E-mode intensity modulation comparison. (a) The modulated intensity of the same system in E^2 mode. Constants used are from a ZnTe electro-optic crystal, where, $r_{41} = 4 \times 10^{-12} m/V$, $n_o = 2.85$, $\lambda = 800nm$ and $d = 500\mu m$ [16]. (b) The modulated intensity from a single-channel electro-optic detector in the E-mode configuration, using the same optical constants as in (a). The only difference between E-mode and E^2-mode is the insertion of a quarter wave plate.

The linear form of eqn. 2.21 allows for sensitivity to the positive and negative nature of an external electric field. Taking the linear terms, and assuming that the electro-optic crystal is experiencing an instantaneous electric field brought about by a THz pulse of light E_{THz}, we can see that the intensity exiting the polarizer system is given by

$$I_{\mathrm{out}} = I_{\mathrm{in}} \left(\frac{1}{2} + \frac{\pi d n_o^3 r_{41}}{2\lambda} E_{\mathrm{THz}} \right). \tag{2.22}$$

Some simple rearranging gives us

$$\frac{I_{\mathrm{out}} - \frac{I_{\mathrm{in}}}{2}}{I_{\mathrm{in}}} = \left(\frac{\pi d n_o^3 r_{41}}{2\lambda} \right) E_{\mathrm{THz}}. \tag{2.23}$$

which is an important equation that we will use to calculate calibrated electric fields in later chapters. The left hand side is telling us that by comparing the input sampling beam intensity to the output intensity, we can measure a quantity proportional to a THz electric field. Experimentally we can measure these intensities by either using a gated intensified imaging system such

as the PicoStarHR, or 2 photodiodes (one measuring I_{in}, and another measuring I_{out}).

There are two reasons for why we can sample different parts of a THz electric field. The first is that each THz pulse is a facsimile of all other THz pulses coming from a source. Another way to say this is that optical rectification produces phase-stable pulses of light, which allows us to sample the electric field of many pulses. The second reason is that near-infrared pulses can have durations on the order of 50fs, which is very short in comparison to the 1ps duration of THz pulses. Therefore, by delaying the arrival time between a near-infrared pulse and a THz pulse, we can change the electric field that surrounds the near-infrared pulse. Figure 2.7 shows how this works in a step-by-step series of images. A digitally controlled delay stage is used to vary the image pulse arrival time. With these stages, we can introduce delays on the scale of $1\mu m$, which corresponds to timescales on the order of $7fs$. We can then iterate the sampling scheme (step, measure, step, measure... etc.), and stitch together the time-domain electric field of a THz pulse of light.

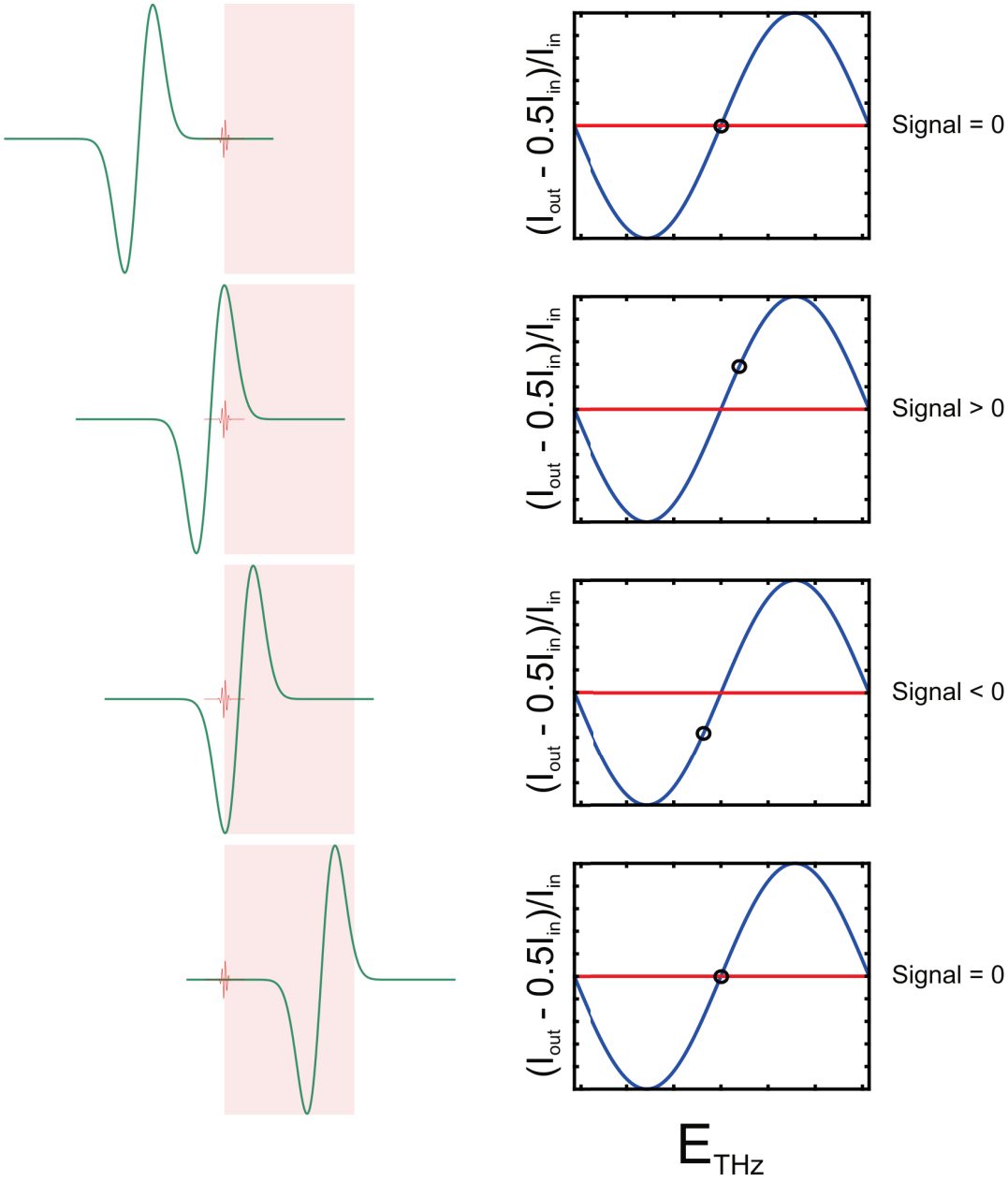

Fig. 2.7 Sketch of how the near-infrared pulse (red) can be delayed to sample different parts of synchronized, phase-stable THz pulses (green) using a single-channel electro-optic detector in E-mode. The figure starts at the top where the near-infrared sampling beam arrives before the THz pulse. Proceeding downwards, the THz pulse is sampled at later and later times, until eventually there is no THz pulse to sample. The functions plotted on the right show how eqn. 2.20 modulates the output intensity proportional to the incident THz electric field. This is seen as the circle moving along the blue curve.

Chapter 3

Ultrafast imaging

3.1 Ultrafast imaging system

This section is dedicated to explaining how we use the PicoStar HR imaging system to perform ultrafast imaging of intense THz pulses. It will draw on the theory presented in the previous chapters, focusing on how we obtain the intensities required to perform near-field single channel electro-optic imaging . We begin by introducing the layout of the system, and follow that up with the physical properties of the imaging system. This paves the way for the discussion of time-domain imaging, and the efforts made to optimize the setup.

3.1.1 Tabletop diagram

Fig. 3.1 shows the key components of the electro-optic imaging system. The blue line represents an 800nm, 50fs pulse coming from the Legend amplification system. This line is called the imaging line because these are the pulses that are destined to arrive at the intensified imaging system. The imaging line is attenuated by a polarizer-half wave plate-polarizer combination, which can attenuate the imaging line from powers of $650mW$ down to less than $1mW$. This is useful, because it minimizes the effects of exciting charge carriers in the samples we aim to probe (Appendix B.3).

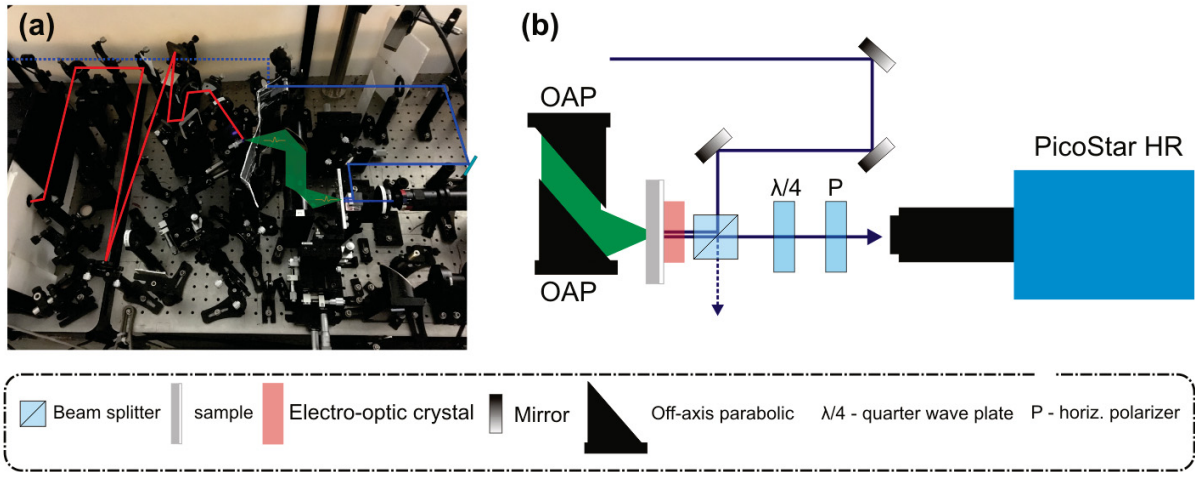

Fig. 3.1 Picture and diagram of electro-optic imaging system. (a) Picture of the electro-optic imaging system, with an overlay of some key components. The blue line represents the imaging beam path, and the red line is the THz generation path. (b) Schematic of the electro-optic imaging system.

The red line in Fig. 3.1 indicates the path that another 800nm 50fs pulse follows (this time, powers on the order of $2W$), which we will refer to as the generation path. This path is dedicated to generation of THz pulses through optical rectification in lithium niobate (Chapter 2.1).

The overall picture for this setup is to have the imaging path fall parallel to the THz propagation direction. As the imaging beam is reflected off of the sample surface, it passes through an electro-optic crystal twice: once on entry, and again upon reflection from the sample surface. At the precise moment of reflection, the THz pulse should encompass the imaging beam, much like Fig. 2.7. Reflecting off of the surface, and then passing through the quarter wave-plate and the linear polarizer, the intensified imaging system can record the modulated imaging beam.

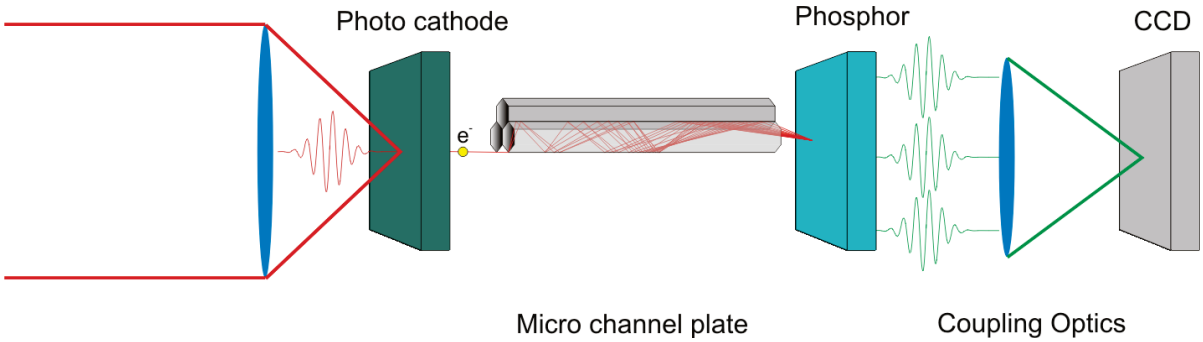

Fig. 3.2 Sketch of key components within an ICCD system. The system has a photo cathode that launches electrons into a micro channel plate (MCP). The large number of secondary electrons generated in the MCP are deposited onto a phosphor, which illuminates the coupling optics of a CCD array.

3.1.2 Properties of the intensified imaging system

To perform ultrafast imaging of intense THz pulses, we use an intensified charged coupled device (ICCD) camera system. Figure 3.2 shows the basic construction of an ICCD system. The PicoStar HR ICCD is specially designed for use in systems operating at repetition rates near 110 MHz, fundamentally limited by the open/close frequency of a photo cathode [23]. The photo cathode is sensitive to photons near the infrared band of the electromagnetic spectrum. Figure 3.3 shows this in plots of the quantum efficiency and the photo sensitivity. The quantum efficiency is simply the percentage of photons that are converted into photo electrons, ie,

$$\mathrm{QE} = \frac{\#\text{Photo electrons generated}}{\#\text{Photons incident}}. \tag{3.1}$$

From Fig 3.3 we can see that for 800nm light, the photo cathode has a quantum efficiency of nearly 6%. The photo cathode acts much like a shutter, when a large voltage is applied (U_{cathode}). U_{cathode} quickly accelerates the photoelectrons from the cathode into a micro channel plate (MCP). The MCP creates secondary electrons when a primary electron collides with the walls of the micro channel. The number of secondary electrons generated (and hence, the Gain) is dependent on the number of collisions that occur. The Gain is controlled by the voltage placed across the MCP (U_{MCP}), this voltage drives electrons into further collisions with the micro

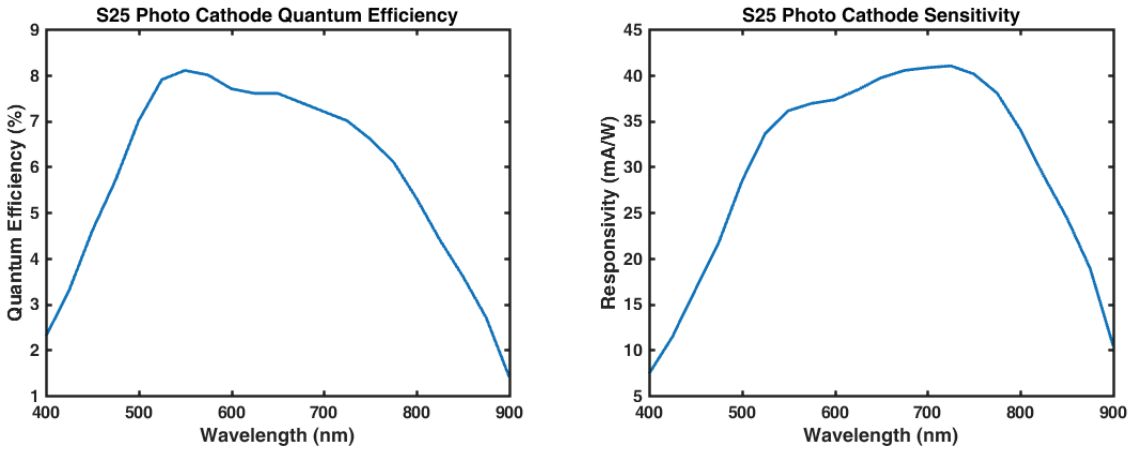

(a) (b)

Fig. 3.3 (a) Quantum efficiency and (b) sensitivity of the ICCD photocathode in the visible spectrum. This data is provided by the Picostar HR Camera Test Certificate.

channels. Once the signal has been amplified by this gain process, the electrons are pulled onto a phosphor, which illuminates the CCD through coupling optics.

The photo cathode is synchronized to the Legend amplifier, such that photoelectrons are only accelerated into the micro channels when the optical pulse arrives at the photo cathode. Fig. 3.4 shows a diagram of the timing sequence for the triggering of the photo cathode. For reference, we trigger the cathode off of the exit Pockel cell from within the Legend amplifier. With this reference in time, a picosecond delay unit is used to delay the shutter according to the path length required to travel from the Legend to the ICCD. Looking again to Fig. 3.4, the "1000ps gate" signal is shifted by delay time introduced by the picosecond delay unit. Once the photo cathode is synchronized to the legend amplifier, the ICCD then integrates over a predetermined number of pulses ("CCD exposure" in Fig. 3.4). After the CCD is finished integrating, the CCD is read into the DaVis software, where images can be saved in ASCII format.

Recall the step-by-step concept in Fig. 2.7. If we delay the imaging beam, in order to sample different parts of a THz waveform, there is a chance that we may delay the pulse so much that

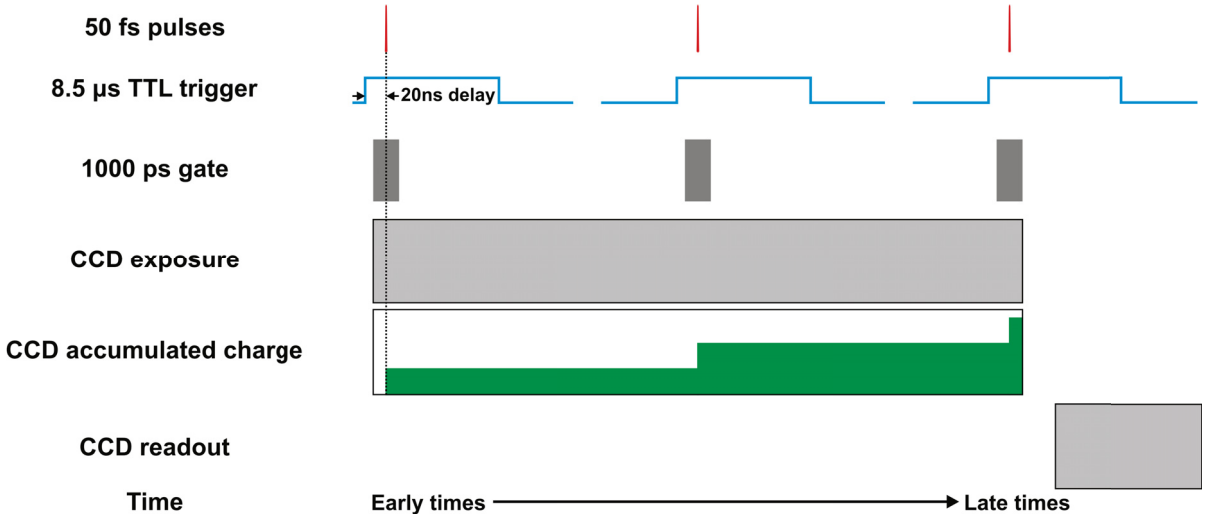

Fig. 3.4 Schematic of the image acquisition process. 50fs pulses are captured within a 1000ps wide gate that is triggered by the rising edge of an 8.5μs TTL signal synchronized to the fs pulses. A controllable delay allows us to center the window on the fs pulses. Once the 50fs pulse is captured, the ICCD system converts that intensity into an accumulated charge on a CCD, which is integrated over the CCD exposure time. After the exposure is over, the CCD readout begins. This image is not to scale, as the time between fs pulses is 1ms.

the imaging pulse is no longer synchronized to the imaging system. To look into the possibility of this, we measured the window over which imaging is possible. Starting off at times before the optical pulse arrives, and stepping through many delay times, we could visualize the onset of the imaging pulse. By integrating these images, we can measure the total intensity, which allows us to plot Fig. 3.5. Figure 3.5 shows that there is roughly a 1ns window over which we can safely introduce an optical delay. This corresponds to approximately 6 inches of mechanical delay, which is large compared to the 0.15mm required to sample a THz pulse. Therefore, we should not expect the imaging delay line to compromise the synchronization of the imaging system and the Legend amplifier.

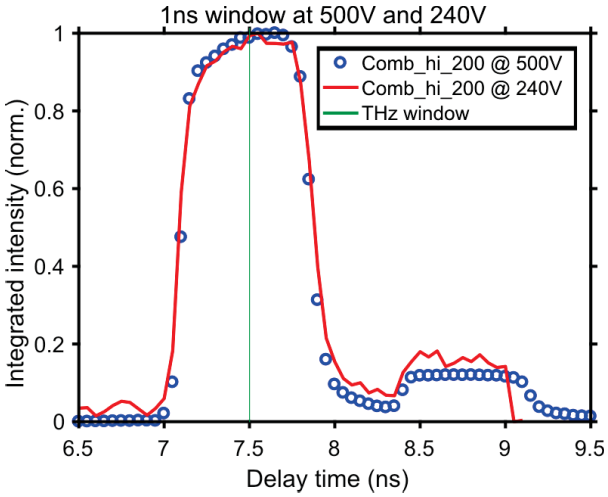

Fig. 3.5 Gate window at two different intensifier voltages (red line and blue circles). The green line is the range of delay we need to sample a THz pulse. For such small delays, the window will be approximately flat.

3.1.3 Image analysis

Using everything presented thus far, we can now perform ultrafast imaging of intense THz pulses. We accomplish this by bringing together the Picostar ICCD system and the Pockel-cell configuration from Chapter 2.2. Recall eqn. 2.23, where we saw that in order to acquire an image of a THz pulse we need a background image with no THz present (I_{in}) and a signal image with the THz modulation present (I_{out}).

Normally, to accommodate the fact that a CCD can't read negative counts, an offset is applied to the signal images . This transforms the signal intensities $I_{\text{out}} \rightarrow I_{\text{out}} + \text{Offset}$, which implies the need to subtract off this offset manually [24], changing eqn. 2.23 to read

$$\frac{(I_{\text{out}} + \text{Offset}) - I_{\text{in}} - \text{Offset}}{I_{\text{in}}} = \left(\frac{\pi d n_o^3 r_{41}}{2\lambda}\right) E_{\text{THz}}. \tag{3.2}$$

In an effort to reduce the time between capturing a signal image and the corresponding background image, a Thorlabs SH05 beam shutter was used to block the THz source. Using a TTL communication system controlled by a National Instruments DAQ board, the background

image is taken, the shutter is opened, and the signal image is taken. Once the images are taken, a delay line is moved and the process begins anew. The problem with this scheme is that there isn't any control over which images get an offset, and which ones don't. We are forced to let all images acquire an offset, which sends $I_{\text{out}} \rightarrow I_{\text{out}} + \text{Offset}$ and $I_{\text{in}} \rightarrow I_{\text{in}} + \text{Offset}$. In the numerator of eqn. 2.23, we can see that the offsets will cancel, while in the denominator we need to a priori subtract off the offset, giving us the new reduction equation

$$\frac{(I_{\text{out}} + \text{Offset}) - (I_{\text{in}} + \text{Offset})}{(I_{\text{in}} + \text{Offset}) - \text{Offset}} = \left(\frac{\pi d n_o^3 r_{41}}{2\lambda} \right) E_{\text{THz}} \tag{3.3}$$

For clarity, whenever an "Offset" is added to an image during image acquisition, it is contained within brackets. Whenever an offset is subtracted during the data analysis, the "Offset" term has been left outside of brackets.

An example of image analysis using eqn. 3.2 is shown in Fig. 3.6. Figure 3.6 (a) shows an image taken when the THz pulse overlaps the optical pulse. $(I_{\text{out}} + \text{Offset})$. Figure 3.6 (b) shows an image of the background image (I_{in}). Using eqn. 3.2 on Fig. 3.6 (a) and Fig. 3.6 (b), the modulation ratio image is calculated, and shown in Fig. 3.6 (c). Figure 3.6 (d) shows how a cross section of an image evolves during image analysis. Equation 3.3 from now on will be referred to as the modulation ratio. It is important to recall Fig. 2.6 when discussing the modulation ratio, as an electric field strength greater than $\sim 100 kV/cm$ will correspond to electric fields that put the electro-optic detector into a regime where the modulation ratio will decrease as the electric field is increased - defeating the purpose of the detector.

Now, by performing pixel-by-pixel subtraction of the background image (I_{in}) and the signal image (I_{out}), we can calculate a THz-induced modulation for a given time step. Doing this for many time steps, we can produce an entire movie. The Matlab code used to perform these calculations is in Appendix A. The code generates a 3-D array of images that is ordered in time. This makes it very easy to Fourier transform the time axis, resulting in the ability to construct frequency domain images.

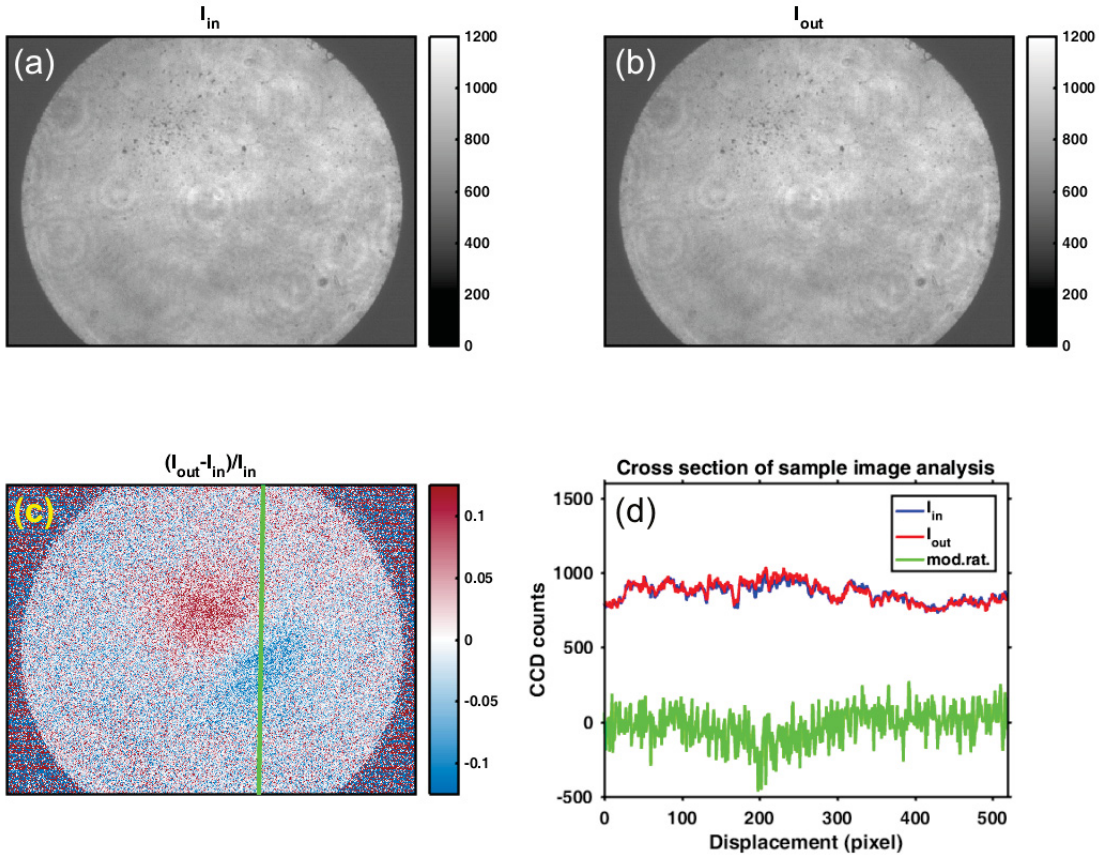

Fig. 3.6 Analysis of imaging data. (a) Image of un-modulated intensity captured by the ultrafast imaging system (I_{out}) in the E-mode configuration. (b) A picture of the THz-modulated intensity (I_{out}). (c) A still-frame image of the modulation ratio calculated using eqn. 3.3, the images in (a) and (b), and an offset of 400 counts. (d) A cross section of the calculation performed in panels (a)-(c). The modulation ratio is scaled by a factor of 2000 so as to make it visible on these scales.

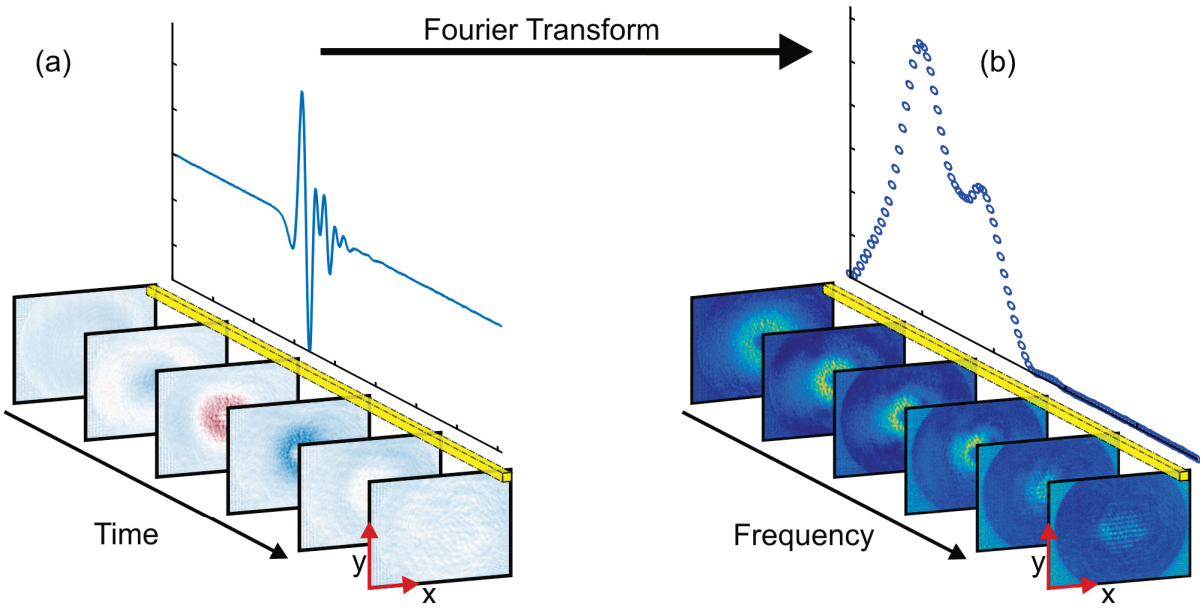

Fig. 3.7 Diagram of frequency domain images. (a) A 3D matrix containing time-ordered images of a THz pulse emerging through a 0.5mm thick, semi-insulating Si wafer using the E-mode configuration. From the time-ordered data set, we can extract a vector (yellow bar), and perform a fast Fourier transform (FFT) of this vector. (b) The spectral amplitudes are calculated from the FFT, and deposited into a new 3D matrix, maintaining the (x,y) coordinate of the vector.

The concept behind frequency domain imaging is expressed in Fig. 3.7. Frequency domain imaging is performed by extracting time-ordered vector from a time-domain 3-D matrix, and fast Fourier transform it. Keeping track of the row/column from which the time vector came, it is then possible to construct a 3-D, frequency ordered array of the amplitude spectrum. Having access to this ability is extremely useful in performing sub-wavelength imaging of intense THz-pulses [5, 6, 25, 26], but is not the main focus of the present work. In the next two pages, space is given to clearly present a time-domain series of images and the respective frequency-domain images. Fig. 3.8 shows a series of time-domain images, capturing snapshots of the electric field of a THz pulse (red-to-blue color) as it emerges through an $In_{0.53}Ga_{0.47}As$ thin film doped to a concentration of $n_c = 2 \times 10^{17} cm^{-3}$. Here we only show steps of 1ps, but the complete image set uses 100fs time-steps. Each image is analyzed according to eqn. 3.3, since the data was acquired using a mechanical shutter. The color bars of Fig. 3.8 demonstrate the modulation

ratio of each image. The system is set up in the E-mode configuration, which provides the ability to distinguish positive electric fields from negative electric fields. From the THz images we can extract a 1-D time-domain waveform by averaging over a small area in each time step, indicated by the green circle shown at 0ps in Fig. 3.8. By Fourier transforming the time-axis, the image set shown in Fig. 3.9 is constructed. The 1-D amplitude spectrum is gathered by means identical to the waveform extraction, except this time applying the averaging to the 3-D matrix of Fourier amplitudes. The red circle overlaid on the 0.2THz image highlights the area averaged to acquire the spectrum shown in the bottom right of Fig. 3.9.

So far we have outlined the mechanism that allows us to measure the spatial characteristics of the electric field of an intense THz pulse. It is now appropriate to compare the peak electric fields of an electro-optically imaged THz pulse, with those attained using a pyroelectric array, and conventional two-channel EOS.

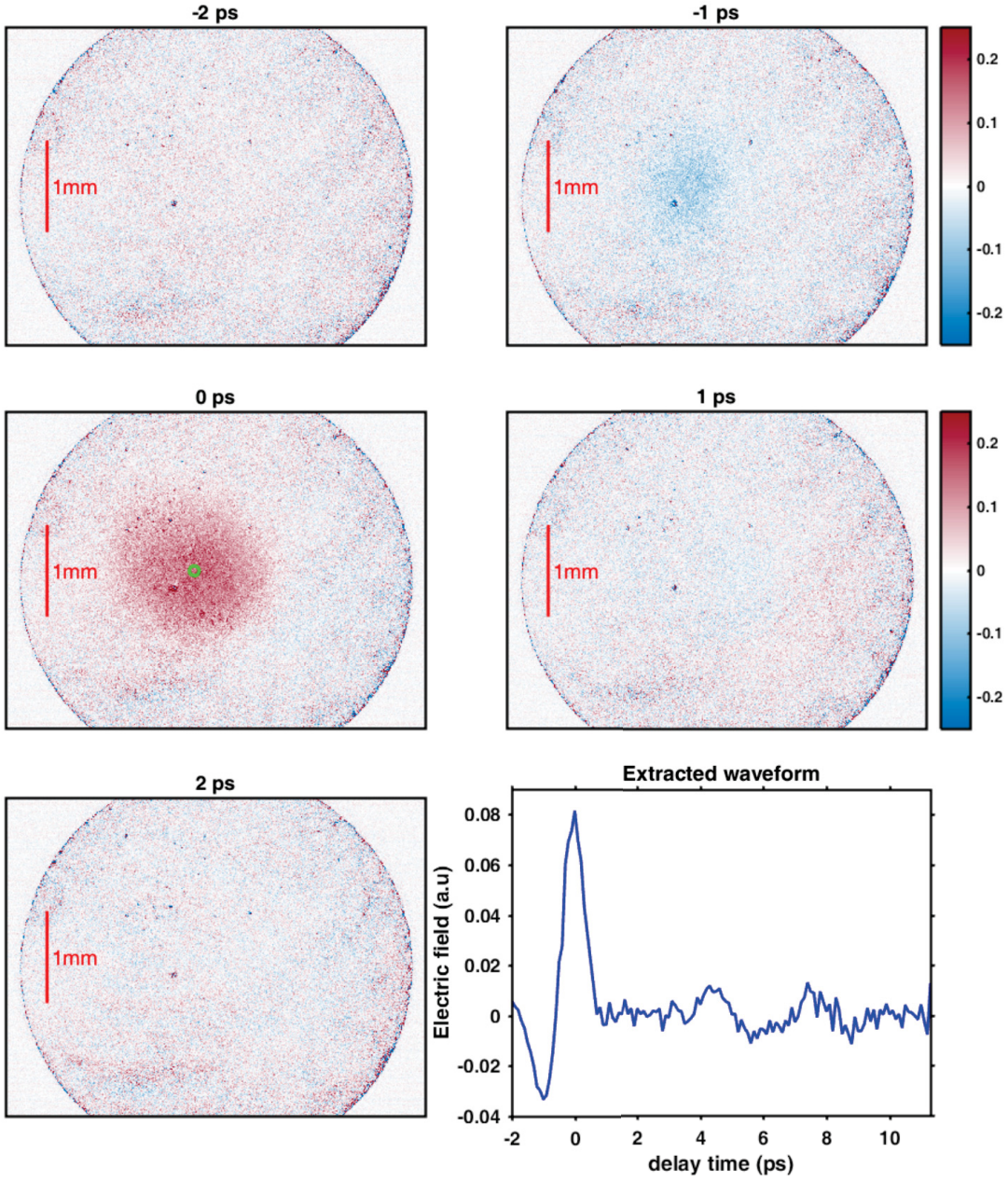

Fig. 3.8 Time-series of THz images taken in E-mode. A THz pulse is transiting an n-doped InGaAs epilayer in this time-series. The green circle at time 0ps indicates the region from which the waveform of the bottom right panel was extracted. The actual data set has 134 of such images, spaced at 100fs time-steps.

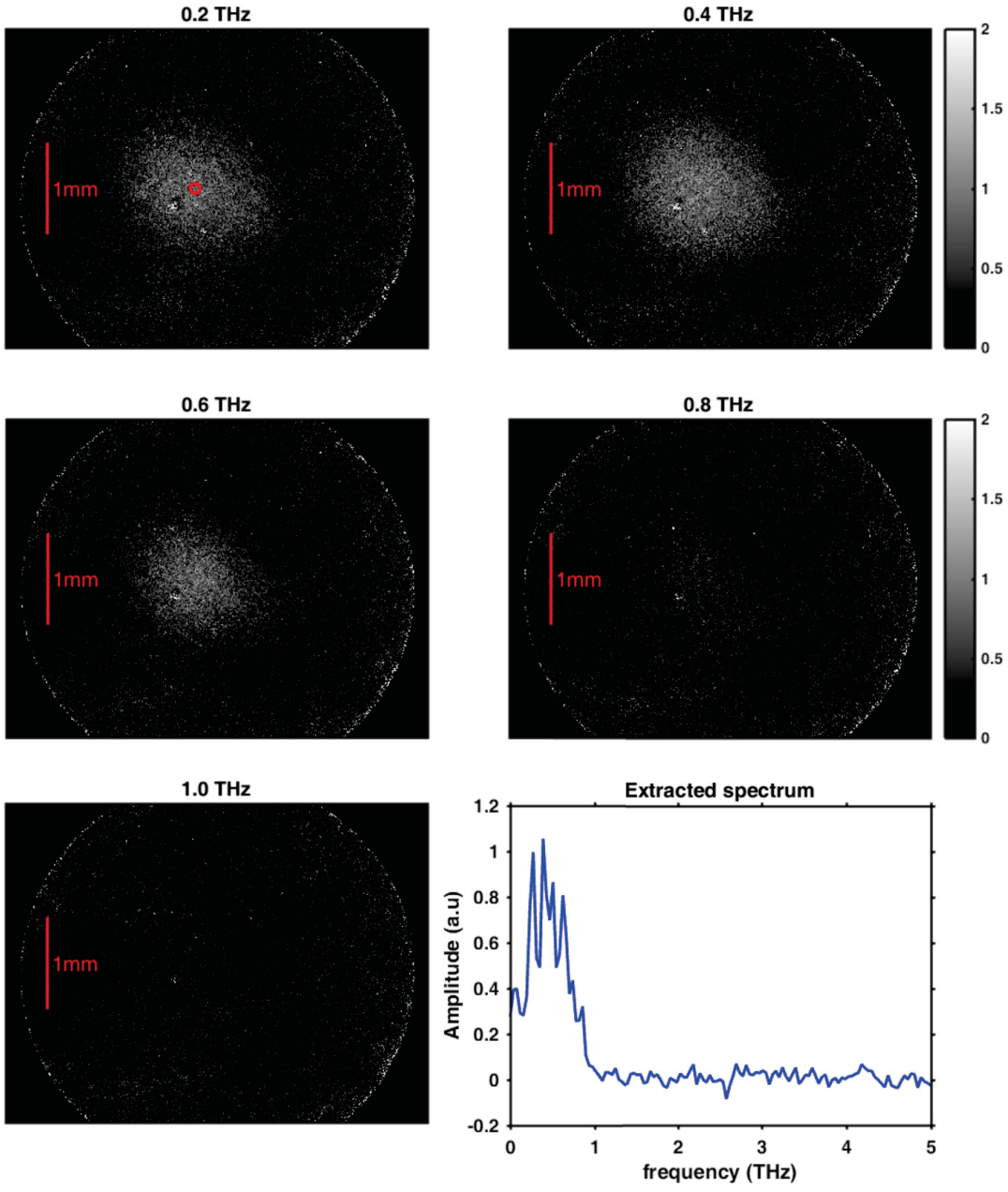

Fig. 3.9 Fourier amplitudes of the THz movie from Fig. 3.8. The red circle indicates the region from which the amplitudes of the bottom right panel were extracted. This area is identical to the area inside the green circle in Fig. 3.8.

3.2 THz electric field calibration

Having the ICCD system in place, and the data processing laid out, we can now measure waveforms using the electro-optic imaging system. There are two alternative methods of characterizing the peak electric field of a THz pulse. The first method of calibration uses a two-channel electro-optic sampling (EOS) system. In a two-channel system, the intensity difference between horizontal and vertical polarizations is used to calculate a modulation ratio that is proportional to the THz electric field. The modulation ratio of this system is given by [18]

$$\frac{I_x - I_y}{I_x + I_y} = \frac{2\pi n_o^3 r_{41} t_{GaP} L}{\lambda_o} E_{\mathrm{THz}} \tag{3.4}$$

where, I_x and I_y are the intensities of the x and y components of the sampling beam, $n_o = 3.2$ is the index of refraction of the electro-optic crystal at the sampling wavelength $\lambda_o = 800nm$, $L = 300\mu m$ is the thickness of the electro-optic crystal, $r_{41} = 0.88pm/V$ is the electro-optic coefficient of the electro-optic crystal, $t_{GaP} = 0.46$ is the Fresnel transmission coefficient for the electro-optic crystal at $1THz$, and E_{THz} is the THz electric field strength. Equation 3.4 has been derived for an arbitrary electro-optic crystal in Appendix B.2 [22]. Figure 3.10 contains a plot of a THz electric field calibrated using the two-channel technique, having been transmitted through an n-doped $In_{0.53}Ga_{0.47}As$ thin film with a carrier concentration of $n_c = 2 \times 10^{17} cm^{-1}$. The many peaks of the amplitude spectrum shown in Fig. 3.10 are the result of multiple beam interference that occurs as the primary transmitted beam interferes with the first reflection from within a sample. The peak modulation ratio is measured to be 0.074, indicating a peak electric field of $23.7kV/cm$.

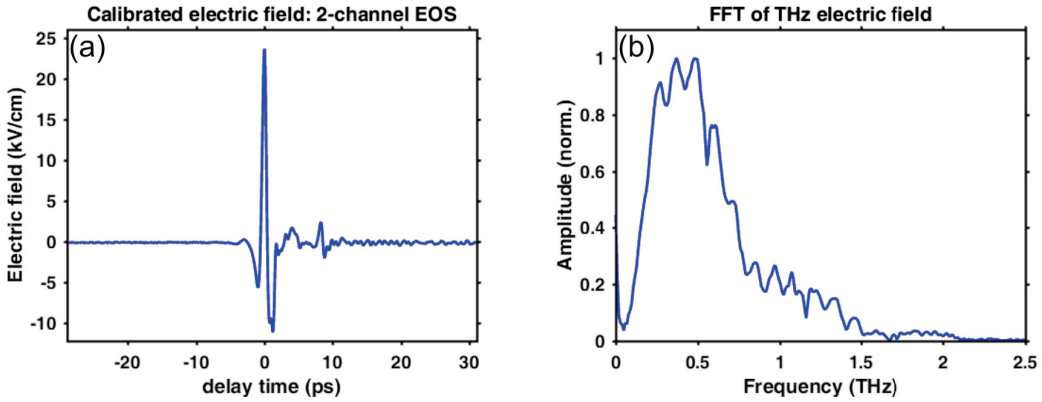

Fig. 3.10 Time and frequency domain plots of THz pulse calibrated to eqn. 3.4. (a) A THz waveform measured using two-channel EOS, and calibrated using eqn. 3.4. This calibration measures a peak electric field of $23.7 kV/cm$. (b) The normalized amplitude spectrum of the THz pulse shown in a.

Alternatively, one may opt to measure a waveform using two-channel EOS, and scale it to the peak electric field calculated from the THz intensity profile, which can measured using a pyroelectric array. The peak THz field in this case is given by

$$|E_{THz}^{peak}| = \sqrt{\frac{4E}{\pi^{3/2} c \varepsilon_o w^2 \tau}} \tag{3.5}$$

where E is the pulse energy measured from a pyroelectric detector, w is a width parameter that comes from fitting the THz intensity profile to the Gaussian in Appendix B.1, $\tau = 1 ps$ is the pulse duration, c is the speed of light in vacuum, and ε_o is the free space electric permittivity. On the same day the waveform above was taken, the THz pulse energy was measured to be $1 \mu J$, and an image was taken of the THz intensity profile using pyroelectric array (Fig. 3.11). A Gaussian surface was fit to this intensity profile, and shows a $1/e^2$ diameter of $2.1218 mm$. This indicates that $w = 0.1.06 mm$, and reveals a peak electric field of $155 kV/cm$.

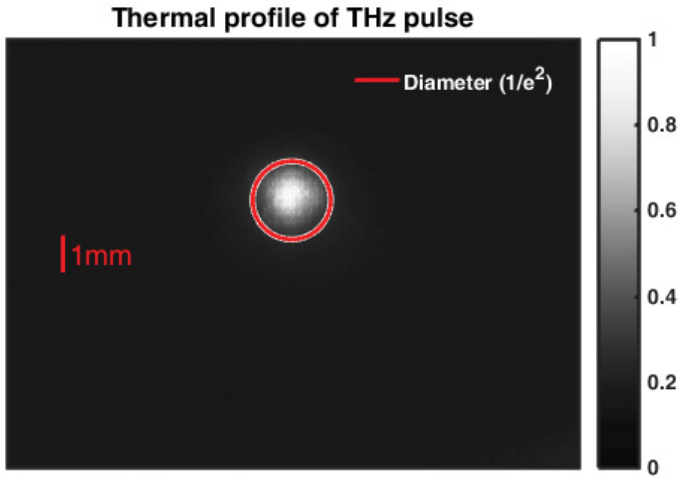

Fig. 3.11 Normalized thermal profile of THz pulse. The best-fit $1/e^2$ diameter for this image was 2.12 mm, as shown by the red circle. With energy of $1\mu J$, the peak electric field from this is 155kV/cm.

We used the electro-optic imaging system to measure the THz peak electric field under the same circumstances above. Shown in Fig. 3.12, we average the THz modulation ratio from a small circle of only 16px ($150\mu m$) diameter on each movie frame. From this modulation ratio, we can use eqn. 3.3 to convert the modulation ratio into an electric field, giving us a peak electric field of 149kV/cm. In Fig.3.13 we show the calibrated electric fields alongside one another. What is clear is that the two-channel EOS system is much lower than the electric fields read by the electro-optic imaging system and the THz intensity profile. A possible reason for this discrepancy is a misalignment between the sampling beam and the THz pulse in the two-channel EOS system. From Fig. 3.11, we can see that the intensity profile of the THz pulse is Gaussian. As a result, the peak electric field measured by the two-channel EOS system will fall off exponentially with misalignment.

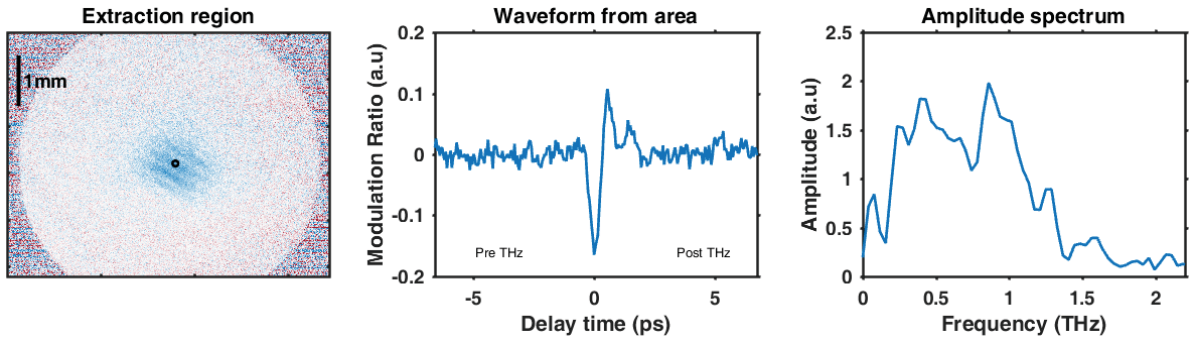

Fig. 3.12 The THz waveform from a movie of THz transmission through an $n_c = 2 \times 10^{17} cm^{-3}$ $In_{0.53}Ga_{0.47}As$:Si thin film, grown on a lattice matched InP:Fe substrate in E-mode using a $3.3mm$ thick GaP imaging crystal, with an active layer $300\mu m$ thick. Using eqn. 3.3 the peak modulation ratio of 0.15 corresponds to an electric field of 149 kV/cm.

3.3 Exploring linearity of imaging system

In regards to Fig. 3.1, the THz pulses are focused directly onto samples, and hence straight onto the electro-optic crystal. Since high field strengths are needed to explore nonlinear dynamics, and the electro-optic crystal is in close proximity to these high fields, it is possible for an increase in applied electric field to produce a decrease in signal (recall Fig. 2.6b). Electric field strengths exceeding roughly $100kV/cm$ may cause modulation ratios to decrease with increasing field strength. Let us refer to this effect as over rotation. Over rotation has been seen to happen in 1mm thick ZnTe, where the peak recorded electric field decreases significantly with increased THz field strength [27], occurring at electric fields as low as $45kV/cm$. In-turn the over rotation described above has the ability to obscure the true detection of a nonlinear process.

To explore this possibility, a 500 μm thick [110] oriented ZnTe crystal was mounted on an n-doped $In_{0.53}Ga_{0.47}As$ thin film with a carrier concentration of $n_c = 2 \times 10^{17} cm^{-3}$. THz pulses are focused onto the sample by an off-axis parabolic mirror, having a focal length of $3in$. The sample was placed on the focal point of this mirror. Movies were made of the THz transmission through this sample at various field strengths, attenuating with the aid of semi-insulating (SI)

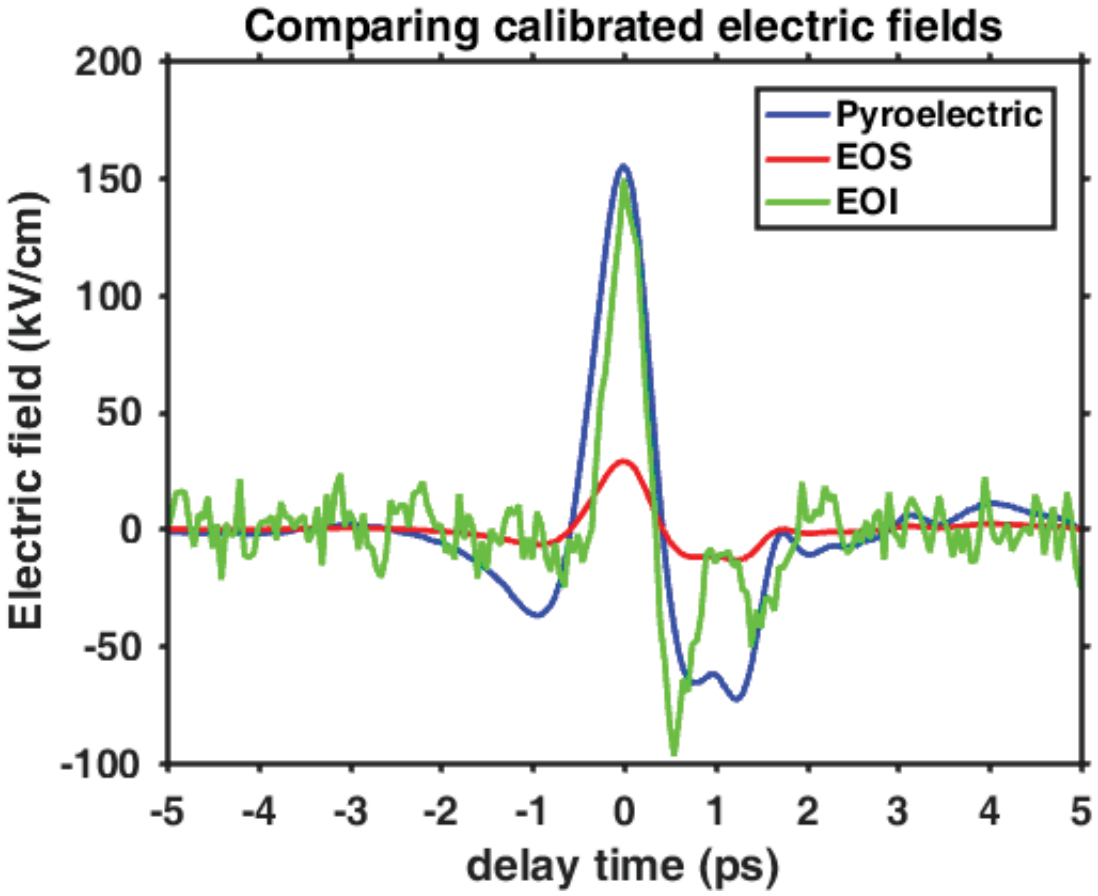

Fig. 3.13 Comparison of electric fields calibrated to using different methods. EOS waveform (red), the EOS waveform scaled to the Peak field from the pyroelectric array (blue), and the calibrated peak field from EOI (green) in E-mode on 300μm thick GaP crystal.

silicon wafers.

The peak modulation ratio in the unattenuated movie is near 0.4 (shown in Fig. 3.14 (a) and (c)), which, using eqn. 2.23, yields an incident electric field of $125 kV/cm$. The central regions of the peak electric fields appear to have a depression. This can be explained in reference to Fig. 2.6. At an electric field near $125 kV/cm$, the modulation is opposite to that in a linear regime, and so the highest electric fields will appear to be lower than expected.

After attenuating the source with 2 SI silicon wafers the maximum modulation ratio became 0.25, which equates to an electric field of $78 kV/cm$. Although this is still quite far from the linear detection regime, we can see a drastic difference in the peak electric-field images in Fig. 3.14 (b) and (d), since the depression within the center of the image has receded. The intensity profiles of the waveforms in Fig. 3.14 are shown in Fig. 3.15 so as to highlight the difference between the waveform measured in an extreme electric field regime, against waveform measured in the more moderate regime. To obtain an intensity profile, every image is squared, and the images are then integrated in time. The intensity profile for the THz pulse seems to have a donut-like profile in the high-field regime that is not present in the low field regime. Although a donut-like intensity has been seen to radiate from two-color plasma sources [28], the ring that we are seeing comes about from a THz pulse having electric field strengths that far surpass a linear regime of detection.

One possible explanation for the behavior seen in the spatial profile of the THz pulse is that the electro-optic crystal is fairly thick. Recalling eqn. 2.23, it can be seen that the thickness of the electro-optic crystal is directly proportional to the modulation ratio. Another explanation is that ZnTe may has a relatively large electro-optic coefficient compared to that of GaP. Therefore, by changing the electro-optic crystal of the imaging system, we should be able to remove the donut-like features.

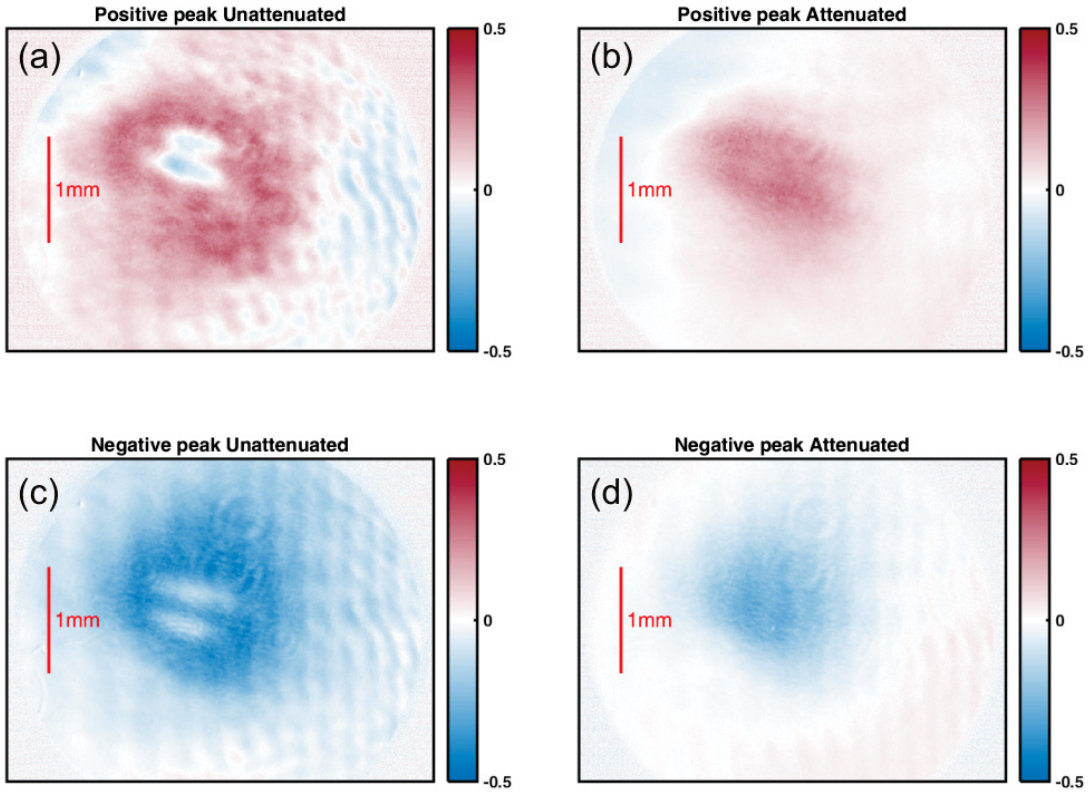

Fig. 3.14 Comparing spatial characteristics of the peak pulse-front shape before and after attenuation with silicon wafers. (a) The peak electric field image, obtained when the imaging crystal sampling outside of the linear regime, on a 0.5mm thick ZnTe imaging crystal affixed to an $n_c = 2 \times 10^{17} cm^{-3}$ low doped $In_{0.53}Ga_{0.47}As$ thin film, grow on a lattice matched InP:Fe substrate. (b) The same peak-electric field, however this time the THz source has been attenuated using two semi-insulating silicon wafers. What we see is the remission of the over-rotated central regions. Panels (c) and (d) demonstrate remission of over rotation for the negative peak electric field as well.

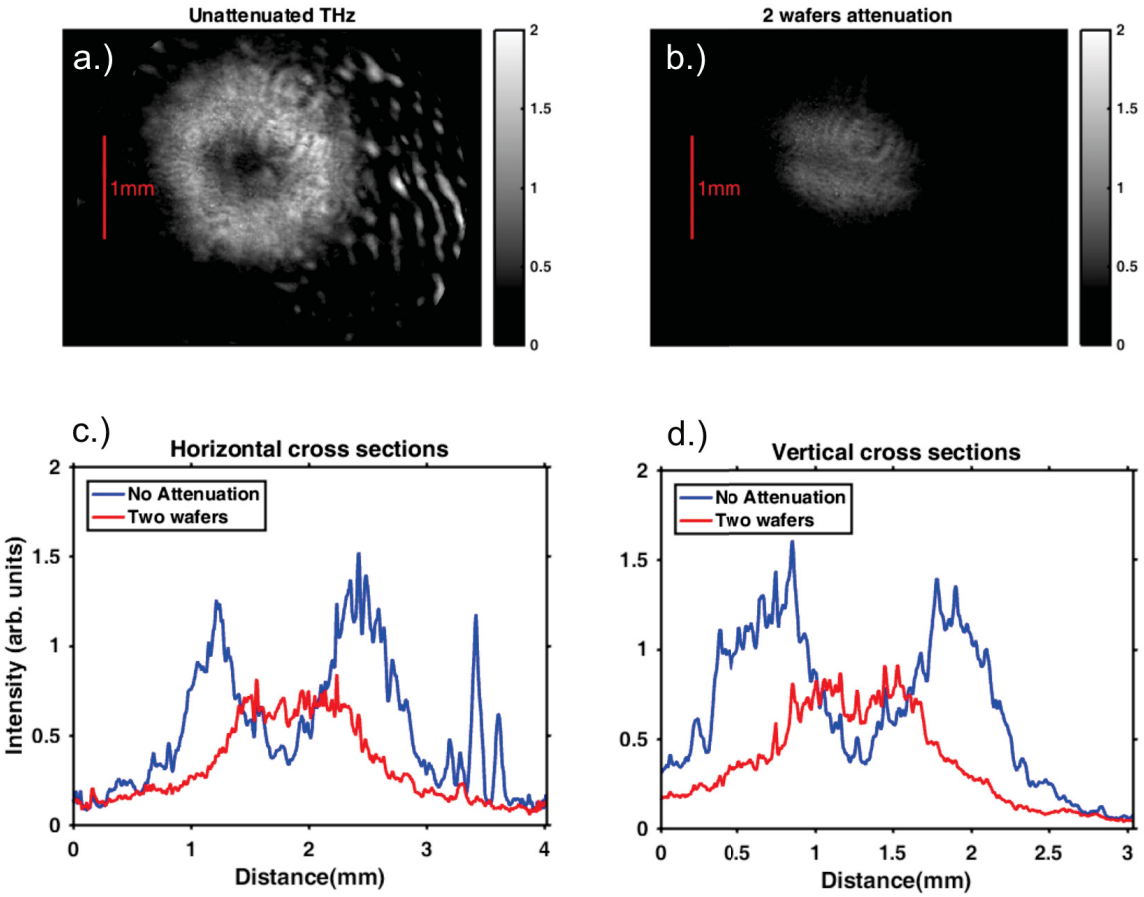

Fig. 3.15 Comparing the intensity profile of THz pulse before and after attenuation with silicon. (a) Near-field THz intensity profile when the THz is left unattenuated. (b) The donut-like feature disappears when the source is attenuated with two semi-insulating silicon wafers. (c) The horizontal profiles of both the attenuated and unattenuated images are shown, while in (d) the vertical profiles are shown.

We chose to use a $300\mu m$ thick [110] GaP crystal mounted to 2mm of [100] Gap, in order to perform electro-optic imaging free from over rotation. The 2mm thick [100] GaP layer elongates the time between reflections within the electro-optic crystal, while maintaining a constant index of refraction. The electro-optic coefficient of GaP ($0.88pm/V$) [18] is smaller than that of ZnTe ($4pm/V$) [16] by roughly a factor of 4, and the thickness is reduced by almost half. Since GaP and ZnTe both have a $\bar{4}3m$ point group [13, 29], the phase induced in eqn. 2.17 by an external electric field maintains the same form [18]

$$\phi_{\text{ext}} = \frac{\pi d n_o^2 r_{41}}{\lambda} E_{\text{ext}}. \tag{3.6}$$

The benefit seen in the equation above this is that for a thinner crystal having a lower electro-optic coefficient, we can expect more than 75% reduction of the modulation ratio. This is non-ideal for scenarios where signals are weak, but given the over-rotation witnessed in ZnTe, changing from ZnTe to GaP should place us well within the linear detection regime.

Fig. 3.16 shows the results of imaging on the same sample as before, with the only difference being the $300\mu m$ GaP imaging crystal. The Fig. 3.16 (a) shows the peak electric field acquired from a time-domain scan. The green lines represent the lines from which the vertical and horizontal cross-sections were taken. Both Fig. 3.16 (b) and Fig. 3.16 (c) show the vertical and horizontal cross sections of the peak electric field image (respectively). Fig. 3.16 (d) shows the time-domain waveform extracted from a $0.3mm$ square surrounding the intersection of the horizontal/vertical cross-sections. By changing the electro-optic imaging crystal from ZnTe to GaP, we have removed the donut-like features from the THz pulse.

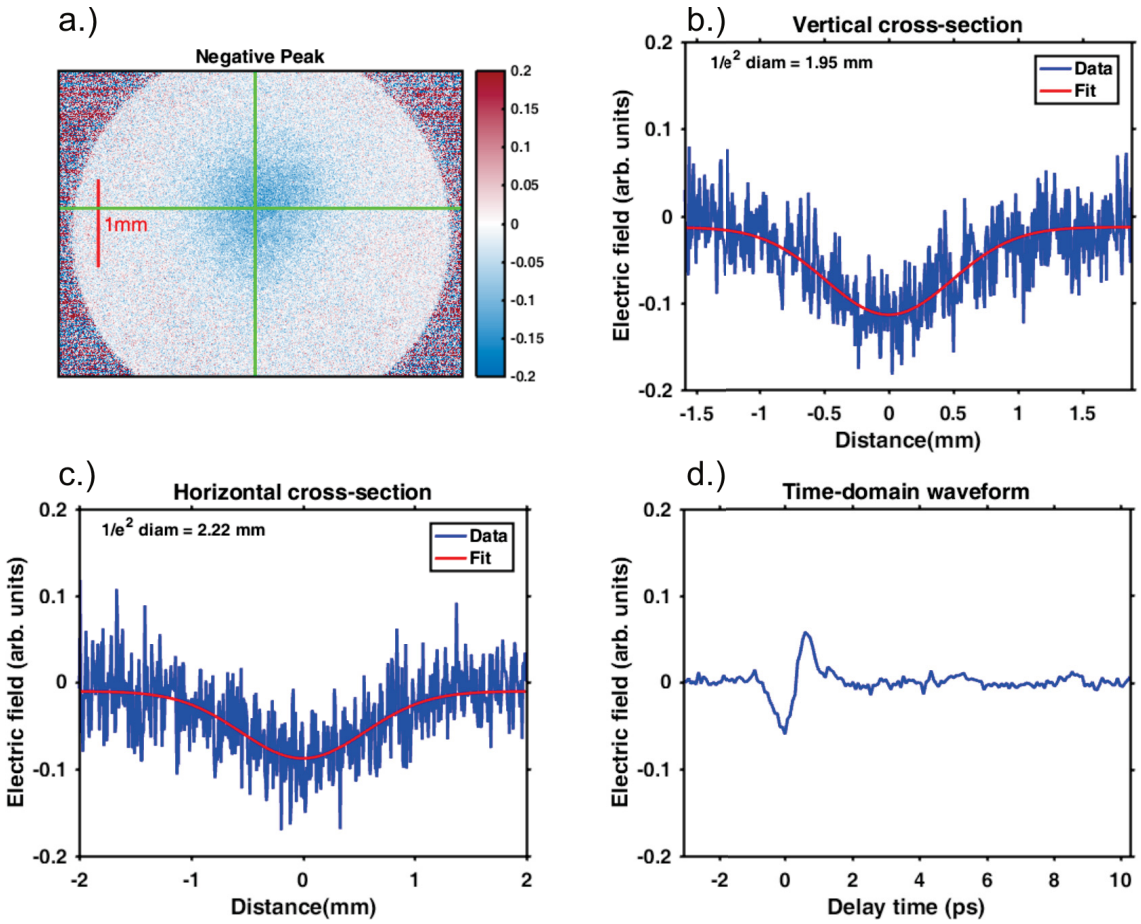

Fig. 3.16 Image of peak negative THz pulse front taken using GaP as an electro-optic crystal. (a) Peak negative THz electric field acquired using a 300 μm thick GaP imaging crystal. Imaging was performed on an $In_{0.53}Ga_{0.47}As$ thin film having $n_c = 2 \times 10^{17} cm^{-3}$, and we see that there is no indication of over-rotation happening with a peak modulation ratio of 0.1 (). (b) A vertical cross section of the peak field, and the corresponding Gaussian fit. The fit indicates a $1/e^2$ diameter of 1.95mm. (c) Horizontal cross-section is shown, demonstrating a $1/e^2$ diameter of 2.22mm. (d) Time-domain waveform extracted by averaging a 0.3mm square surrounding center of the panel (a) for the entire time-series.

Chapter 4

High-field dynamic Drude model of conductivity

4.1 Using light to measure conductivity

Before diving into the details about macroscopic conductivity in thin films, let us first take a minute to talk about circuit theory.

Transmission line theory bridges a very important cross-over region in electrodynamics, connecting field analysis to circuit phenomena [30]. Amazingly, one can derive a series of wave equations for voltage pulses in a transmission line that bear a stunning resemblance to the telegrapher's equations [30, 31]. These equations make it easy to transfer familiar ideas such as index of refraction into circuit theory, provided one can understand some unfamiliar terminology. Let's start off with the *Impedance* (Z), which is just the ratio of a magnetic field and an electric field:

$$Z = \frac{\mathbf{E}}{\mathbf{B}} = \sqrt{\frac{\varepsilon^{(1)}\varepsilon_o}{\mu_o}} = \frac{n}{c} \tag{4.1}$$

In a non-magnetic medium, the impedance is only dependent on the electrical permitivity (ε), the vacuum permittivity (ε_o), and the vacuum magnetic permeability (μ_o) . The *Admittance* (Y)

is simply the inverse of the impedance

$$Y = \frac{1}{Z}. \tag{4.2}$$

The admittance of free space is given by

$$Y_o = \frac{1}{377}\Omega^{-1} \tag{4.3}$$

and so the impedance of free space is

$$Z_o = 377\Omega. \tag{4.4}$$

When a voltage pulse propagates along a transmission line, reflections can occur if there is an impedance mismatch. Letting Z_1 be the impedance before the mismatch, and Z_2 be the impedance after the mismatch, the reflection coefficient is given by

$$r' = \frac{Z_2 - Z_1}{Z_2 + Z_1} = \frac{Y_1 - Y_2}{Y_1 + Y_2} \tag{4.5}$$

which bears a striking resemblance to the electric field reflection coefficient

$$r = \frac{\mathbf{E}_r}{\mathbf{E}_i} = \frac{n_1 - n_2}{n_1 + n_2}. \tag{4.6}$$

where, n_1 is the incident index of refraction and n_2 is the transmitted index of refraction. The voltage transmission coefficient is given by

$$t' = \frac{2Z_2}{Z_1 + Z_2} = \frac{2Y_1}{Y_1 + Y_2} \tag{4.7}$$

which, again, should look familiar, since

$$t = \frac{\mathbf{E}_t}{\mathbf{E}_i} = \frac{2n_1}{n_1 + n_2}. \tag{4.8}$$

The impedance of a thin film is related to the material conductivity and the thickness as

$$Z_{\text{film}} = \frac{1}{\tilde{\sigma} d} \tag{4.9}$$

where d is the thickness of the film, and $\tilde{\sigma} = \sigma_1 + i\sigma_2$ is the bulk complex conductivity. We will now shift the discussion towards addressing the problem of optical transmission at an air-thin film interface, as shown in Fig. 4.1.

In the top image of Fig. 4.1 we show a THz pulse shining onto a conducting film. Let the film have a complex conductivity $\tilde{\sigma}$, thickness d and impedance Z_f. The substrate (brownish region) will be quite large compared to the thin film, and will have an impedance that is related to its index of refraction $Z_s = Z_o/n$, where we assume that the substrate has a real index of n. By the nature of these two surfaces being connected, a circuit can be drawn (Fig. 4.1 (b)), where the film impedance and the substrate impedance are added in parallel to form the load impedance Z_L:

$$\frac{1}{Z_L} = \frac{1}{Z_s} + \frac{1}{Z_f}. \tag{4.10}$$

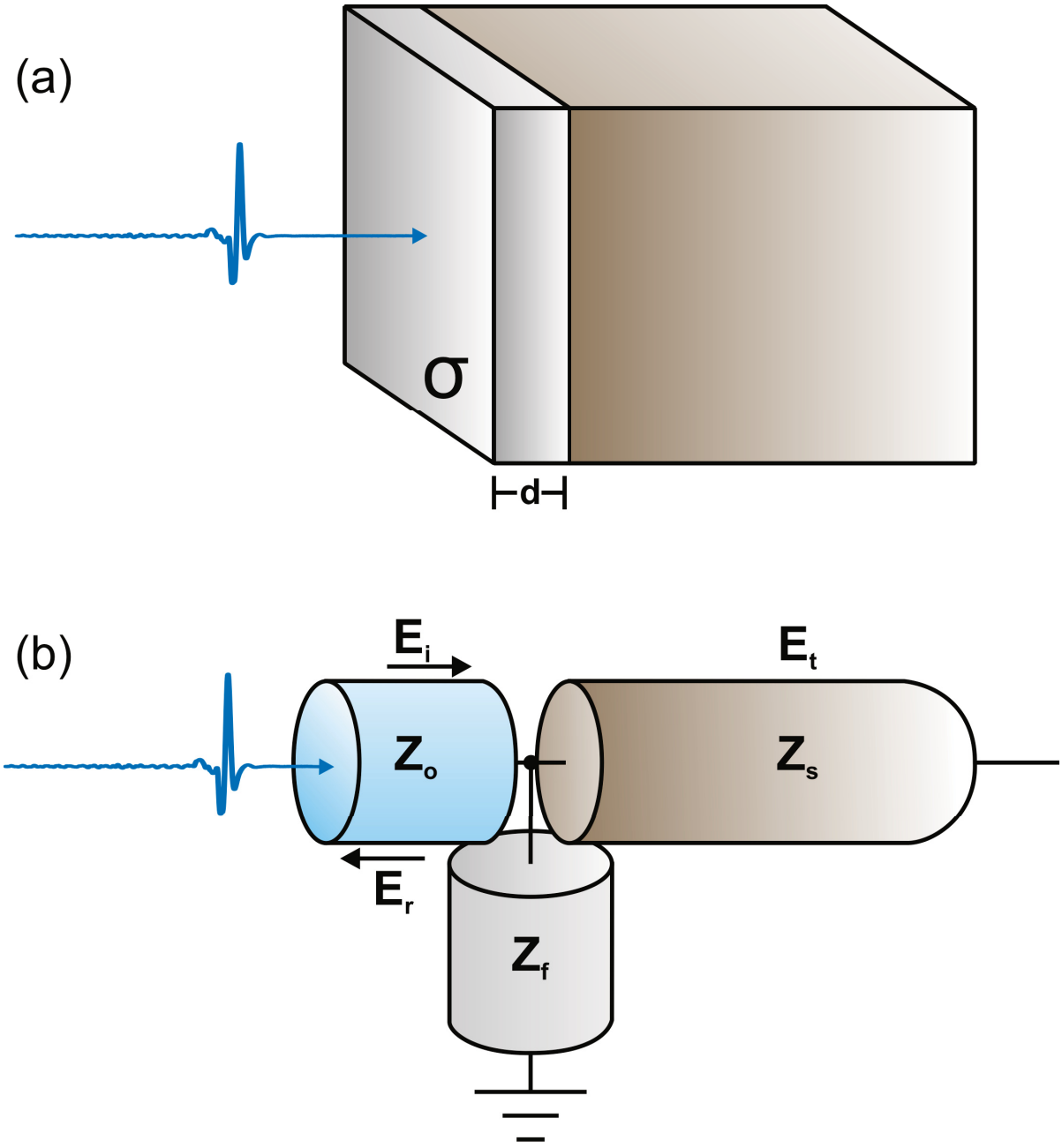

Fig. 4.1 Transmission line diagram of a THz pulse incident to a thin conducting film. Subscripts i, t and r represent the incident, transmitted, and reflected electric fields, while Z_f, Z_o, Z_s represent the impedance of the thin film, free space and the substrate respectively.

In this equivalent circuit, the transmission coefficient is hence given by the thin film equation [32]

$$\begin{aligned} t' &= \frac{2Z_L}{Z_L + Z_o} \\ &= \frac{2}{1 + Z_o/Z_L} \\ &= \frac{2}{1 + Z_o\tilde{\sigma}d + n} \\ &= \frac{2Y_o}{Y_o + nY_o + \tilde{\sigma}d} \end{aligned} \tag{4.11}$$

Therefore, an electric field that passes through a thin film, and a substrate will have the form

$$\mathbf{E}_t = \frac{2Y_o}{Y_o + nY_o + \tilde{\sigma}d}\mathbf{E}_i = \frac{2}{1 + n + Z_o\tilde{\sigma}d}\mathbf{E}_i = t'\mathbf{E}_i \tag{4.12}$$

which is sensitive to the conductive properties of the thin film. Alternatively, by noting that $\mathbf{J} = \tilde{\sigma}\mathbf{E}_t$, we can recast eqn. 4.12 into the form

$$\mathbf{E}_t = \frac{2Y_o\mathbf{E}_i - d\mathbf{J}}{Y_o + nY_o} \tag{4.13}$$

The next two sections will discuss the microscopic origins of conductivity, explaining exactly where σ comes from in the context of the Drude model. The Drude model is a free-carrier model, and can provide a microscopic origin for the material conductivity.

4.2 Low field conductivity: The Drude model

Considering the n-type nature of the samples that are discussed later in Chapter 5, it is worth framing the discussion of the Drude model in the context of n-doped, direct-gap semiconductors (see Fig. 4.2). In these semiconductors, the equilibrium electron population is located in the

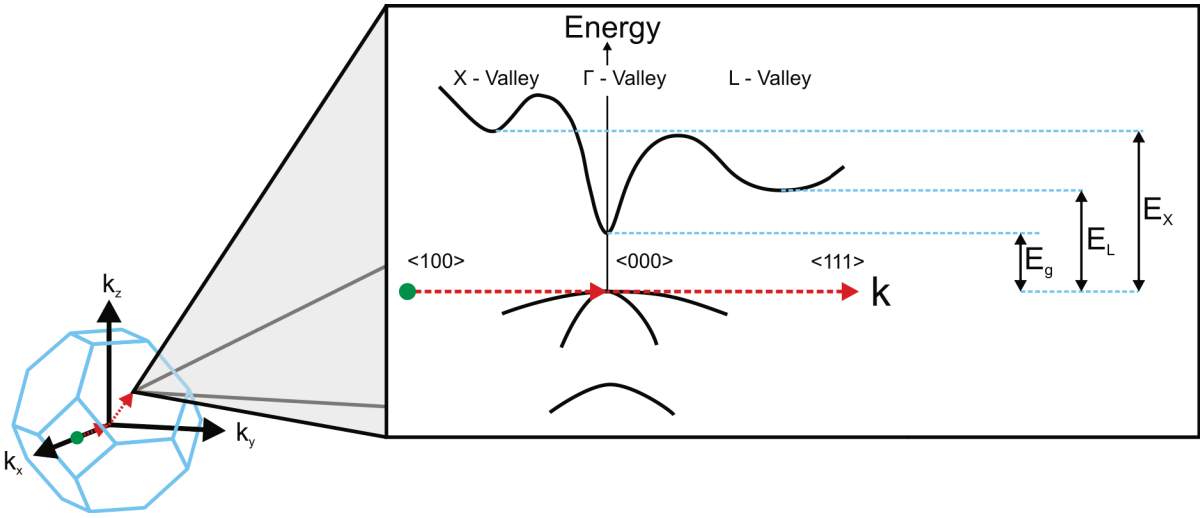

Fig. 4.2 Band diagram of direct-gap semiconductor. As one starts at the green ball and moves along 3D axes of a Brillouin zone in $\vec{k}$-space (red-arrows), one can reproduce a band diagram by noting the stack of energy states at each location in $\vec{k}$-space. Electrons in equilibrium rest in the global band minimum, which has a nearly quadratic shape. E_g, E_L, E_X represent the Γ-valley, L-valley and X-valley band gap energies respectively.

global band minimum (around $\mathbf{k} = 0$). This results in the carrier population experiencing a nearly parabolic dispersion, similar to that of free electrons. In turn these conduction electrons behave qualitatively like free electrons, with the slight modification of an effective mass defined by

$$m^* = \hbar^2 \left(\frac{\partial^2 E(\mathbf{k})}{\partial \mathbf{k}^2} \right)^{-1}, \tag{4.14}$$

which is inversely proportional to the band curvature, and proportional to the square of the reduced planck constant ($\hbar$). In the effective mass approximation, conduction band electrons embedded in an electric field ($\mathbf{E}$) are accelerated according to

$$\mathbf{F} = m^* \frac{\mathrm{d}\mathbf{v}}{\mathrm{d}t} = \hbar \frac{\mathrm{d}\mathbf{k}}{\mathrm{d}t} = q\mathbf{E} = -e\mathbf{E}, \tag{4.15}$$

where e denotes the magnitude of the fundamental electric charge. With real semicondcutors this equation of motion is not complete since a crystal lattice is abound with phonons, impurities, lattice defects, and even surface boundaries from which electrons may scatter. To encapsulate

these scattering processes, we introduce a velocity dependent force to eqn. 4.15, resulting in the new equation of motion

$$m^* \frac{\mathrm{d}\mathbf{v}}{\mathrm{d}t} = -e\mathbf{E} - \frac{1}{\tau} m^* \mathbf{v}. \tag{4.16}$$

Affixed to the velocity dependent (friction-like [33]) term is the collisional dampening rate $(1/\tau)$, which is defined by the mean scattering time τ.

4.2.1 DC Conductivity

If a constant electric field ($\mathbf{E}_o$) is applied to the system for a long enough time for an equilibrium to be reached, the electron velocity becomes time-independent, and so $d\mathbf{v}/dt = 0$, reducing eqn. 4.16 to the much simpler form as follows.

$$\mathbf{v}(t) = -\frac{e\tau}{m^*} \mathbf{E}_o \tag{4.17}$$

eqn. 4.17 allows us to extract the DC conductivity by noting that the current density has the form $\mathbf{J} = -ne\mathbf{v} = \sigma\mathbf{E}$

$$\sigma_{\mathrm{DC}} = \frac{\mathbf{J}}{\mathbf{E}} = \frac{ne^2\tau}{m^*} = \omega_p^2 \varepsilon_o \tau \tag{4.18}$$

where we have defined the plasma frequency as $\omega_p = \sqrt{ne^2/\varepsilon_o m^*}$, and the density of carriers is denoted by n. The ratio of the average drift velocity of carriers to the DC electric field strength can tell us about the mobility of electrons in a material, and is defined as follows

$$\mu \equiv \frac{\mathbf{v}}{\mathbf{E}} = \frac{e\tau}{m^*} = \frac{\sigma_{\mathrm{DC}}}{ne}. \tag{4.19}$$

4.2.2 AC-conductivity

In the presence of an AC driving field of frequency ω, ie,

$$\mathbf{E}(t) = E_o\left(\cos(\omega t) + i\sin(\omega t)\right) \tag{4.20}$$

eqn. 4.16 can be solved analytically by noting a homogeneous solution of the form

$$\mathbf{v}_{hom}(t) = v_o e^{-t/\tau} \tag{4.21}$$

and a particular solution of the form

$$\mathbf{v}_{part}(t) = Ae^{i\omega t}. \tag{4.22}$$

After solving for A, we can write the total current density as

$$ne\mathbf{v}(t) = \underbrace{nev_o e^{-t/\tau}}_{\text{Impulse}} - \left[\underbrace{\frac{ne^2\tau}{m^*}\frac{1}{1+\omega^2\tau^2}}_{\text{Re}\{\widetilde{\sigma}\}}E_o + i\underbrace{\frac{\omega\tau^2 ne^2}{m^*}\frac{1}{1+\omega^2\tau^2}}_{\text{Im}\{\widetilde{\sigma}\}}E_o\right]e^{i\omega t} \tag{4.23}$$

Usually at initial times the electron velocity is zero, and so the “impulse" term of eqn. 4.23 vanishes. Looking to the oscillating components of eqn. 4.23, we see the sum of the real and imaginary contributions of the driving field. Furthermore, since

$$\mathbf{J} = \widetilde{\sigma}\mathbf{E} = -ne\mathbf{v} \tag{4.24}$$

we can read out the real and complex parts of the conductivity (σ_1 and σ_2 respectively) as

$$\begin{aligned}\sigma_1 &= \frac{\sigma_{\mathrm{DC}}}{1+\omega^2\tau^2} \\ \sigma_2 &= \frac{\omega\tau\sigma_{\mathrm{DC}}}{1+\omega^2\tau^2}\end{aligned} \tag{4.25}$$

In summary, we have shown that a free electron experiencing an alternating electric field has a characteristic current density related to the Drude conductivity. Connecting this idea to the previous section, the conductivity shown in eqn. 4.12 appears in the transmission coefficient of material as follows:

$$\mathbf{E}_t = \frac{2Y_o}{Y_o + nY_o + \tilde{\sigma}_{\mathrm{Drude}}d}\mathbf{E}_i \tag{4.26}$$

where Y_o is the admittance of free space, $\tilde{\sigma}_{\mathrm{Drude}}$ is the Drude conductivity, d is the epilayer thickness, $\mathbf{E}_t$ and $\mathbf{E}_i$ are the incident and transmitted electric fields respectively. Experimentally we can measure incident and transmitted waveforms quite easily. So, having a thin-film sample mounted on a substrate, and a plain substrate sample, we can perform time-domain spectroscopy by calculating the ratio of the thin-film electric field transmission to the substrate transmission.

$$\begin{aligned}\frac{\mathbf{E}_{t,\mathrm{sub}}}{\mathbf{E}_{t,\mathrm{film}}} &= \frac{\mathbf{E}_i \times (t_{\mathrm{sub}}) \times (t_{\mathrm{sub}}) \times e^{ikL}}{\mathbf{E}_i \times (t_{\mathrm{sub}}) \times (t_{\mathrm{film}}) \times e^{ikL}} \\ &= \frac{Z_o d\tilde{\sigma}_{\mathrm{Drude}} + n + 1}{n+1} \\ &= \left[1 + \frac{Z_o d\sigma_1}{n+1}\right] + i\left[\frac{Z_o d\sigma_2}{n+1}\right]\end{aligned} \tag{4.27}$$

Measuring the waveforms above in discrete intervals, we can perform a fast Fourier transform of the time-domain THz waveforms to obtain an array of complex numbers for the substrate data and the thin film data. Dividing the complex numbers element-by-element in the array (according to eqn. 4.27), we obtain a complex array of numbers of the form $x(\omega) + iy(\omega)$. This

array is related to the real and imaginary parts of eqn. 4.27 through

$$x(\omega)+iy(\omega)=\left[1+\frac{Z_o d n_e e^2\tau}{m^*(1+n)(1+\omega^2\tau^2)}\right]+i\left[\frac{Z_o d\omega\tau^2 n_e e^2}{m^*(n+1)(1+\omega^2\tau^2)}\right], \tag{4.28}$$

where we have denoted the electron density n_e so as to avoid confusion with the substrate index of refraction n. This is just one example of how THz time-domain spectroscopy can be used to compare theoretical conductivity to experimental results, as the choice of a model for conductivity is going to be relevant to the system at hand. In n-doped semiconductors, electrons are mostly free, and so a Drude model would be a natural choice. Figure 4.3 highlights the results of performing THz time-domain spectroscopy on heavily doped $In_{0.53}Ga_{0.47}As$ thin films. The curve fitting algorithm is given in Appendix A.2.3. The fit indicates a DC conductivity of $\sigma_{DC}=(1.03\pm0.07)\times10^5\Omega^{-1}m^{-1}$, and a mean scattering time of $\tau=(170\pm5)fs$, matching very closely to those reported by Ayesheshim K. Ayesheshim ($\sigma_{DC}=1.04\times10^5\Omega^{-1}m^{-1}$ and $\tau=131fs$) [10]. The mean absolute error associated with the above fit is calculated by

$$MAE=\frac{\sum_{i=1}^{N}|y_{meas,i}-y_{fit,i}|}{N}, \tag{4.29}$$

where N is the number of experimental data points, $y_{meas,i}$ is the ith measured data point, $y_{fit,i}$ is the fitted data point corresponding to $y_{meas,i}$, and N is the number of data points. The reported mean average error for this fit is $7.7\times10^3\Omega^{-1}m^{-1}$. The reduced χ^2 is defined as

$$\tilde{\chi}^2=\frac{1}{N}\sum_{i=1}^{N}\left(\frac{(y_i-y(x_i))}{\alpha_i}\right)^2, \tag{4.30}$$

where y_i and $y(x_i)$ are the observed and fit y-values respectively, N is the number of degrees of freedom, and α_i are the errors for the y-coordinate $y(x_i)$. For the fit shown in Fig. 4.3, a $\tilde{\chi}^2$ value of 1.85 is reported, indicating a good fit.

A brief note on curve fitting, since both the real and imaginary conductivities are coupled

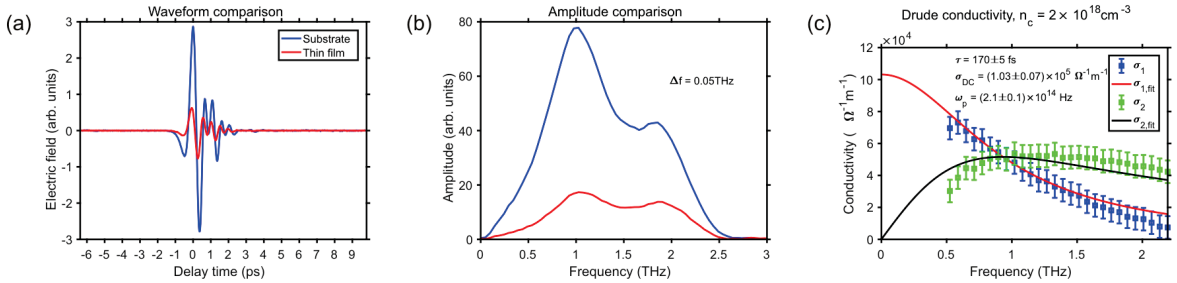

Fig. 4.3 THz time-domain spectroscopy of an n-doped $In_{0.53}Ga_{0.47}As$ thin-film. (a) The time-resolved THz waveforms. The blue waveform corresponds transmission through a reference substrate, while the red waveform is the measurement from transmission through a substrate with an n-doped InGaAs epilayer. (b) Amplitudes of fourier transformed waveforms from (a). (c) Fit using eqn. 4.28. Blue squares (red line) correspond to the real conductivity from measurement (theory). Green squares (black line) correspond to the imaginary conductivity from measurement (theory)

through the variable τ, σ_1 and σ_2 must be fit simultaneously, in order to guarantee a shared value of τ in the fitting process. The fast Fourier transform is used to transform the THz waveforms shown in Fig. 4.3 (b). Due to reflections from within the electro-optic crystal and the sample of interest, the time-domain waveforms are shortened, which has direct implications on the frequency resolution of our data through

$$t_{max} - t_{min} = \frac{1}{2\Delta f}, \tag{4.31}$$

where $t_{max} - t_{min}$ is the time window over which we sample the THz electric field, and Δf is the subsequent frequency resolution. Because the fast fourier transform uses a base-2 bit reversal algorithm [34], the fast fourier transform algorithm automatically pads the input data with zeros so that the waveforms have a length that is divisible by 2.

4.3 High field conductivity: Dynamic Drude model

Continuing our discussion of conduction band electrons, we need to address a looming issue. We've been ignoring the presence of nearby satellite valleys (Fig. 4.2), which does a disservice to their importance in the presence of strong electric fields.

In InGaAs there are two satellite valleys in the conduction band (X and L valleys) that surround the global minimum (Γ-valley), and they have curvatures that differ from the curvature of the Γ-valley. This has direct implications on the effective mass of electrons that populate these valleys. Intervalley scattering is a process whereby a strong electric field accelerates free electrons into high into the conduction band, where phonon scattering relocates a portion of the electron population into these satellite valleys. Because of the effective mass difference, the mobility of electrons decreases [11, 12]. Consequently, eqn. 4.12 shows that the reduced conductivity is going to result in an increased transmittance.

In this section we aim to physically describe Fig. 4.4. Let us consider a two-band model, using only the Γ and L-valleys, where the effective masses of electrons in these valleys are written as m^*_Γ and m^*_L respectively. The total number of free electrons doesn't change in this simulation, and so the number of electrons in the Γ-valley (n_Γ) is related to the number of electrons in the L-valley (n_L) by

$$n_\Gamma(t) = n_o - n_L(t) \tag{4.32}$$

where n_o is the total number of free electrons. When a THz pulse is incident on a sample, the current density excited by this electric field is given by

$$\mathbf{J}(t) = -n_\Gamma(t) e \mathbf{v}_\Gamma(t) - n_L(t) e \mathbf{v}_L(t) \tag{4.33}$$

where e is the elementary charge, $\mathbf{v}_\Gamma$ and $\mathbf{v}_L$ are the electron velocities of the respective valleys at time t. The electric field transmitted through a sample with electrons in both valleys is given by eqn. 4.13 [10]

$$\mathbf{E}_t = \frac{2Y_o\mathbf{E}_i(t) - d\mathbf{J}}{Y_n + nY_o} \tag{4.34}$$

where $\mathbf{E}_i$ is the incident electric field, d is the thickness of the substrate, n is the substrate index of refraction and Y_o is the familiar admittance of free space. $\mathbf{E}_t$ accelerates electrons in each of the satellite valleys according to the two equations of motion

$$\begin{aligned} \frac{\mathrm{d}\mathbf{p}_\Gamma}{\mathrm{d}t} &= -e\mathbf{E}_t(t) - \frac{\mathbf{p}_\Gamma}{\tau_\Gamma} \\ \frac{\mathrm{d}\mathbf{p}_L}{\mathrm{d}t} &= -e\mathbf{E}_t(t) - \frac{\mathbf{p}_L}{\tau_L} \end{aligned} \tag{4.35}$$

Electrons in these valleys are accelerated into energy states associated with the momentum gained from the above equations of motion. The Γ and L-valley electron energies are given by the kinetic energy of the accelerated electrons, and the average thermal electron energies

$$\begin{aligned} E_\Gamma &= \frac{\mathbf{p}_\Gamma^2}{2m_\Gamma^*} + \frac{3}{2}k_BT \\ E_L &= \frac{\mathbf{p}_L^2}{2m_L^*} + \frac{3}{2}k_BT \end{aligned} \tag{4.36}$$

The rate that electrons scatter from the Γ-valley to the L-valley ($\tau_{\Gamma\to L}^{-1}$) is given by a piecewise continuous function, and the reverse scattering rate is assumed to be constant ($\tau_{L\to\Gamma}^{-1}$), since the density of energy states in the central minimum is much lower than the density of states in the

satellite valley [35]. $\tau^{-1}_{\Gamma\to L}$ is given by

$$\tau^{-1}_{\Gamma\to L}(E_\Gamma,t) = \begin{cases} 0 & E_\Gamma < E_{th}-\Delta \\ \tau^{-1}_{\Gamma\to L,0} & E_\Gamma \geq E_{th}+\Delta \\ \text{smooth function} & E_{th}-\Delta < E_\Gamma < E_{th}+\Delta \end{cases} \tag{4.37}$$

where E_{th} is a threshold energy that governs electron scattering, $\tau^{-1}_{\Gamma\to L,0}$ is the maximum $\Gamma\to L$ scattering rate and *smooth function* is a seventh order polynomial that is continuous up to its third derivative [10, 11, 36, 37]. This polynomial serves as a continuous connection between an intervalley scattering rate of zero, and $\tau^{-1}_{\Gamma\to L,0}$. Δ is a width parameter that sets the region over which the smooth function is active. Now that the intervalley scattering rates are known, it is possible to update the number of electrons in each of these valleys. The rate of change of electrons in the Γ-valley is the number of electrons that arrive, minus the number of electrons that have left

$$\frac{\mathrm{d}n_\Gamma}{\mathrm{d}t} = \frac{n_L}{\tau_{L\to\Gamma}} - \frac{n_\Gamma}{\tau_{\Gamma\to L}} \tag{4.38}$$

This can be rewritten using eqn. 4.32

$$\frac{\mathrm{d}n_\Gamma}{\mathrm{d}t} = \frac{n_o - n_\Gamma}{\tau_{L\to\Gamma}} - \frac{n_\Gamma}{\tau_{\Gamma\to L}}, \tag{4.39}$$

which shows that a new Γ-valley electron population can be calculated for the next time-step, i.e,

$$n_\Gamma(t+\Delta t) = n_\Gamma(t) + \frac{\mathrm{d}n_\Gamma}{\mathrm{d}t}\Delta t. \tag{4.40}$$

Let us now take some time to frame these equations in the context of Fig. 4.4. An incident THz electric field is attenuated by the presence of electrons in the thin film, according to the instantaneous material conductivity given by equations 4.33 and 4.34. This attenuated electric field accelerates electrons within the Γ and L-valleys according to their equations of motion, eqn. 4.35. From this acceleration, a Γ-valley energy can be calculated using eqn. 4.36, which is

in turn used to calculate the $\Gamma \rightarrow L$ electron scattering rate (eqn. 4.37). Assuming the $L \rightarrow \Gamma$ scattering rate is constant, we can update the electron population for each valley using eqn. 4.40. Thus a new electric field is incident, and the cycle will continue over and over until the THz pulse has transmitted through the sample. This cycle is shown in Fig. 4.5, where an incident electric field is converted into a transmitted field, by running it through the algorithm outlined above.

Experimentally, we can measure the time-domain waveforms for incident and transmitted THz pulses to very good accuracy. The presence of intervalley scattering in the sample can thus be detected by looking at how intervalley scattering reshapes the THz electric field on sub-cycle timescales. A key signature of the subpicosecond reshaping is the rectification of the THz pulse in the near-field. In this sense, a THz pulse that was originally a symmetric function will acquire asymmetry as the transmissivity of the sample changes on subpicosecond time scales, giving the THz pulse a net directionality. The net directionality of a transmitted pulse is the primary motivation for studying intervalley scattering in the near-field, since the rectified components of the transmitted electric field will diffract rapidly away from the surface of transmission. Figure 4.6 shows an example of the rectification of an input electric field, by running it through the intervalley simulation located in Appendix A.2.1. Figure 4.6 (a) is a selection of waveforms calculated using eqn. 2.8, and scaled to peak electric fields between $15 kV/cm$ and $75 kV/cm$. As the peak electric field is increased, the integrated waveforms in Fig. 4.6 (c) always converge on zero. The simulation requires an input maximum electric field, and a normalized waveform. Running the waveforms from Fig. 4.6 (a) through the intervalley scattering simulation, the waveforms in Fig. 4.6 are generated. They are attenuated by reflections from the sample surface, and when fields are strong ($75 kV/cm$ waveform) the sample can be seen to undergo a subpicosecond boost in transmission at the onset of the peak electric field. This subpicosecond reshaping of THz pulses is what gives rise to a net integral in Fig. 4.6 (d). The material parameters used in this simulation can be found in Appendix A.2.1.

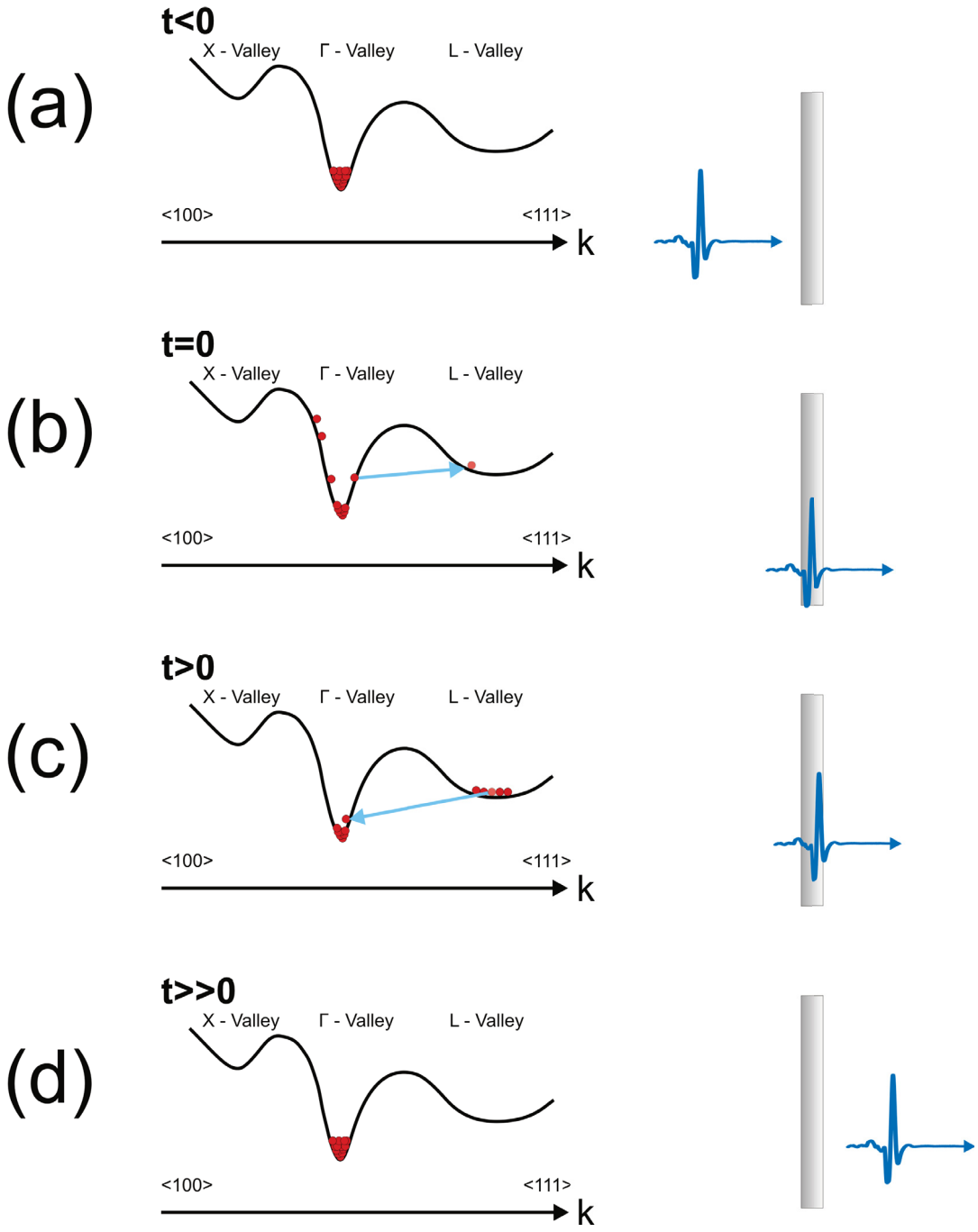

Fig. 4.4 Diagram of the intervalley scattering process. (a)Conduction band electrons in equilibrium. (b) Conduction band electrons are accelerated into high energy states, where phonon scattering scatters electrons to a nearby satellite valley. (c) The thin-film conductivity has lowered before the THz pulse has left the film, resulting in a boost in transmittance. (d) The THz pulse leaves the sample, encoded with the sub-cycle asymmetry in transmittance.

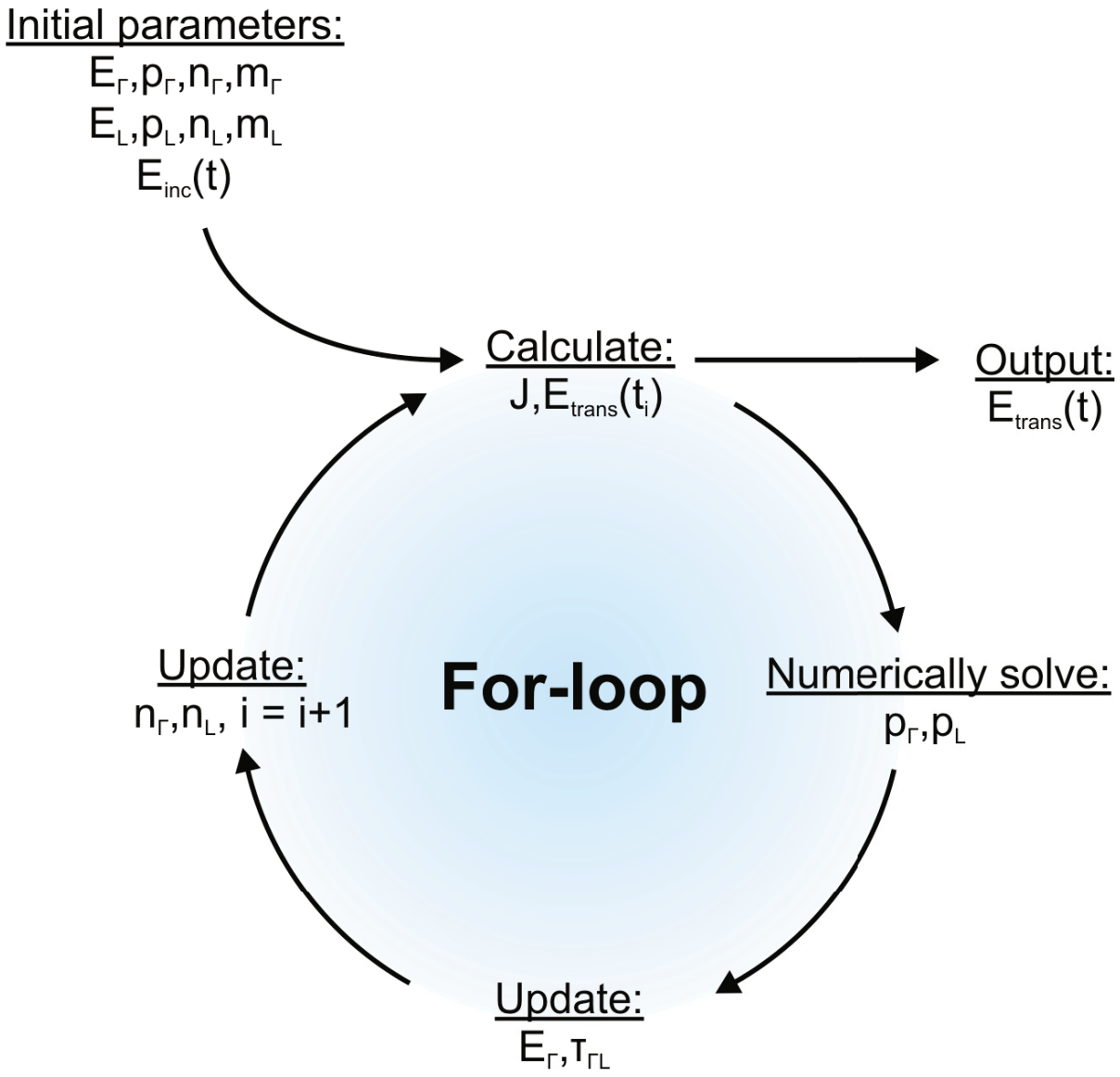

Fig. 4.5 Dynamic Drude model used to simulate nonlinear transmission induced by intervalley scattering. The simulation takes in an array of electric field values and time steps $E_{\text{inc}}(t)$. It numerically solves the momentum of an electron population, and uses this to update the population of electrons in the Γ and L-valleys. Using the updated populations, the transmission coefficient for each step is calculated. The simulation computes an array of electric field values for a THz pulse that exits a sample undergoing intervalley scattering ($E_{\text{trans}}(t)$). The loop ends once a transmitted electric field has been calculated for each element of the input array E_{in}.

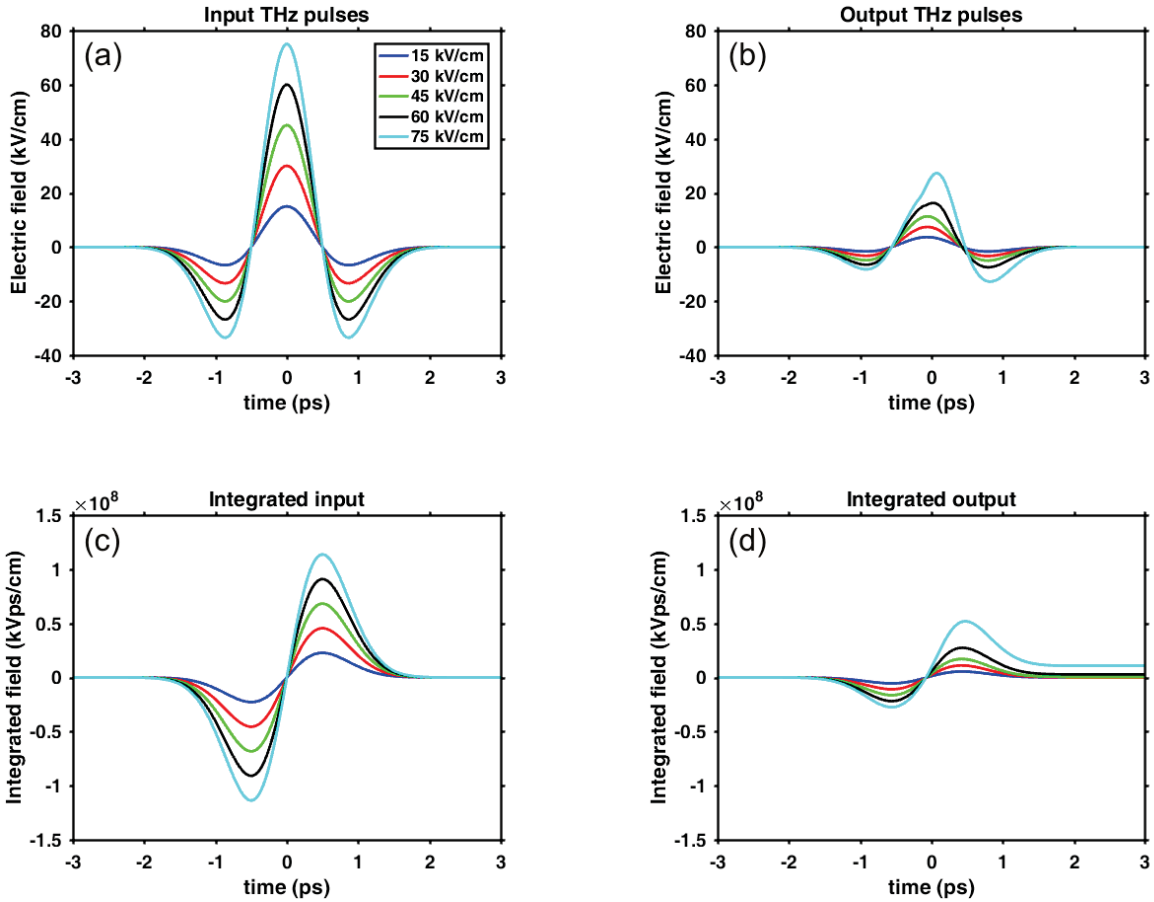

Fig. 4.6 Comparing the THz waveforms input to the intervalley scattering simulation and output from the simulation. (a) Ideal THz waveforms input to the simulation from eqn. 2.8, scaled to a variety of peak fields. (b) The THz pulses that have undergone simulated transmission trough a system undergoing intervalley scattering. Notice that in the high field waveforms, there is the presence of enhanced transmission (dent appears around t = 0ps), and that the waveforms are no longer symmetric. (c) Integrals of input THz pulses. The integrals converge on zero for late times, indicating that the total electric field is zero. This integral serves as an indicator for intervalley scattering, as seen in (d). (d) Integrals of the waveforms shown in (b). Notice that the integrals do not converge to zero. This is the result of the subpicosecond changes in conductivity that reshape the transmitted electric field. Also notice that in the low electric field limit, the waveforms integrate to zero, indicating that intervalley scattering has not occurred.

Chapter 5

Ultrafast imaging of intervalley electron dynamics in n-doped InGaAs epilayers

5.1 Open Aperture Z-scan experiment

5.1.1 Samples

Absorption bleaching is the result of a physical process inducing an ehnanced transmissivity of a material. The transmittance is seen to increase nonlinearly with incident field strength.

This section will discuss the open-aperture z-scans performed on three semiconductor wafers. The first wafer is a $d = 350\mu m$ thick, semi-insulating InP:Fe wafer oriented to the [100] direction. There are two more InP wafers, but these have $In_{0.53}Ga_{0.47}As$ epilayers grown on one side. The ratio of Ga/In is specifically chosen to encourage lattice matching between the $In_{0.53}Ga_{0.47}As$ epilayers and their InP substrates. The $In_{0.53}Ga_{0.47}As$ epilayers have a thickness of $500nm$, and are doped with Si to produce an excess of free charge carriers. There are two doping densities, $n_c = 2 \times 10^{17} cm^{-3}$, which we refer to as the low doped sample (LD), and $n_c = 2 \times 10^{18} cm^{-3}$ which we refer to as the highly doped sample (HD). As a control sample, semi-insulating GaAs was also used to verify the insulating nature of the substrate. Samples

have two possible orientations. The first orientation is shown in Fig. 5.1 (a), where the THz pulse is first incident to the $In_{0.53}Ga_{0.47}As$ thin film. The second orientation is shown in Fig. 5.1, where the THz pusle is first incident to the substrate side of the sample. This sample asymmetry will be important in Section 5.1.3.

5.1.2 Details

To characterize a saturable absorption process, such as intervalley scattering, one has the option to use an open aperture z-scan approach, whereby the transmitted energy is monitored as a sample is moved through the focus of an intense light pulse. Previously, z-scans of various forms been used to measure cubic nonlinearities in semiconductors [38, 39], demonstrate the strong presence of homogeneous broadening in side-chain azobenzene polymers [40], excited state nonlinearity in polythiophene thin films [41] and intervalley scattering [12] in n-doped InGaAs epilayers. Some key features to look for are a doping-dependent broadening of the nonlinear transmission, as well as a diode-like behavior as the sample is inverted in the sample holder. The primary feature of interest is the large boost in transmission seen at the focus ($z = 0$) of a THz pulse. This is expected because as the sample approaches the focus of a THz pulse (well approximated by a Gaussian optics), the peak electric field increases according to [42]

$$E_{\mathrm{THz}}^{\mathrm{peak}} = \frac{E_o}{\sqrt{1+\frac{z^2}{z_R^2}}}. \tag{5.1}$$

where E_o is the THz peak field and $z_R = \pi w_o^2/\lambda$ is the Rayleigh range, characterized by the THz wavelength (λ) and beam waist (w_o) [10, 42]. As the sample approaches the focus, an increasing amount electrons are accelerated high into the conduction band (eqn. 4.35), and so more electrons scatter into nearby sattelite valleys of the conduction band. The displaced population lowers the net conductivity, and in turn the transmissivity of the sample increases until a saturation of absorption occurs near the focus.

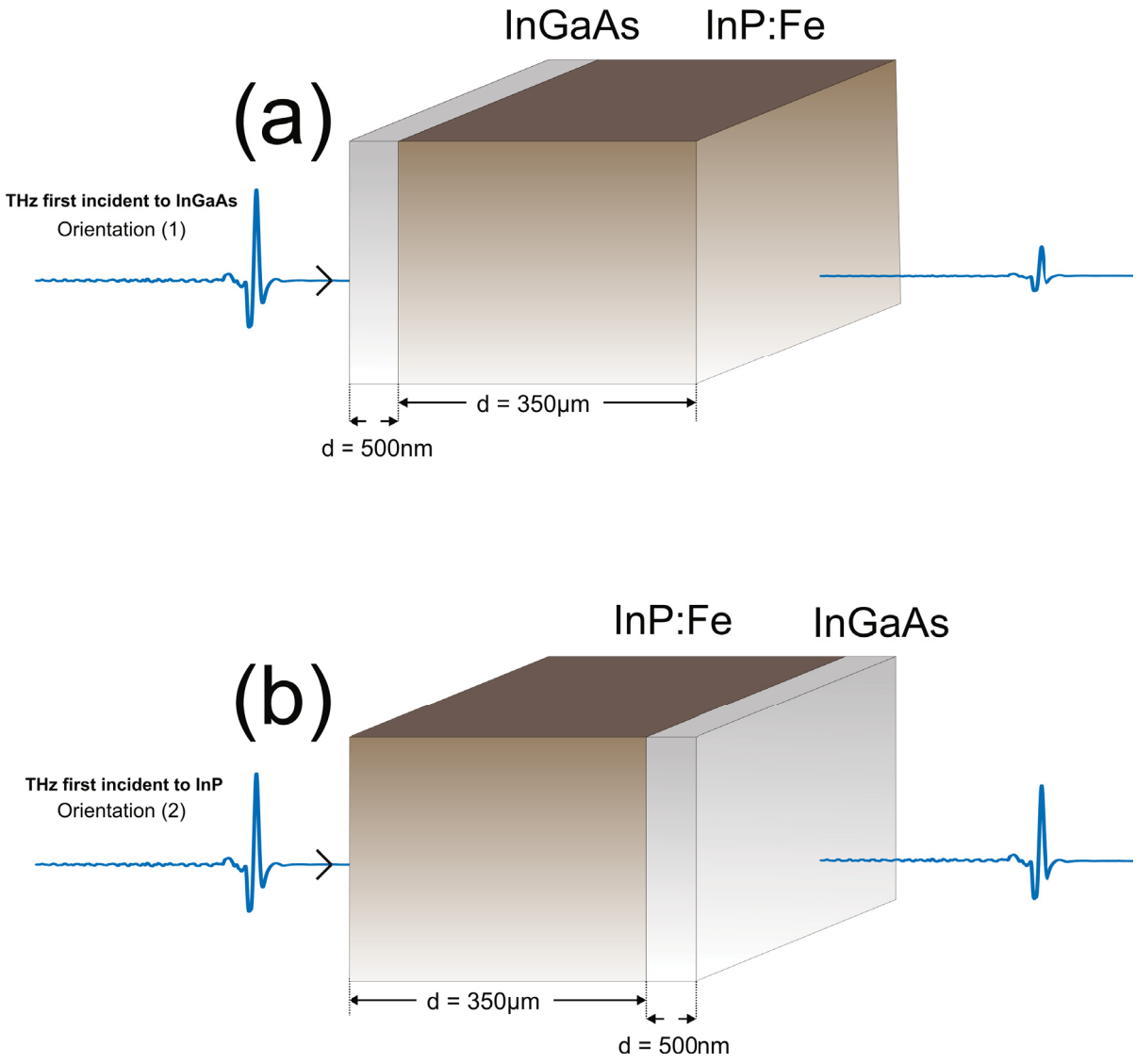

Fig. 5.1 Two orientations of samples used in open aperture z-scans. (a) THz pulse first incident to n-doped $In_{0.53}Ga_{0.47}As$ epilayer. (b) THz pulse first incident to InP substrate.

In order to perform these measurements, a pyroelectric detector (SPJ-D-8: Spectrum Detector Inc.) is used to measure the energy of THz pulses. The pyroelectric detector is attached to a lock-in amplifier, and is read out by a National Instruments DAQ board, and recorded by a LabView program. The LabView program also controls a motorized stage (Thorlabs MTS50A-Z8) that can move the sample through the focus.

Figure 5.2 is a schematic of an open-aperture z-scan experiment. As the sample is moved across the focus, the transmissivity of the sample increases. After the sample passes through the focus, the transmissivity decreases.

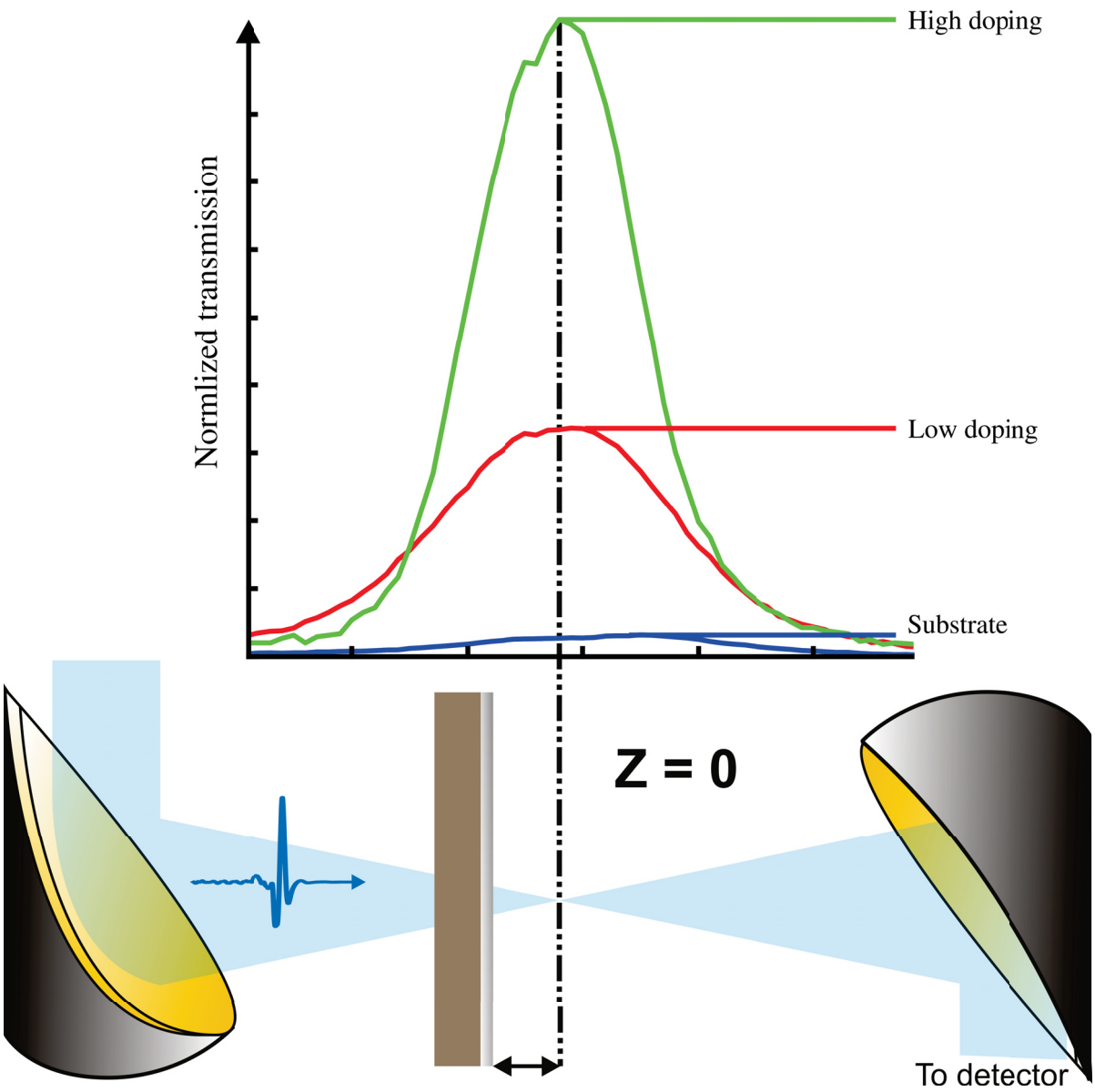

Fig. 5.2 Schematic of an open-aperture z-scan experiment, where a sample moves through the focus of a THz pulse. By measuring the transmitted energy at each step, we can get a measure of the location where the peak absorption bleaching occurs. For the highly doped sample, we see a very short onset of the absorption bleaching, whereas in the low doping sample shows shallower onset of absorption bleaching.

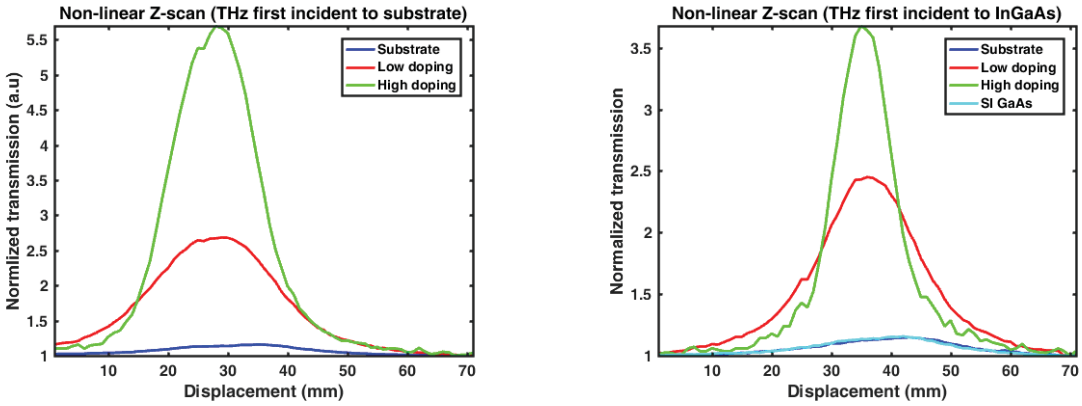

(a) (b)

Fig. 5.3 Experimental results of an open aperture z-scan experiment, as measured by a pyroelectric detector. (a) Transmitted energy measured along THz propagation axis, normalized to the far-field values. The THz pulse is first incident to the substrate. The blue curve is an open aperture z-scan of the InP substrate. (b) The same measurement as in (a), however THz pulses are now first incident to the n-doped epilayer. The cyan curve is an open aperture z-scan of a semi-insulating (SI) GaAs wafer. The SI GaAs exhibits transmissive behavior similar to the InP substrate.

5.1.3 Diode-like behavior

By measuring the transmitted energy, and dividing by the far-field energy value, we can retrieve the normalized transmission. The normalized transmission data for open-aperture z-scans performed on various samples is plotted in Fig. 5.3. The dark blue curve demonstrates the results for a piece of semi-insulating InP:Fe, while the green/red curves show the z-scans of high/low doped InGaAs grown on semi-insulating InP:Fe. A wafer of semi-insulating GaAs is z-scanned to verify the nonlinearity of the substrate z-scan (cyan curve).

Recall Fig. 5.1. Samples are z-scanned according to the two orientations in this figure. In the first orientation, THz pulses fall directly on the $In_{0.53}Ga_{0.47}As$ thin film. THz pulses exit this arrangement with electric field denoted by $\mathbf{E}_{t,1}$. Flipping the sample around, the samples are now in the second orientation, where THz pulses are incident to the substrate, and transmit with peak field $E_{t,2}$. In both instances we see that as a sample moves through the focus of a THz pulse, the normalized transmission peaks at the focus. We can gather that there are no

nonlinearities in the substrate, since both the InP substrate and the semi-insulating GaAs sample behave identically. The slight rise near $z = 45mm$ is the result of a slight misalignment in the optics collecting the transmitted THz pulses.

When the $In_{0.53}Ga_{0.47}As$ samples are scanned in the second orientation, we can see that the peak normalized transmission is larger in the first orientation. This gives rise to an optical diode, where nonlinear transmission is preferred in one direction of travel, over the other. The physical origins of this preference can be traced back to the transmission coefficients of the system. In the first orientation, we have already shown that the transmitted electric field has the form (recall eqn. 4.12)

$$\mathbf{E}_{t,1} = \frac{2}{1+n+Z_o\tilde{\sigma}d}\mathbf{E}_i. \tag{5.2}$$

It can be shown that when the sample is flipped around, the transmitted electric field has the form [10]

$$\mathbf{E}_{t,2} = \left(\frac{2n}{1+n}\right)\frac{2}{1+n+Z_o\tilde{\sigma}d}\mathbf{E}_i \tag{5.3}$$

demonstrating that

$$\frac{\mathbf{E}_{t,2}}{\mathbf{E}_{t,1}} = \frac{2n}{1+n}. \tag{5.4}$$

From eqn. 5.4 we fully expect that the sample should demonstrate preferential transmission in the $E_{t,2}$ orientation, since $2n/(1+n) \geq 1$ for $n > 1$.

The index of refraction (n) for our InP substrate was measured using THz time-domain spectroscopy. The results are plotted in Fig. 5.4, where we can see that the real index is approximately 4.1 in the range from 0.5 to 2 THz. As such, the transmitted electric field in the second orientation is approximately 1.6 times larger than the first orientation ($E_{t,2} = 1.6E_{t,1}$). Since so much more electric field arrives at the thin film for the second orientation, more electrons are excited high into the conduction band of the $In_{0.53}Ga_{0.47}As$ epilayer. This results in more intervalley scattering, a lower electron mobility and a higher overall transmissivity near the focus.

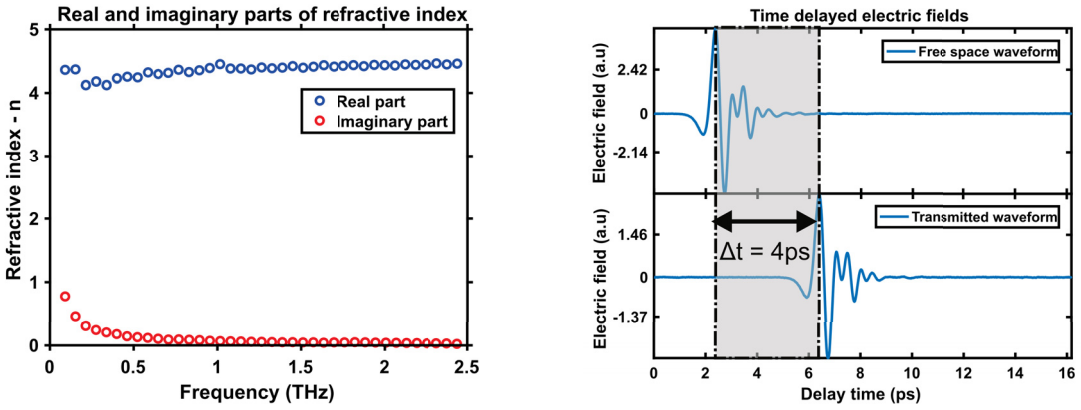

(a) (b)

Fig. 5.4 Using THz-TDS to measure InP substrate index of refraction. (a) Experimental values of the real and imaginary index of refraction for the InP substrate by THz-TDS. (b) Demonstrating the time shifted peak electric field induced by placing the InP onto the focus of the THz beam. Given that the time separation is $4ps$, and the substrate has a thickness of $350\mu m$, we can expect an index near 4.

5.2 Ultrafast imaging Z-scan

5.2.1 Details

Delving into a little bit of signal analysis here, the energy of a signal is given by

$$E = \frac{1}{Z}\int_{-\infty}^{\infty} |V(t)|^2 dt \tag{5.5}$$

where Z is the characteristic impedance of the transmission line through which the signal propagates. We can relate the voltage signal to an electric field through the definition of a voltage

$$\int \mathbf{E}(t)\cdot d\ell = \Delta V(t) \tag{5.6}$$

which implies that over small distances Δx, an electric field that is slowly varying in space will have the form

$$\mathbf{E}(t)\Delta x = \Delta V(t) = V(t) \tag{5.7}$$

where the final identity occurs by setting the reference voltage to zero. The electric field will be approximately constant for elctro-optic imaging data, since for a small area (ie, a circle with a 5 pixel radius) the electric field is pretty much constant. As such, eqn. 5.5 becomes

$$E = \frac{1}{Z}(2\pi r)^2 \int_{-\infty}^{\infty} |\mathbf{E}(t)|^2 dt \tag{5.8}$$

If a pulse is propagating in free space, then the characteristic impedance is just $Z = Z_o = 377\Omega$, so that

$$E = \frac{4\pi \times \pi (r)^2}{Z_o} \int_{-\infty}^{\infty} |\mathbf{E}(t)|^2 dt \propto \int_{-\infty}^{\infty} |\mathbf{E}(t)|^2 dt. \tag{5.9}$$

Equation 5.9 allows us to measure a time-domain waveform over a small area, and calculate a quantity proportional to the energy contained within a pulsed electric field.

With the above demonstration, we should be able to measure the energy of THz pulses directly from their time-domain waveforms. Therefore, we should expect to be able to take the ideas from the previous section and apply them here. To clarify, it should be possible to make a movie at a series of z locations on either side of a THz focus ($z = 0$). From these movies, we can extract an electric field from a small area of dimension (πr^2). Integrating the square of this electric field, we will obtain a quantity proportional to the energy at each z-position. Thus, using the time-domain waveforms, we should be able to repeat the measurements made in the previous section, only this time we use the electro-optic imaging system.

Movies were made using 75fs time steps and 100 counts of offset. With the full THz-energy recorded to be $1\mu J$, a standard z-scan was performed to find the maximum transmission at $z = 34mm$, as well as establish a baseline measurement. Maximum absorption bleaching (transmission enhancement) for the HD sample was found to be at $z = 34mm$. With respect to this maximum, movies were made at 1mm spacing starting from $+6mm$ and going to $-9mm$. Since we are using a camera system, the ICCD will have to be moved in tandem with the sample,

so that the ICCD is focusing on the sample at every step. This brought in an unforeseen issue with the camera translation stage; the ICCD camera began pointing away from the THz pulse at large z-values. Five signal images and five backgrounds were taken for every time step in order to enhance the signal to noise ratio in each movie. Waveforms were then extracted from a circle with a radius of $4px(26\mu m)$, encompassing an area of approximately $50px^2(2,234\mu m^2)$. The waveforms were then integrated according to eqn. 5.9.

As an additional measure of nonlinear transmission, we should be able to see a subpicosecond change in transmission when the peak electric field arrives at the sample. If intervalley scattering is happening on subpicosecond timescales, causing a boost in transmission near the peak electric field, then we should be able to see a z-dependent change in the peak-to-peak electric field symmetry. This will comprise a second measure of the nonlinearity experienced in a sample. The z-dependent pyroelectric energy measurement will serve as a benchmark for the results from the z-dependent peak-to-peak electric field differences and waveform energies.

5.2.2 Comparing results to baseline measurement

The results of the open-aperture imaging z-scan are plotted in Fig. 5.5, where the peak transmitted electric field seems to drift from the center of the image. This happens because the stage that supports the camera fails to maintain a collinear alignment at these positions. In the future, we will need a stronger stage in order to obtain even better results. For now, we find the approximate maximum (black circle) of each image and extract a waveform from the area around this maximum (blue curves).

The normalized integrated waveforms (blue circles), peak-to-peak electric fields (red circles) and the pyroelectric energies (green line) are plotted in Fig. 5.6. What we see is a boost in transmission at the focus of the THz pulse ($z = 34mm$). Integrating the squared waveform seems to under appreciate the transmitted energy, likely because in Fig. 5.5, the main pulse is barely in the time-window. This diminishes the integrated square because the area under the curve

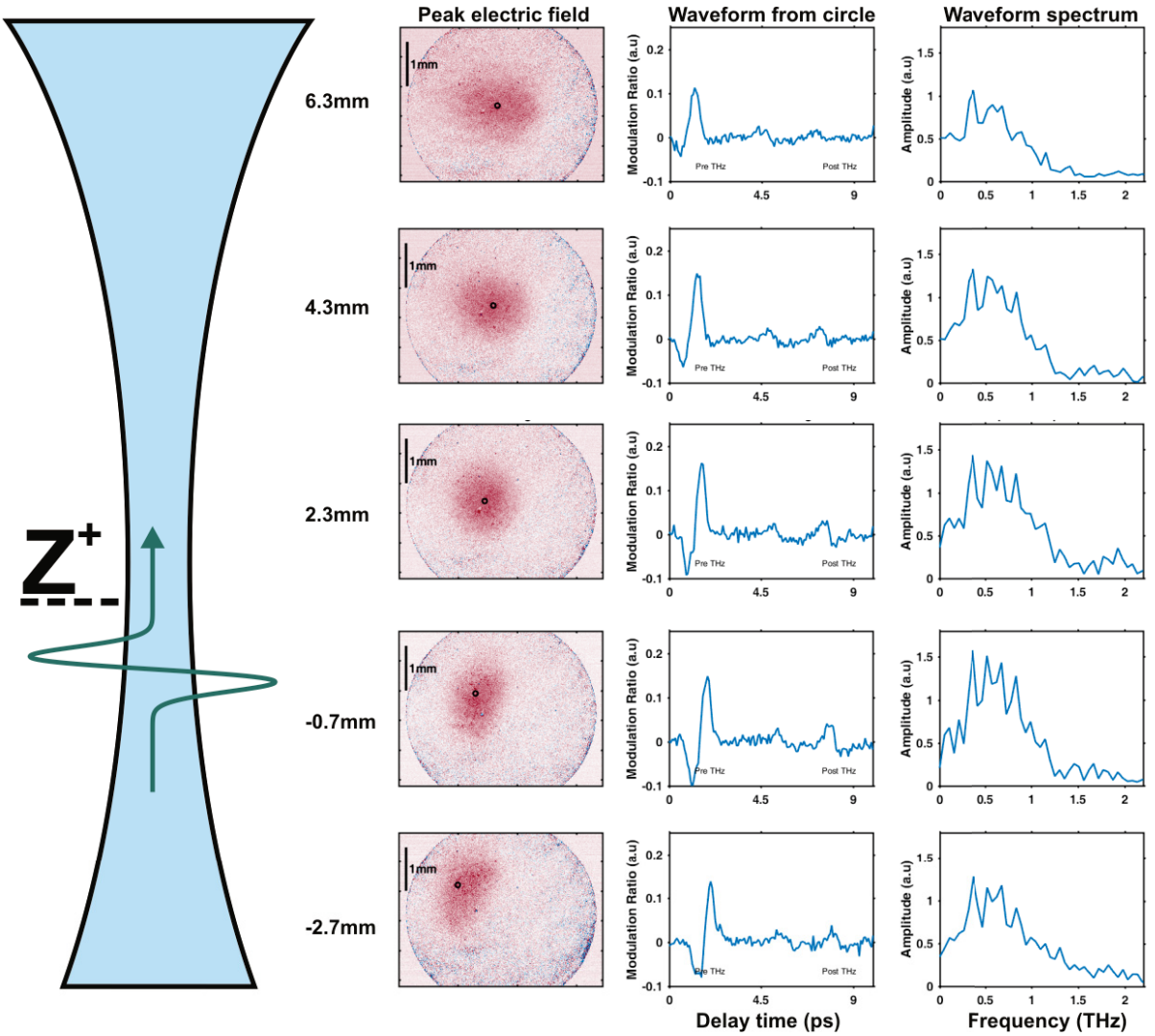

Fig. 5.5 Selection of waveforms from the imaging z-scan. Each of the peak electric field images are shown alongside their respective waveforms. Time-domain waveforms extracted by averaging the electric field within the area enclosed by black circles. As the sample moved through the focus of the THz pulse, the THz spot drifted out of frame. The drift stems from the camera stage not traveling perfectly collinear to the THz propagation axis. From the horizontal drift of 0.5mm over 9mm of travel, the camera stage is 6 degrees from the horizontal alignment. A similar calculation shows a vertical tilt of 10 degrees.

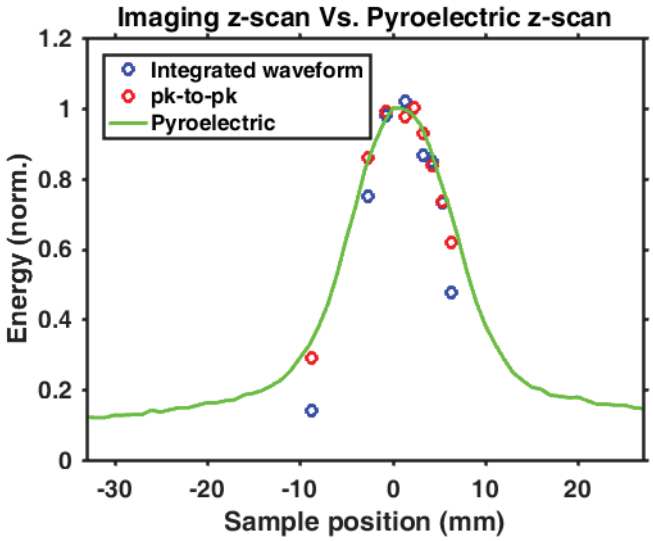

Fig. 5.6 Characterizing nonlinearity using three different techniques. The green line is a standard pyroelectric z-scan. The blue dots come from integrating the electric fields of the imaging z-scan, and the red dots come from the peak-to-peak electric field difference at each step of the imaging z-scan. With a pulse energy of $1\mu J$, the electric field was found to be 126kV/cm.

for early times is simply not present. Repeating this experiment would thus require a better centered time window over which we integrate. Overall the peak-to-peak difference seems to be a more appropriate measure of transmission nonlinearity, since it is not sensitive to the time window we choose to work with (insofar as the minimum and maximum electric fields are in the camera frame).

5.3 Near-field electro-optic sampling

In order to remove the presence of pulse-to-pulse differences, we installed a single-channel near-field EOS system, shown in Fig. 5.7. This system introduces a Thorlabs BP145b1 (45% Transmission) pellicle beam splitter (PBS), to split the imaging beam into 2 paths. One track is dedicated to measuring the background intensity I_{out} using a Thorlabs PDA100A photodiode (PD_1). A variable density filter (VDF) is used to attenuate I_{out} so that non-modulated difference can be zeroed ($I_{\text{in}} - I_{\text{out}} = 0$) with lock-in sensitivity.

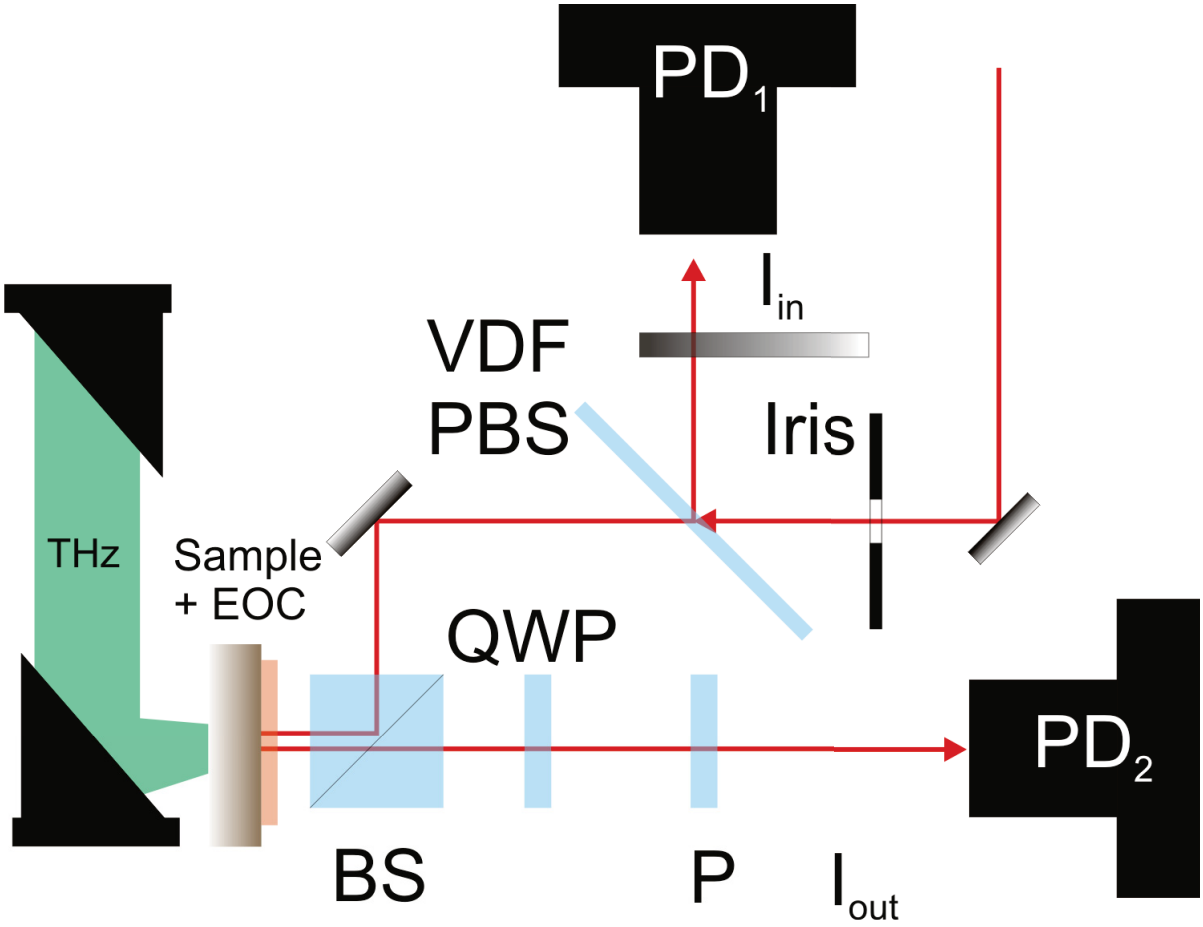

Fig. 5.7 Diagram of near-field electro-optic sampling system. PD denotes a photodiode, VDF is a variable density filter, PBS is a pellicle beam splitter, QWP is a quarter wavelplate, EOC is an electro-optic crystal, BS is a non-polarized beam splitter, P is a linear polarizer, with a horizontal transmission axis.

The alternate path shines the remaining light onto the sample by use of a non-polarizing beamsplitter (BS). This redirects 50% of the incident light onto the sample, where it is reflected back onto a quarter waveplate (QWP), and through a horizontally aligned nanoparticle linear polarizer (P). Finally, this pulse is incident to the other photodiode (same model as above, PD_2).

With the above arrangement, we use an amplifier locked-in to a 500 a Hz chopping frequency to measure I_{out}, I_{in} and $I_{\text{in}} - I_{\text{out}}$ to great accuracy. Finally, the ICCD camera hasn't been removed from the system, and so we have the ability to use an iris to spatially isolate the signal to only

those areas modulated by THz radiation.

Before finishing this section, we should devote some time to determining if this system is sensitive to the near-field phenomena we are interested in. The distance for which diffractive behavior can be considered near-field (R) is related to the wavelength of light diffracting (λ) and the largest physical dimension of the object upon which diffraction occurs (D) when

$$R < \frac{D^2}{\lambda}. \tag{5.10}$$

Ayesheshim measured a transient picosecond dipole induced by intervalley scattering that had dimensions on the order of $D = 1mm$ [10]. Thus, for a center wavelength of $f = 0.5THz$, $\lambda_o = 0.6mm$. When propagating in the electro-optic crystal, $\lambda = \lambda_o/n$. The index of refraction at THz wavelengths for is 2.8 for ZnTe [16] and 3.2 for GaP [43]. Thus, $\lambda \approx \lambda_o/3$, implying that

$$R < \frac{(1mm)^2}{0.6mm/3} = \frac{3mm}{0.6} = 5mm. \tag{5.11}$$

So long as the THz pulses do not travel for longer than 5mm within the electro-optic crystal, the near-field signatures of nonlinear transmission will be present in the time-domain waveforms.

5.4 Experimental details and preliminary results

The experiment this time is quite simple. We measured the transmitted THz electric field through a control sample (substrate of InP) and a LD sample. By integrating the time-domain electric field, we can expose the presence of any subpicosecond nonlinearity, ie,

$$\text{Offset}(t) = \int_{-\infty}^{t} \mathbf{E}(t')dt'. \tag{5.12}$$

Fig. 5.8 shows the results of the measurements described above. Given the subpicosecond nature of intervalley scattering, we expect to see the presence of a subpicosecond reshaping of

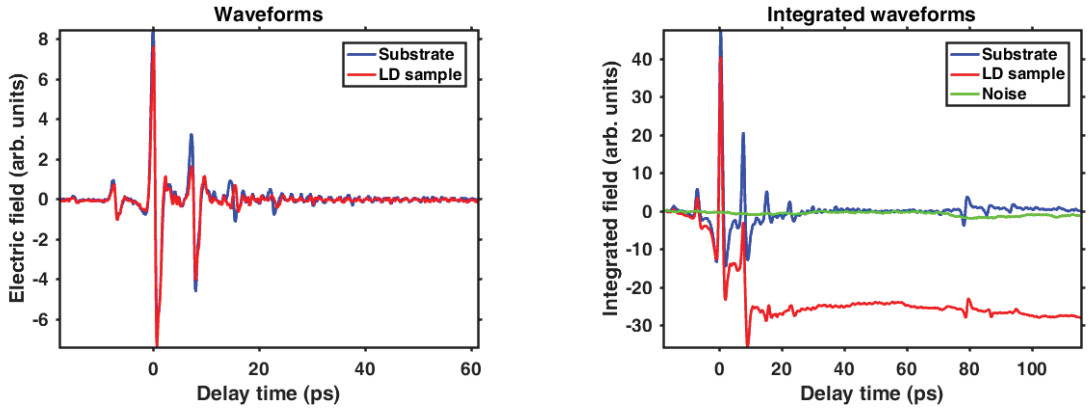

(a) (b)

Fig. 5.8 Results from near-field electro-optic sampling. (a) The full time-domain window of the THz waveforms measured. The blue curve comes from a transmission through the substrate, and the red curve comes from nonlinear transmission through the LD sample. (b) Running integrals of the waveforms from (a). The green curve is the integral of a noise data set.

the THz pulse, induced by intervalley scattering. This reshaping of the transmission waveforms will be prominent in the time-integral of a THz waveform, bearing the form of a net integral. This integral is presented in Fig. 5.8, which shows a distinct offset in the LD transmission waveform that isn't present in either the control sample or the noise.

This result agrees with the expectation from Fig. 4.6 (b), where the dynamic Drude model shows the non-zero nature of the integrated waveforms should diverge from zero. Further optimization and testing must be done to solidify these results, by exploring the field-dependent nature of this nonlinearity. Furthermore, as the temperature of the conducting film is lowered, we expect to see the duration of the intervalley scattering process increase, since the phonon scattering rate that drives this nonlinearity will be reduced. Replicating these results with an electro-optic imaging scheme may yield valuable insight to the use of intervalley scattering to generate a picosecond transient current, since a local radiating dipole on the surface of the conducting thin film could be an indication that heavier electrons moving alongside lighter electrons creates a local transient current [10]. In the future, this ultrafast voltage transient can be used to create unbiased photodetectors that work at THz frequencies.

5.5 Fitting to dynamic drude model

In Appendix A, the algorithm that is used to fit data to the dynamic Drude model is provided. Using the near-field EOS system, we can measure a THz waveform upon transmission through the InP substrate. Furthermore, we can take this waveform and run it through the algorithm outlined in Chapter 4, and compare it to the waveform we measure upon transmission through a doped epilayer.

The results of a preliminary measurements are shown in Fig. 5.9. By plotting the normalized waveforms, we can see any asymmetry that develops in the waveforms passing through the LD sample. Looking at times just after the peak electric field arrives, we can see that the THz minimum is much deeper when a THz pulse passes through the LD sample. This is an indication that intervalley scattering is enhancing the transmissivity of the LD thin film before the THz pulse has fully left the sample.

The actual curve fitting process results are shown in Fig. 5.10, where the simulation was run for an electric field range from 40 to 160kV/cm. The algorithm seeks the electric field that minimizes the difference between the simulated and measured integrated waveforms, over the range of electric fields specified by the user. Doing this, we can see the first evidence of non-zero integration of a near-field waveform.

The waveforms taken in Fig. 5.10 were acquired as a proof of concept, and as a result the source wasn't optimized, nor was the THz pulse properly characterized before the measurement was taken. By optimizing the source to generate pulses of $1.1\mu J$, and doing an open aperture energy z-scan of the LD sample, the sample was exposed to a peak electric field of 133kV/cm. Figure 5.11 shows the results of the open-aperture z-scan and the thermal profile of the THz pulse, and Fig. 5.12 shows the data retrieved through near-field EOS. In Fig. 5.12 (a) the emitted waveforms for the substrate (blue) and LD sample (red) are shown. By taking the substrate waveform and running it through the intervalley scattering algorithm, we generate

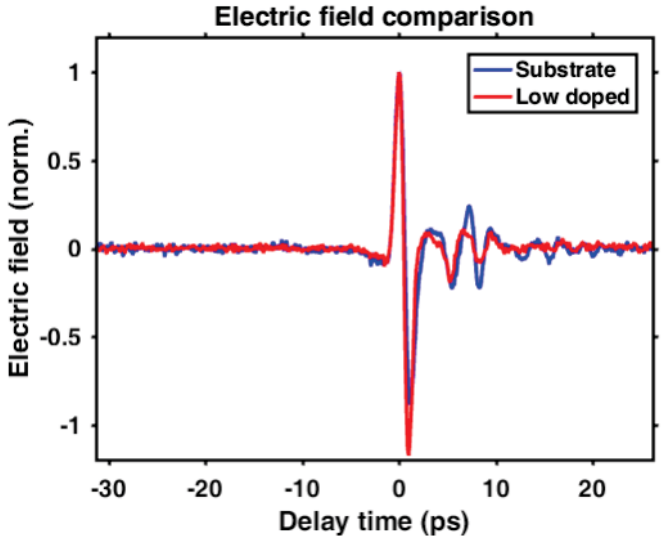

Fig. 5.9 Preliminary input data for fitting to dynamic Drude model. (a) Full time-domain window of the THz pulses measured after transmission through the substrate (blue) and LD sample (Red). The substrate waveform from this data set will be entered into the dynamic Drude simulation shown in Fig. 4.5.

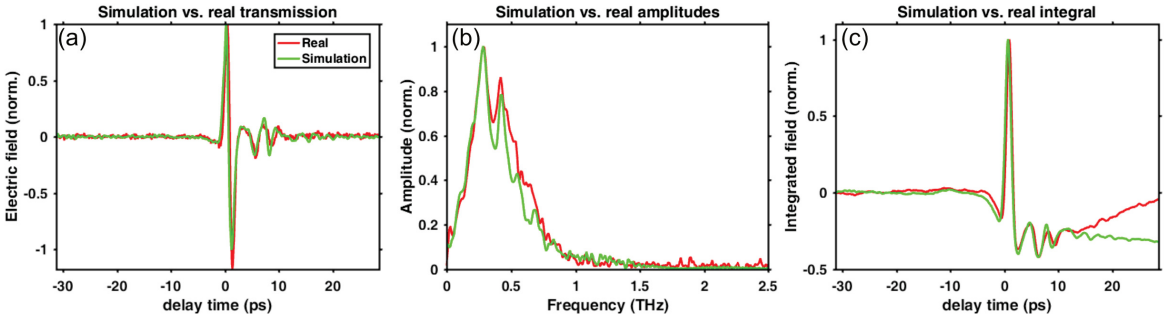

Fig. 5.10 Demonstrating the results of fitting to a dynamic Drude model. (a) Measured (red) and simulated (green) time-domain waveforms. The peak electric field of the simulated waveform was estimated to be 72kV/cm. (b) Fourier transforms of the time-domain waveforms. (c) The integrated waveforms from (a). The integrated waveform from the measured nonlinear transmission diverges at late delay times because of a misalignment between the imaging line and the iris used to isolate the THz waveforms.

a simulated waveform (green). A zoom in of these waveforms is shown in Fig. 5.12 (c) for clarity. Integrating the waveforms from panel (a), we construct Fig. 5.12 (b), where we see that the integrated waveforms have very different behavior. The LD integral converges on a non-zero value, while the substrate integral clearly converges on zero at later times. Panel (d) shows the results of panel (b), zoomed in to the same region as panel (c). It appears as though the simulation is not able to incorporate the effects of reflected THz pulses, since it converges quite well with the measured nonlinear transmission at for times less than 25ps, and flattens out afterwards. The simulation requires the user to input a peak electric field value, as well as a normalized waveform that is to undergo intervalley scattering. In order to find an optimal peak electric field, the algorithm in Appendix A.2.2 was used. It attempts to find the peak electric field that minimized the difference between the simulated output and the measured waveform. It works by running two simulations. One simulation occurs at an upper bound electric field, while the other simulation occurs at a lower peak electric field. The electric field that produces a waveform with the best fit is selected as the new upper bound. For the fitting shown in Fig. 5.11, a peak electric field of 65kV/cm (roughly half of the measured peak electric field) was reported from the minimization algorithm. This explains why the later time intervals do not agree with early times, since subsequent reflections would have smaller peak electric fields that are not strong enough to drive further intervalley scattering. In the future, it should be possible to take this one-dimensional simulation and apply it to the imaging system in a pixel-by-pixel fashion. This could provide insight on the physical origins of the current responsible for the near-field radiation pattern seen in previous work [10].

For the simulation, it was assumed that the sample thickness was $500\mu m$, the effective electron masses for the Γ and L-valleys are $0.04m_e$ and $0.26m_e$ respectively. The threshold energy of eqn. 4.37 was given as $E_{th} = 0.13eV$, with a half-window of $0.06eV$. The carrier density was given as $n_e = 3.5 \times 10^{23} m^{-3}$, along side $\tau_{L\to\Gamma} = 4ps$, $\tau_{\Gamma\to\Gamma} = 0.1ps$,$\tau_{L\to L} = 0.06ps$. The initial momentum of the electrons in the system is zero, and the L-valley population is assumed to begin at zero as well. All of the remaining parameters are given in Appendix A.2.1.

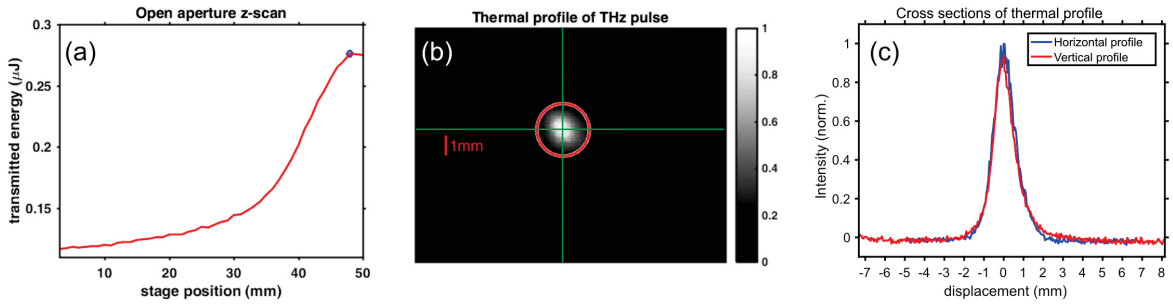

Fig. 5.11 Characterizing THz source before measuring near-field waveforms. (a) Open-aperture z-scan of LD sample, showing the location of the peak nonlinearity at 48mm. Due to the installation of a new sample holder, the entire baseline could not be measured. (b) Thermal image of the THz intensity profile. The THz spot has a $1/e^2$ diameter of 2.6mm (red circle). The energy of the THz pulse is measured to be $1.1\mu J$, corresponding to a peak electric field of 133kV/cm. (c) The vertical and horizontal cross sections extracted from the green lines in (b).

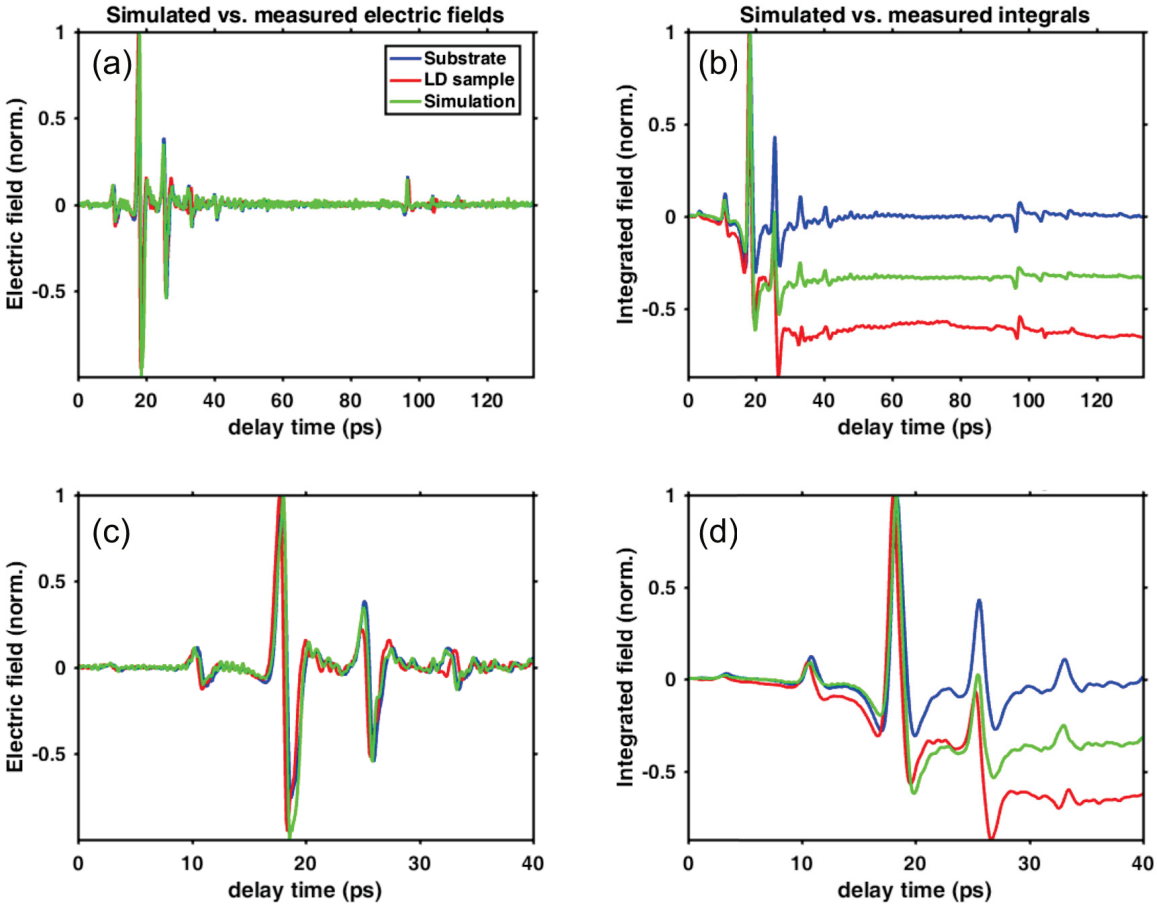

Fig. 5.12 Fitting near-field waveforms using dynamic Drude model. (a) Normalized THz waveforms from simulation and measurement. Peak THz electric field incident to sample is 133kV/cm. (b) Integrated waveforms from (a). (c) Zoomed in view of the waveforms from (a). (d) Integrals of waveforms shown in (c).

Chapter 6

Conclusions and Outlook

THz electro-optic imaging is a tool capable of capturing the near-field, subpicosecond evolution of intense THz electric fields as they transmit through doped semiconductors. In this thesis we have explored the principles of electro-optic imaging, and showed that over-rotation can occur if the imaging electro-optic crystal is not carefully selected. We have seen that choosing an electro-optic crystal with a low electro-optic coefficient, as well as having a reduced thickness, results in a more gaussian electric field profile, accompanied by a modulation ratio well within the linear regime of detection.

We have performed the first ultrafast imaging z-scan of intense THz pulses, in order to explore the near-field behavior of the transmission of intense THz pulses through $In_{0.53}Ga_{0.47}As$ thin films. It was shown that integrating the modulus square of near-field waveforms can be an effective measure of THz-pulse-induced absorption bleaching in n-doped $In_{0.53}Ga_{0.47}As$ thin films, by comparing our measurements to benchmark pyroelectric z-scans. From the imaging z-scan, it was also shown that the z-dependent peak-to-peak electric field difference can indicate the presence of absorption bleaching through comparison to the same pyroelectric benchmark. In the future, it may be possible to use an intervalley scattering simulation to interpret local electron velocities that give rise to dipole radiation patterns seen in previous work [10].

We installed a single-channel electro-optic sampling system within the existing electro-optic imaging setup in order to measure the ultrafast near-field evolution of subpicosecond changes in the conductivity of $In_{0.53}Ga_{0.47}As$ thin films. From this, we have seen evidence of a rectification process occurring in a heavily doped $In_{0.53}Ga_{0.47}As$ epilayer that gives rise to a non-zero integrated THz electric field. We then attempted to use a dynamic Drude simulation to generate THz electric fields that share similar features to those seen in experiment. More work needs to be done in order to properly demonstrate agreement between simulation and measurements, as the work presented here stands as a preliminary attempt.

Looking forward, the electro-optic imaging system has great potential. One route that can be explored is taking the $In_{0.53}Ga_{0.47}As$ samples to low temperatures. We can lower the temperature of our samples, perform an ultrafast imaging z-scan, and measure the absorption bleaching induced by THz pulses. As the temperature is lowered, the increase in electron mobility will lower the electric field threshold for intervalley scattering, enabling intervalley scattering at lower electric field strengths than room temperature values quoted in literature [12]. By achieving a lower threshold fields, it may be possible to make an efficient saturable absorber for ultrafast terahertz signals, similar in principle to those presented in previous work [44].

Using only a reflection coated wafer of GaP, one could presumably measure the spatial characteristics of THz electric fields undergoing a Gouy phase transition without the need for elaborate detection schemes [45]. Experimentally, this measurement can be done easily using the ultrafast imaging z-scan presented in this thesis. In doing so, we can easily reconstruct a three-dimensional map of a THz carrier envelope undergoing a Gouy phase transition.

References

[1] National Museum of American History. Capturing the Moment pg. 1.

[2] T. Hartwick, D. Hodges, D. Barker, and F. Foote. Far infrared imagery. *Applied Optics*, 15(8):1919–1922, 1976.

[3] B. B. Hu and M. C. Nuss. Imaging with terahertz waves. *Optics Letters*, 20(16):1716–1718, 1995.

[4] W. Chan, J. Deibel, and D. Mittleman. Imaging with terahertz radiation. *Reports on Progress in Physics*, 70(8):1325–1379, 2007.

[5] F. Blanchard, A. Doi, T. Tanaka, and K. Tanaka. Real-Time, Subwavelength Terahertz Imaging. *Annual Review of Materials Research*, 43(1):237–259, 2013.

[6] F. Blanchard and K. Tanaka. Improving time and space resolution in electro-optic sampling for near-field terahertz imaging. *Opt. Lett.*, 41(20):4645–4648, 2016.

[7] R. Kersting, F. Buersgens, G. Acuna, and G. C. Cho. Terahertz near-field microscopy. *Advances in Solid State Physics*, 47:203–222, 2008.

[8] T. Cocker, D. Peller, P. Yu, J. Repp, and R. Huber. Tracking the ultrafast motion of a single molecule by femtosecond orbital imaging. *Nature*, 539(7628):263–267, 2016.

[9] V. Jelic, K. Iwaszczuk, P. Nguyen, C. Rathje, G. Hornig, H. Sharum, J. Hoffman, M. Freeman, and F. Hegmann. Ultrafast terahertz control of extreme tunnel currents through single atoms on a silicon surface. *Nature*, 13(111):33–36, 2017.

[10] A. Ayesheshim. *High-power Terahertz Pulse Generation and Nonlinear Terahertz Carrier Dynamics in Semiconductors*. PhD thesis, University of Alberta, Dept. of Physics, Canada, 2015.

[11] F. H. Su, F. Blanchard, G. Sharma, L. Razzari, A. Ayesheshim, T. Cocker, L. Titova, T. Ozaki, J. Kieffer, R. Morandotti, M. Reid, and F. Hegmann. Terahertz pulse induced intervalley scattering in photoexcited GaAs. *Optics express*, 17(12):9620–9629, 2009.

[12] L. Razzari, F. H. Su, G. Sharma, F. Blanchard, A. Ayesheshim, H. C. Bandulet, R. Morandotti, J. C. Kieffer, T. Ozaki, M. Reid, and F. A. Hegmann. Nonlinear ultrafast modulation of the optical absorption of intense few-cycle terahertz pulses in n -doped semiconductors. *Physical Review B - Condensed Matter and Materials Physics*, 79(19):3–6, 2009.

[13] R. Boyd. *Nonlinear Optics*. Elsevier, third edition, 2008.

[14] C. Rulliere. *Femtosecond laser pulses*. Springer, 1998.

[15] J.D Jackson. *Classical Electrodynamics*. Wiley, third edition, 2007.

[16] Y. S. Lee. *Principles of terahertz science and technology*. Springer, dec 2009.

[17] K. L. Yeh, J. Hebling, M. C. Hoffmann, and K. A. Nelson. Generation of high average power 1 kHz shaped THz pulses via optical rectification. *Optics Communications*, 281(13):3567–3570, 2008.

[18] H. Hirori, A. Doi, F. Blanchard, and K. Tanaka. Single-cycle terahertz pulses with amplitudes exceeding 1 MV/cm generated by optical rectification in LiNbO3. *Applied Physics Letters*, 98(9), 2011.

[19] J. Hebling, G. Almasi, I. Kozma, and J. Kuhl. Velocity matching by pulse front tilting for large area THz-pulse generation. *Optics Express*, 10(21):1161, 2002.

[20] D. H. Auston. Subpicosecond electro-optic shock waves. *Applied Physics Letters*, 43(8):713–715, 1983.

[21] Z. Wang, F. H. Su, and F. A. Hegmann. Ultrafast imaging of terahertz Cherenkov waves and transition-like radiation in LiNbO3. *Optics Express*, 23(6):8073–8086, 2015.

[22] D. Mittleman. *Sensing with Terahertz Radiation*. Springer-Verlag Berlin Heidelberg New York, 2003.

[23] LaVision GmbH. *PicoStarHR Manual*. LaVision, G\"ottingen, 2003.

[24] Z. Wang. *Ultrafast imaging of terahertz pulses*. Phd, University of Alberta, 2013.

[25] F. Blanchard, A. Doi, T. Tanaka, H. Hirori, H. Tanaka, and Y. Kadoya. Real-time terahertz near-field microscope. *Optics express*, 19(9):3523–3525, 2011.

[26] A. Doi, F. Blanchard, T. Tanaka, and K. Tanaka. Improving spatial resolution of real-time Terahertz near-field microscope. *Journal of Infrared, Millimeter, and Terahertz Waves*, 32(8-9):1043–1051, 2011.

[27] M. C. Hoffmann. Nonlinear Terahertz Spectroscopy. In Kai-Erik Peiponen, , Axel Zeitler, , and Makoto Kuwata-Gonokami, editors, *Nonlinear Terahertz Spectroscopy*, pages 355—-388. 2013.

[28] P. Klarskov, A. C. Strikwerda, K. Iwaszczuk, and P. U. Jepsen. Experimental three-dimensional beam profiling and modeling of a terahertz beam generated from a two-color air plasma. *New Journal of Physics*, 15, 2013.

[29] W. M. Haynes. *CRC Handbook of Chemistry and Physics*. CRC Press, 97th edition, 2017.

[30] D. Pozar. *Microwave Engineering Fourth Edition*. John Wiley & Sons, fourth edition, 2005.

[31] E. Hecht. *Optics*. Addison-Wesley, fourth edition, 2002.

[32] M. C. Nuss and J. Orenstein. *Terahertz time-domain spectroscopy*, pages 7–50. Springer Berlin Heidelberg, Berlin, Heidelberg, 1998.

[33] M. Grundmann. *The Physics of Semiconductors*. Springer, 2006.

[34] W. H. Press, S. A. Teukolsky, W. T. Vetterling, and B. P. Flannery. *Numerical Recipes 3rd Edition: The Art of Scientific Computing*. Cambridge University Press, 3 edition, 2007.

[35] E. M. Conwell and M. Vassel. High-Field Distribution Function in GaAs. *IEEE Transactions on Electron Devices*, 13(1), 1966.

[36] G. Q. Chen, J. W. Jerome, C. W. Shu, and D. Wang. Geometric Structure and Symmetry Properties. In J. Jerome, editor, *Modelling and Computation for Applications in Mathematics, Science, and Engineering*, pages 130–140. Oxford University Press, Oxford, 1998.

[37] A. Marcello Anile and S. D. Hern. Two-valley Hydrodynamical Models for Electron Transport in Gallium Arsenide : Simulation of Gunn Oscillations. *VLSI Design*, 15(4):681–693, 2002.

[38] M. Sheik-Bahae, Al. A. Said, T. H. Wei, D. J. Hagan, and E. W. Van Stryland. Sensitive Measurement of Optical Nonlinearities Using a Single Beam. *IEEE Journal of Quantum Electronics*, 26(4):760–769, 1990.

[39] M. Dinu, F. Quochi, and H. Garcia. Third-order nonlinearities in silicon at telecom wavelengths Third-order nonlinearities in silicon at telecom wavelengths. *Applied Physics Letters*, 82(18), 2003.

[40] B. Gu, Y. X. Fan, J. Wang, J. Chen, J. Ding, H. T. Wang, and B. Guo. Characterization of saturable absorbers using an open-aperture Gaussian-beam Z scan. *Physical Review A - Atomic, Molecular, and Optical Physics*, 73(6):1–4, 2006.

[41] L. Yang, R. Dorinsville, Q. Z. Wang, P. X. Ye, R. R. Alfano, R. Zamboni, and C. Taliani. Excited-state nonlinearity in polythiophene thin films investigated by the Z-scan technique. *Optics Letters*, 17(5):323–325, 1992.

[42] B. E. A. Saleh and M. C. Teich. *Fundamentals of Photonics*. John Wiley & Sons, second edition, 2007.

[43] H. Hirori, K. Shinokita, M. Shirai, S. Tani, Y. Kadoya, and K. Tanaka. Extraordinary carrier multiplication gated by a picosecond electric field pulse. *Nature communications*, 2(May):594, 2011.

[44] M. C. Hoffmann and D. Turchinovich. Semiconductor saturable absorbers for ultrafast terahertz signals. *Appl. Phys. Lett.*, 96(1151110), 2010.

[45] D. Hoff, M. Krüger, L. Maisenbacher, A. M. Sayler, G. G. Paulus, and P. Hommelhoff. Tracing the phase of focused broadband laser pulses. *Nature Physics*, (July):1–6, 2017.

Appendix A

Computation and Imaging

A.1 Image Processing in MATLAB

A.1.1 Reducing images

```
1  function [Reduced_images,Reduced_matrix ] = Reduce_mean_shutter(
       Num_images,Offset,N)
2  % REDUCE_MEAN_SHUTTER
3  % This function is designed to upload 2 data sets and process them side
       by side.
4  %               1.) Load in Data image
5  %               2.) Load in Background image
6  %               3.) (Image - Bkgrd)./Bkgrd = Signal (single channel)
7
8  %% Input Variables
9  %               Num_images     = Number of images per data set
10 %               eg,                = 256;
11 %
12 %               Offset         = Counts of offset used in LaVision
13 %               eg,            = 500;
14 %
15 %               N              = Number of data sets to average over
16 %       eg,            = 5
17 %
18 %%%%%%%%%%%%%%%%%%%%%%%%%%%%%%%%%%%%%%%%%%%%%%%%%%%%%%%%%%%%%%%%%%%%%%%
19
20 %% Output Variables
21 %               Reduced_images = Output cell array;
22 %                      = 1xN cell;
23 %       Reduced_matrix = 3-D matrix of output values;
24 %               eg,                = 520x688x256;
```

```
25 %
26 %%%%%%%%%%%%%%%%%%%%%%%%%%%%%%%%%%%%%%%%%%%%%%%%%%%%%%%%%%%%%%%%%%%%%%%%
27
28
29 %% This is the preamble information
30
31
32
33
34 tic;
35
36 Temp_image = zeros(520,688,N);
37 Temp_Bkgrd = zeros(520,688,N);
38 file_dir = cell(N,Num_images/2);
39
40
41 for j = 1:N
42 file_dir{j} = fullfile(uigetdir('',sprintf('Please select %i data
      directory',j)));
43 end
44
45
46
47
48
49 %% Making a list of strings with file directories
50
```

```
51
52              fprintf('Please wait while images are processed.\n')
53          %Making a cell array of strings of image locations
54                  Image_cell_string = cell(N,Num_images/2);
55                  Bkgrd_cell_string = cell(N,Num_images/2);
56              for j = 1:N
57                  Image_cell_string{j,1} = fullfile(file_dir{j},'Image\\
                        B00001.txt');
58                  Bkgrd_cell_string{j,1} = fullfile(file_dir{j},'Image_01\\
                        B00001.txt');
59                  for i= 2:2:8
60                      Image_cell_string{j,i/2 +1} =  fullfile(file_dir{j},
                            sprintf('Image_0%i\\B00001.txt',i));
61                      Bkgrd_cell_string{j,i/2 +1} = fullfile(file_dir{j},
                            sprintf('Image_0%i\\B00001.txt',i+1));
62                  end
63                  for i = 10:2:Num_images-2
64                      Image_cell_string{j,i/2 +1} = fullfile(file_dir{j},
                            sprintf('Image_%i\\B00001.txt',i));
65                      Bkgrd_cell_string{j,i/2 +1} = fullfile(file_dir{j},
                            sprintf('Image_%i\\B00001.txt',i+1));
66                  end
67              end
68
69
70  %% Using the list of strings to open one image at a time
71
```

```
72              Reduced_matrix = zeros(520,688,Num_images/2);
73              Reduced_images = cell(1,Num_images/2);
74          %Generating the data cell array and matrix
75              for i = 1:Num_images/2
76                  for j = 1:N
77                      Temp_image(:,:,j) = single(importimage(
                            Image_cell_string{j,i}));
78                      Temp_Bkgrd(:,:,j) = single(importimage(
                            Bkgrd_cell_string{j,i}));
79                  end
80                      Mean_image = mean(Temp_image,3);
81                      Mean_Bkgrd = mean(Temp_Bkgrd,3);
82                      Reduced_images{i} = (Mean_image-Mean_Bkgrd)./(
                            Mean_Bkgrd-Offset);
83                      Reduced_matrix(:,:,i) = Reduced_images{i};
84              end
85  toc;
86
87  end
```

A.1.2 3D fast fourier transform

```
function [Amplitudes, Frequencies,FFT] = FFT_three_d(wave, Sampling_Frequency)
%% Description:
%
% FFT.m is designed to take an 3D matrix, and perform a standard single
% sided FFT. It outputs a frequency spectrum and an amplitude matrix.
% %%%%%%%%%%%%%%%%%%%%%%%%%%%%%%%%%%%%%%%%%%%%%%%%%%%%%%%%%%%%%%%%%%%%%%%%%%

%% Variables:
%
% wave                = vector of values to be transformed
%   eg,               = Waveform
%
% Sampling_Frequency = 1/(time between data points)
%   eg,               = Output_frequencies
% %%%%%%%%%%%%%%%%%%%%%%%%%%%%%%%%%%%%%%%%%%%%%%%%%%%%%%%%%%%%%%%%%%%%%%%%%%

tic;
%% Calculate frequency spectrum
    % fftlength
        NFFT=2^nextpow2(length(wave(1,1,:)));
    % Get the sampling frequency
        Fs=Sampling_Frequency;
    % FFT actual information goes from DC to Nyquist Frequency
```

```
22          Frequencies=Fs/2*linspace(0,1,NFFT/2+1);
23
24  %% Generate amplitudes
25          FFT = fft(wave,NFFT,3);
26          Amplitudes = abs(fft(wave,NFFT,3));
27          Amplitudes = Amplitudes(:,:,1:NFFT/2+1);
28          FFT = FFT(:,:,1:NFFT/2 +1);
29  toc;
30  end
```

A.1.3 Converting Lock-in Signal to Electric Field

```
function [ E_THz ] = Electric_field(Waveform,N,Modulation_ratio,EO_Crystal)
%% Description:
%Electric_field takes in an EOS wave form and spits out the equivalent
%Out put E_THz is a vector in kV/cm using Hiriori,Tanaka,Blanchard,Doi 2011
%APL: Single—cycle terahertz pulses with amplitudes exceeding
%1 MV/cm generated by optical rectification in LiNbO3
% %%%%%%%%%%%%%%%%%%%%%%%%%%%%%%%%%%%%%%%%%%%%%%%%%%%%%%%%%%%%%%%%%%%%%%%%%%

%% Variables:
%
% Waveform         = Normalized output Va—Vb from lock in amplifier.
%   eg,            = [vector]
%
% N                = number of silicon attenuation wafers.
%   eg,            = 3
%
% Modulation_ratio = A—B/A+B from Oscilloscope
%   eg,            = 34 mV/1000mV
%
% EO_Crystal       = What type of crystal are you using? (GaP or ZnTe)
%   eg,            = 'ZnTe'
```

```
% %%%%%%%%%%%%%%%%%%%%%%%%%%%%%%%%%%%%%%%%%%%%%%%%%%%%%%%%%%%%%%%%%%%%%%%%%%%%%%%%%

% %%%%%%%%%%%%%%%%%%%%%%%%%%%%%%%%%%%%%%%%%%%%%%%%%%%%%%%%%%%%%%%%%%%%%%%%%%%%%%%%%
%% Outputs:
%
% E_THz             = Electric field [kV/cm]
%   eg,             = [Vector]
%
% %%%%%%%%%%%%%%%%%%%%%%%%%%%%%%%%%%%%%%%%%%%%%%%%%%%%%%%%%%%%%%%%%%%%%%%%%%%%%%%%%


%% Preamble
Waveform = Waveform./max(Waveform);

switch EO_Crystal
    case 'ZnTe'
    % ZnTe Properties
    lambda_o = 805E-9; %[m]
    n_o = 2.8529; %Li. 1984
    eo_coeff = 4.04E-12;%Yun-Shik Lee pg. 93 [m/V]
    t_si = 0.7; % Hiriori,Doi,Blanchard,Tanaka 2011
```

```
42      t_znte = 0.479;
43          % http://www.ncbi.nlm.nih.gov/pmc/articles/PMC4791559/
44          % Says t_ZnTe = 2/(n_thz+1) where n_thz is the index of
                refraction of
45          % 1THz light in ZnTe
46      L = 0.5E-3; %Thicnkness = 500 micrometers
47
48      E_THz = asin((Modulation_ratio))*((lambda_o.*Waveform)./(2*pi*(n_o^3)
            *eo_coeff*t_znte*(t_si.^N)*L)).*(1E-5);
49
50      case 'GaP'
51      % GaP Properties
52      lambda_o = 800E-9;
53      t_GaP = 0.46; % Hiriori,Doi,Blanchard,Tanaka 2011
54      t_si = 0.7;
55      n_o = 3.2; % Hiriori,Doi,Blanchard,Tanaka 2011
56      eo_coeff = .88E-12; % Hiriori,Doi,Blanchard,Tanaka 2011
57      L = 200E-6;
58
59      E_THz = asin((Modulation_ratio))*((lambda_o.*Waveform)./(2*pi*(n_o^3)
            *eo_coeff*t_GaP*(t_si.^N)*L)).*(1E-5);
60  end
61
62
63  %% Output vector
64  E_THz;
65
```

```
66
67 end
```

A.2 Dynamic Drude model

A.2.1 Model

```
function [Output] = thin_film_1D(E_max,E_noise)
%     disp('Start')
%     disp(' ')
    %% ── Description ──
    %   This script takes in THz waveform data and models the field
    %   transmitted through a sheet of doped InGaAs. A thin film
    %   approximation is used and carrier momemtum is calculated using
        RK4.
    %   Scattering rate is chosen using a smooth, monotomic threshhold
    %   function.
    %   Original Author: Ayesheshim Kebie Ayesheshim
    %   Improved and added onto by Kameron Palmer and Charles Jensen

    %% ── Inputs ──
    %   o   (Normalized, single column) THz waveform data file
    %   o   physical parameters adjusted in a following section

    %% ── Outputs ──
    %   o   Calculates and plots emmitted (emt) and incidental (inc)
        fields
    %   o   Integral of emt and inc
    %   o   Writes out select values of interest

    %% ── Physical Constants ──
```

```
23      e0 = 1.60217653e-19;                          %electron charge [C]
24      me = 9.109389e-31;                            %electron mass [Kg]
25      kb = 1.380658e-23;                            %boltzmann constant [J/K]
26      T0 = 300;                                     %temperature [K]
27      Y0 = 1/377;                                   %admittance of free space
            [1/Ohm]
28
29      %% ---  System Parameters  ---
30      %   Values related to the THz beam
31      [t,THz] = import_waveform('C:\Charles\Video bin\Movies and data
            \2017\31_May_017\31\Substrate');%uigetfile('*.*','Please select a
            THz waveform')));      %THz waveform data file
32      THz = flipud(THz);
33      THz = THz(1:end - 1);
34      THz = THz -mean(THz(530:760));
35      THz = Waveform_smooth(t,THz./max(THz),E_noise,2.5);         %
            Smoothing waveform with Tukey window
36      t = t.*1e-12;
37      %E_max = 60e+5;                        %Max value of THz pulse, [V/m].
            1e5 V/m = 1kV/cm
38      E_inc = E_max.*THz;                   %Create array of incident pulse,
            [V/m]
39      t_run = (t(end)-t(1));                      %Time interval of pulse, [
            s]
40
41      %% ---  Sample Parameters  ---
42      %   Values of constants related to the sample
```

```
43      n_elec = 3.5e23;                    %number density of electrons,
           [1/m^3]
44      d_thick = 0.5e-6;                   %thickness of the sample, [m]
45      n = 3.001;                          %index of material, [1]
46      mG = 0.04*me;                       %effective mass in G-valley, [Kg]
47      mL = 0.26*me;                       %effective mass in L-valley, [Kg]
48      aG = 1.33/e0;                       %parabolicity of the G-valley,
           [1/eV]
49      aL = 0.59/e0;                       %parabolicity of the L-valley,
           [1/eV]
50
51      %% --  Scattering Parameters  --
52      %   Intervalley scattering is handled by assuming the rate is 0 for
           low
53      %   energy, a set constant for high energy, and a smooth intermediate
54      %   function over a set window with a chosen width and center
55      enth = 0.13*e0;                    %center of the smooth function
           window, [eV]
56      de = (0.12-0.06)*e0;                       %half width of window, [eV
           ]
57      tGL = 0.030e-12;                    %G -> L max scattering rate, [s]
58      tLG = 4.000e-12;                    %L -> G scattering time, [s]
59      tGG = 0.100e-12;                    %G -> G scattering time, [s]
60      tLL = 0.060e-12;                    %L -> L scattering time, [s]
61
62      %% --  Run Parameters  --
63      format long
```

```
64      N = length(E_inc);                          %number of data points
65      t = linspace(0,t_run,N);                    %time array, [s]
66      dt = t(2) - t(1);                           %time step value, [s]
67      E_emt = zeros(size(t));                     %Field that leaves, [V/m]
68      J = zeros(size(t));                         %current density, [A/m^2]
69      nG = ones(size(t));                         %fraction of electrons in
            G-valley, [1]
70      vG = zeros(size(t));                        %average vel. of
           electrons in G-valley, [m/s]
71      vL = zeros(size(t));                        %average vel. of
           electrons in L-valley, [m/s]
72      MG = ones(size(t))*mG;                      %effective mass in G-
           valley, [Kg]
73      ML = ones(size(t))*mL;                      %effective mass in L-
           valley, [Kg]
74      en0 = 1.5*kb*T0;                            %thermal component of
           energy, [J]
75      enG = ones(size(t))*en0;                    %energy of an electron in
            the G-valley, [J]
76      enL = ones(size(t))*en0;                    %energy of an electron in
            the L-valley, [J]
77      pG = vG.*sqrt(2*mG*enG.*(1 + aG*enG));      %momentum of an electron
           in the G-valley, [Kgm/s]
78      pL = vL.*sqrt(2*mL*enL.*(1 + aL*enL));      %momentum of an electron
           in the L-valley, [Kgm/s]
79      rGL = zeros(size(t));                       %scatter rate from G-
           valley to L-valley, [1/s]
```

```
80      diff_pG = pG;                                   %force on electron in G-
           valley, [N]
81      diff_pL = pL;                                   %force on electron in L-
           valley, [N]
82      I_emt = zeros(size(t));                         %integral of emitted
           field w.r.t time, [Vs/m]
83      I_inc = zeros(size(t));                         %integral of emitted
           field w.r.t time, [Vs/m]
84
85      %% --  Begin Calculation  --
86
87      for j = 1:N
88          % calculate current and emitted field
89          J(j) = -e0*n_elec*(nG(j)*vG(j) + (1-nG(j))*vL(j));
90          E_emt(j) = (2*Y0*E_inc(j) - d_thick*J(j))/(Y0 + n*Y0);
91
92          % calculate mass/energy
93          MG(j) = mG*(1 + aG*(enG(j) - 1.5*kb*T0));
94          ML(j) = mL*(1 + aL*(enL(j) - 1.5*kb*T0));
95          enG(j) = ((sqrt(1+2*aG*pG(j)^2/MG(j))-1)/(2*aG))+1.5*kb*T0;
96          enL(j) = ((sqrt(1+2*aL*pL(j)^2/ML(j))-1)/(2*aL))+1.5*kb*T0;
97
98          %update momentum of G-valley (using RK4)
99          rGL(j) = inter_scattering(enG(j),enth,de,tGL);
100         tG = rGL(j);
101         diff_pG(j) = -e0*E_emt(j)-pG(j)*(1/tGG + tG);
102         k1 = dt*diff_pG(j);
```

```
103         k2 = dt*(-e0*E_emt(j)-(pG(j)+1/2*k1)*(1/tGG + tG));
104         k3 = dt*(-e0*E_emt(j)-(pG(j)+1/2*k2)*(1/tGG + tG));
105         k4 = dt*(-e0*E_emt(j)-(pG(j)+    k3)*(1/tGG + tG));
106         pG(j+1) = pG(j)+(1/6)*(k1+2*(k2+k3)+k4);
107
108         %update momentum of L-valley (using RK4)
109         tL = 1/tLG;
110         diff_pL(j) = -e0*E_emt(j)-pL(j)*(1/tLL + tL);
111         c1 = dt*diff_pL(j);
112         c2 = dt*(-e0*E_emt(j)-(pL(j)+1/2*c1)*(1/tLL + tL));
113         c3 = dt*(-e0*E_emt(j)-(pL(j)+1/2*c2)*(1/tLL + tL));
114         c4 = dt*(-e0*E_emt(j)-(pL(j)+    c3)*(1/tLL + tL));
115         pL(j+1) = pL(j)+(1/6)*(c1+2*(c2+c3)+c4);
116
117         %calculate velocties and fraction in G-valley
118         vG(j+1) = pG(j)/(mG*sqrt(1+(2*aG*pG(j)^2)/mG));
119         vL(j+1) = pL(j)/(mL*sqrt(1+(2*aL*pL(j)^2)/mL));
120         vd(j) = vG(j)*nG(j) + vL(j)*(1-nG(j));
121         nG(j+1) = nG(j)+dt/tLG-nG(j)*dt*(rGL(j)+1/tLG);
122
123         %calculate integrals
124 %         if(j > 1)
125 %             I_inc(j) = trapz(E_inc(1:j));
126 %             I_emt(j) = trapz(E_emt(1:j));
127 %         end
128     end
129     %% Linear fits to remove noise term
```

```
130     [I_inc] = running_integral(E_inc);
131     [I_emt] = running_integral(E_emt);
132
133
134     %% remove the extra value in each of these
135     pG = pG(1:end-1);
136     pL = pL(1:end-1);
137     vG = vG(1:end-1);
138     vL = vL(1:end-1);
139     nG = nG(1:end-1);
140
141     %% -- Generate Output structure --
142     Output.pG = pG;
143     Output.pL = pL;
144     Output.vG = vG;
145     Output.vL = vL;
146     Output.nG = nG;
147     Output.nL = 1-nG;
148     Output.E_emt = E_emt;
149     Output.I_inc = I_inc;
150     Output.I_emt = I_emt;
151     Output.enG = enG;
152     Output.enL = enL;
153
154     %% --  Plot  --
155     % Fields
156 %     figure(1)
```

```
157 %         plot(t*1e12,(E_inc./max(E_inc)), t*1e12, (E_emt./max(E_emt)),'
    LineWidth',1.5)
158 %         legend('E_{inc}','E_{emt}')
159 %         title('Emitted and Incidental Fields')
160 %         xlabel('Time [ps]')
161 %         ylabel('Field Strength [kV/cm]')
162 %     %Integrals
163 %     figure(2)
164 %         plot(t*1e12,(I_inc./max(I_inc)),t*1e12,(I_emt./max(I_emt)),'
    LineWidth',1.5)
165 %         legend('I_{inc}','I_{emt}')
166 %         title('Integral of Emitted and Incidental Fields w.r.t time')
167 %         xlabel('Time [ps]')
168 %         ylabel('Integral up to current time [kV ps/cm]')
169 %     %valley occupancy
170 %     figure(3)
171 %         plot(t*1e12,nG,t*1e12,1-nG,'LineWidth',1.5)
172 %         xlim([-t_run*1e12 *0.05,t_run*1e12])
173 %         legend('\Gamma - Valley','L -Valley','Location','northoutside
    ','orientation','horizontal')
174 %         title('Valley occupancy')
175 %         xlabel('Time [ps]')
176 %         ylabel('Occupancy fraction')
177 %     %velocities
178 %     figure(4)
179 %         plot(t*1e12,vG,t*1e12,vL,'LineWidth',1.5)
180 %         legend('\Gamma - Valley','L - Valley')
```

```
181 %         title('Valley velocities')
182 %         xlabel('Time [ps]')
183 %         ylabel('Velocity [m/s]')
184 %     %energies
185 %     figure(5)
186 %         plot(t*1e12,enG/e0,t*1e12,enL/e0,'LineWidth',1.5)
187 %         legend('\Gamma - Valley','L - Valley')
188 %         title('Valley energies')
189 %         xlabel('Time [ps]')
190 %         ylabel('Energy [eV]')
191 %
192
193     %% --- Fun Facts ---
194 %     disp(strcat({'Max. of emitted field: '},{num2str(max(E_emt)*1e-5)},
        {' kV/cm'}))
195 %     disp(strcat({'Max. of vG: '}, {num2str(max(vG))}, {' m/s'}))
196 %     disp(strcat({'Max. of vL: '}, {num2str(max(vL))}, {' m/s'}))
197 %     disp(strcat({'Integral of Einc: '},{num2str(I_inc(end))}))
198 %     disp(strcat({'Integral of Eemt: '},{num2str(I_emt(end))}))
199     %% --- Finish ---
200    % clear all
201 %     disp(' ')
202 %     disp('Done')
203
204 end
205 function y = inter_scattering(en,enth,b,tn120)
206     e0 = 1.60217653e-19;
```

```
207     %
            ------------------------------------------------------------------------

208     %smooth function:
209     %r12=A1(en1-enth)(en1-2b-enth)(en1+2b-enth)(en1-enth+b1)(en1-enth-b1)
            (en1-enth-b2)(en1-enth+b2)+r120/2
210     b1 = 0.1*e0;
211     b2 = 0.1*e0;
212     BB1 = (0.5/tn120)/((-3*b^3)*(-b-2*b1)*(3*b+2*b1)*(-b-2*b1-2*b2)*(3*b
            +2*b1+2*b2));
213     %
            ------------------------------------------------------------------------

214     if en <= (enth-b);    %b=0.57e0
215         y = 0;
216     else
217         if en >= (enth+b);
218              y = 1/tn120;
219         else
220            y = BB1*(en-enth)*(en-enth-2*b)*(en-enth+2*b)*(en-enth-2*b-2*
                  b1)*(en-enth+2*b+2*b1)*(en-enth-2*b-2*b1-2*b2)*(en-enth+2*b
                  +2*b1+2*b2)+0.5/tn120;
221         end
222     end
223 end
```

A.2.2 Fitting to dynamic Drude model

```
diff = 1;
Data_norm = E_LD./max(E_LD);
E_max = 160E+5;
E_min= 40E+5;
count = 0;

while diff>0.00005 && count<100
    count = count+1;
    Max_output = thin_film_1D(E_max,E_noise);
        E_emt_norm_max = Max_output.E_emt./max(Max_output.E_emt);
        I_max = Max_output.I_emt./max(Max_output.I_emt);
    Min_output = thin_film_1D(E_min,E_noise);
        E_emt_norm_min = Min_output.E_emt./max(Min_output.E_emt);
        I_min = Min_output.I_emt./max(Min_output.I_emt);
    diff_max = abs(min(Data_norm) - min(I_max));
    diff_min = abs(min(Data_norm) - min(I_min));
    if diff_max < diff_min
        E_min = abs(E_max+E_min)./2;
    else
        E_max = abs(E_max+E_min)/2;
    end
    diff = abs(diff_max-diff_min);
end


E_out = [E_emt_norm_max' E_emt_norm_min'];
```

```
27 E_out = mean(E_out,2);
28 E_out = E_out./max(E_out);
29 E_out = E_out(1:end);
30
31 I_out = [Max_output.I_emt Min_output.I_emt];
32 I_out = mean(I_out,2);
33 I_out = I_out./max(I_out);
34 I_out = I_out(1:end);
35
36 Mean.nG = mean([Max_output.nG' Min_output.nG'],2);
37 Mean.nL = mean([Max_output.nL' Min_output.nL'],2);
38 Mean.pG = mean([Max_output.pG' Min_output.pG'],2);
39 Mean.pL = mean([Max_output.pL' Min_output.pL'],2);
40 Mean.vG = mean([Max_output.vG' Min_output.vG'],2);
41 Mean.vL = mean([Max_output.vL' Min_output.vL'],2);
42 Mean.enG = mean([Max_output.enG' Min_output.enG'],2);
43 Mean.enL = mean([Max_output.enL' Min_output.enL'],2);
44
45 clear Max_output
46 clear Min_output
47 clear Output
48 clear E_min
49 clear I_max
50 clear I_min
51 clear Data_norm
52 clear diff_max
53 clear diff_min
```

```
54 clear diff
```

A.2.3 Drude fitting

```
function [Freq_fit_out,Sigma_one_fit_out,Sigma_two_fit_out,sigma_dc,tau]
    = Drude_fitter(sigma_one,sigma_two,freq)
%DRUDE_FITTER Summary of this function goes here
%   Detailed explanation goes here

%% Preamble setup

% Frequency vector: first half is for sigma_one, second half is for
% sigma_two

    freq = [freq freq];
    omega = freq.*2.*pi;

% Creating a single vector for sigma_one and sigma_two
    y = [sigma_one sigma_two];
        n1 = length(sigma_one);
        n2 = length(sigma_two);
        n = n1+n2;

%% Defining fun as the residual function between theory and measurement (
    y)

fun = @(fit_params)[fit_params(1).*fit_params(2)./(1+((omega(1:n1)).*
    fit_params(2)).^2) fit_params(1).*fit_params(2).*(omega(n1+1:n).*
    fit_params(2))./(1+((omega(n1+1:n)).*fit_params(2)).^2)]-y;

```

```
23 %% Fitting the function
24
25 % Initial guess
26     [max_y] = max(sigma_one);
27     initial_guess = zeros(1,2);
28     initial_guess(1) = 1.5.*max_y;
29     initial_guess(2) = 1./(0.85E+12);
30
31 % Fitting the function
32     fit_out = lsqnonlin(fun,initial_guess);
33
34 % Extracting the paramaters
35     sigma_dc = fit_out(1).*fit_out(2);
36
37 % since we do everything with f and not omega, tau -> tau/2pi which means
       we have to correct that
38 % We also correct for f -> f/1E+12 meaning tau-> tau/(2*pi*1E+12)
39     tau = fit_out(2);
40
41 % Creating the fit we want to export
42     Freq_fit_out = linspace(0,max(max(freq)),1000);
43     Sigma_one_fit_out = fit_out(1)./(1+((Freq_fit_out).*fit_out(2)).^2);
44     Sigma_two_fit_out = fit_out(1).*(Freq_fit_out.*fit_out(2))./(1+((
          Freq_fit_out).*fit_out(2)).^2);
45
46 % Quickly plotting the results just to be sure
```

```
47      Plotter(freq(1:n1),y(1:n1),Freq_fit_out,Sigma_one_fit_out,freq(n1+1:n
            ),y(n1+1:n),Freq_fit_out,Sigma_two_fit_out);
48
49
50  end
```

Appendix B

In-depth calculations

B.1 Intensity profile to electric field

Through use of a thermal imaging system, it is possible to characterise the intensity profile of a THz pulse.This characterisation can actually be quite useful in estimating the peak electric field of a THz pulse. The derivation is quite simple, and begins with the assumption that a THz pulse has an intensity profile of the form

$$I(r,t) = I_o e^{-2r^2/w^2} e^{-t^2/\tau^2}. \tag{B.1}$$

Where τ is a measure of the temporal width of a pulse. A THz pulse is typically around the 1ps time scale. Now the instantaneous power of this pulse can be found by integrating over the area

of the intensity profile in cylindrical coordinates.

$$\begin{aligned} P(t) &= \int I(r,t)dA \\ &= I_o e^{-t^2/\tau^2} \int_0^{2\pi}\int_0^{\infty} e^{-2r^2/w^2} dr d\phi \\ &= \frac{\pi w^2 I_o}{2} e^{-t^2/\tau^2} \end{aligned}$$

From this, an average power can be found, all that one needs to do is integrate over a symmetric time interval of length T.

$$\bar{P} = \frac{\pi w^2 I_o}{2}\frac{1}{T}\int_{-T/2}^{T/2} e^{-t^2/\tau^2} dt$$

This isn't generally integrable in terms of elementary functions, and so we make an assumption that the temporal profile of the pulse is extremely small compared to the time between pulses. This means that $T >> \tau$ and so T seems like an eternity compared to τ.[1]

$$\begin{aligned} \bar{P} &\approx \frac{\pi w^2 I_o}{2}\frac{1}{T}\int_{-\infty}^{\infty} e^{-t^2/\tau^2} dt \\ &= \frac{\pi^{3/2} w^2 I_o \tau}{2T} \end{aligned}$$

Now, given that I_o is defined as

$$I_o = \frac{1}{2} c\varepsilon_o |E_o|^2,$$

[1] This is a good assumption, since a THz pulse has an envelope on the order of 1ps, and the repetition time of the Legend amplifier is 1ms. The 9 orders of magnitude is what solidifies this assumption.

it is quite simple to show that the peak electric field is given by

$$|E_o| = \sqrt{\frac{4T\bar{P}}{\pi^{3/2} c\varepsilon_o w^2 \tau}} \tag{B.2}$$

but $\bar{P}T = E$, where E is the measured pulse energy, meaning that

$$|E_o| = \sqrt{\frac{4E}{\pi^{3/2} c\varepsilon_o w^2 \tau}} \tag{B.3}$$

B.2 Electro-optic sampling of THz electric fields

Jones calculus is a method that can be used to describe the changes in the polarization of light as it traverses a number of optical elements. The goal of this appendix is to use Jones calculus to develop a practical understanding of electro-optic sampling. We will be borrowing notation from [31], chapter 8.13.

Let us begin by envisioning a system where light is linearly polarized at a +45 degree angle between the x-y planes, and propagates in the z-direction. This light will travel with wave vector k, and has angular frequency ω such that the electric field components can be expressed as

$$\mathbf{E} = \begin{bmatrix} E_x \\ E_y \end{bmatrix} = \begin{bmatrix} 1 \\ 1 \end{bmatrix} E_o e^{ikz - i\omega t}$$

As far as the present situation is concerned, we need only worry about the relative phases induced by optical elements we are about to introduce. As such, we choose to normalize the intensity to unity, sacrificing information, but gaining simple expressions. Normalizing eqn. B.2 we obtain

$$\mathbf{E}_{\text{Jones}} = \begin{bmatrix} 1 \\ 1 \end{bmatrix} \frac{E_o}{\sqrt{2}}$$

In Jones calculus, one applies a transformation matrix to a Jones vector (through basic matrix multiplication) in order to determine the output electric field. I.e.

$$\mathbf{E}_{\text{Out}} = \mathbb{M}\mathbf{E}_{\text{Jones}} \tag{B.4}$$

In this formalism, $\mathbb{M}$ is a transformation matrix known as a Jones matrix. Every optical element will have its own Jones matrix.

If the linearly polarized light above is incident upon a horizontal polarizer, the output electric field can be readily calculated, provided that we know what the Jones matrix is for a linear polarizer. Some example Jones matrices are listed in table B.1 for reference. Thus, the output electric field would then be

$$\begin{aligned} E_{\text{Out}} &= \begin{bmatrix} 1 & 0 \\ 0 & 0 \end{bmatrix} \begin{bmatrix} 1 \\ 1 \end{bmatrix} \frac{E_o}{\sqrt{2}} \\ &= \begin{bmatrix} 1 \\ 0 \end{bmatrix} \frac{E_o}{\sqrt{2}}. \end{aligned}$$

With this, we can see that the output light is horizontally polarized - as expected. The mathematics is exactly the same if we introduce media that shift the phase of incident light, such as a quarter wave plate, half wave plate or a Kerr medium.

To handle the transmission through multiple optical elements, one needs only to left multiply the matrices for each optical element. For example, if we desired to find the transmission through 10 optical elements, we could simply write

$$\mathbf{E}_{\text{Out}} = \mathbb{M}_{10}\mathbb{M}_9 ... \mathbb{M}_2\mathbb{M}_1\mathbf{E}_{\text{Jones}} \tag{B.5}$$

Where $\mathbb{M}_{10}$ is the last element that interacts with the incident light, and $\mathbb{M}_1$ is the first.

Table B.1 A table of Jones Matrices

Optical element	Jones Matrix
Horizontal Linear Polarizer	$\begin{bmatrix} 1 & 0 \\ 0 & 0 \end{bmatrix}$
Vertical Linear Polarizer	$\begin{bmatrix} 0 & 0 \\ 0 & 1 \end{bmatrix}$
Electro-optic crystal (Vert. fast axis)	$\begin{bmatrix} 1 & 0 \\ 0 & e^{-i\Delta\phi} \end{bmatrix}$
Quarter wave plate (Horiz. fast axis)	$\begin{bmatrix} e^{i\pi/4} & 0 \\ 0 & e^{i3\pi/4} \end{bmatrix}$

Using this method, it is possible to obtain a relation for the intensity of the emitted light. The intensity of emitted light is proportional to the complex square of the Jones vector.

$$I_{\text{Out}} \propto \mathbf{E}^*_{\text{Out}}\mathbf{E}_{\text{Out}} \tag{B.6}$$

Using only the facts from above, we are able to gain describe electro-optic sampling. The goal of the following work is to come up with a formula that relates intensities that can be measured by balanced photodiodes, to the electric field experienced by an electro-optic crystal (E_{THz}).

To begin analyzing electro-optic sampling, we must determine the Jones matrix for a Pockel cell. A Pockel cell has 3 main components: an input polarizer (aligned to x or y) followed by an electro-optic crystal, which is filled by a final analyzer polarizer. The fast-axis of the electro-optic crystal will lie in the vertical direction, the transmission axis of the input polarizer is oriented at $+45^o$ with respect to the x-axis, and the analyzer polarizer rests at -45^o. In electro-optic sampling, we modify the Pockel cell by adding a quarter wave plate between the analyzer and the electro-optic crystal (fast axis is also vertical). light is linearly polarized and

incident at $+45^o$ with respect to the horizontal, and so the Jones vector for this system is

$$\mathbf{E}_{\text{In}} = \begin{bmatrix} 1 \\ 1 \end{bmatrix} \frac{E_o}{\sqrt{2}}$$

and the output electric field can be written as

$$\mathbf{E}_{\text{Out}} = (\mathbb{M}_{-45^o})(\mathbb{M}_{QWP})(\mathbb{M}_{E.O})(\mathbb{M}_{+45^o})\mathbf{E}_{\text{In}}.$$

The Jones matrices can be multiplied out as follows

$$\begin{aligned}
\mathbb{M}_{\text{Tot}} &= (\mathbb{M}_{-45^o})(\mathbb{M}_{QWP})(\mathbb{M}_{E.O})(\mathbb{M}_{+45^o}) \\
&= \left(\frac{1}{2}\begin{bmatrix} 1 & -1 \\ -1 & 1 \end{bmatrix}\right)\left(\begin{bmatrix} e^{i\pi/4} & 0 \\ 0 & e^{i3\pi/4} \end{bmatrix}\right)\left(\begin{bmatrix} 1 & 0 \\ 0 & e^{-i\Delta\phi} \end{bmatrix}\right)\left(\frac{1}{2}\begin{bmatrix} 1 & 1 \\ 1 & 1 \end{bmatrix}\right) \\
&= \frac{1}{4}\begin{bmatrix} 1 & -1 \\ -1 & 1 \end{bmatrix}\begin{bmatrix} e^{i\pi/4} & 0 \\ 0 & e^{i3\pi/4} \end{bmatrix}\begin{bmatrix} 1 & 1 \\ e^{-i\Delta\phi} & e^{-i\Delta\phi} \end{bmatrix} \\
&= \frac{1}{4}\begin{bmatrix} 1 & -1 \\ -1 & 1 \end{bmatrix}\begin{bmatrix} e^{i\pi/4} & e^{i\pi/4} \\ e^{i(3\pi/4-\Delta\phi)} & e^{i(3\pi/4-\Delta\phi)} \end{bmatrix} \\
&= \frac{1}{4}\begin{bmatrix} e^{i\pi/4} - e^{i(3\pi/4-\Delta\phi)} & e^{i\pi/4} - e^{i(3\pi/4-\Delta\phi)} \\ -(e^{i\pi/4} - e^{i(3\pi/4-\Delta\phi)}) & -(e^{i\pi/4} - e^{i(3\pi/4-\Delta\phi)}) \end{bmatrix} \\
&= \frac{e^{i\pi/4} - e^{i(3\pi/4-\Delta\phi)}}{4}\begin{bmatrix} 1 & 1 \\ -1 & -1 \end{bmatrix}
\end{aligned}$$

where $\Delta\phi$ is a phase induced by an electro-optic crystal. Therefore, $\mathbf{E}_{\text{Out}}$ is

$$\begin{aligned} E_{\text{Out}} &= \frac{e^{i\pi/4} - e^{i(3\pi/4-\Delta\phi)}}{4} \begin{bmatrix} 1 & 1 \\ -1 & -1 \end{bmatrix} \begin{bmatrix} 1 \\ 1 \end{bmatrix} \frac{E_o}{\sqrt{2}} \\ &= \frac{E_o}{\sqrt{2}} \left(\frac{e^{i\pi/4} - e^{i(3\pi/4-\Delta\phi)}}{4} \right) \begin{bmatrix} 2 \\ -2 \end{bmatrix} \end{aligned} \tag{B.7}$$

Referring to eqn. B.6, we can calculate the output intensity to be

$$\begin{aligned} I &\propto \frac{E_o^2}{2} \left(\frac{(e^{i\pi/4} - e^{i(3\pi/4-\Delta\phi)})(e^{-i\pi/4} - e^{-i(3\pi/4-\Delta\phi)})}{16} \right) \times 4 \times 2 \\ &= \frac{E_o^2}{4}(1 - e^{i\Delta\phi - i\pi/2} - e^{-i\Delta\phi + i\pi/2} + 1) \\ &= \frac{E_o^2}{2} \times \frac{2 - 2\cos(\Delta\phi - \pi/2)}{2} \\ &= E_o^2 \times \frac{1 - \cos(\Delta\phi - \pi/2)}{2} \\ &= \frac{I_o}{2} \times [1 - \sin(\Delta\phi)] \end{aligned}$$

More succinctly, the output intensity of the above described system is dependent on the phase induced by the electro-optic crystal as follows

$$I(\Delta\phi) = \frac{I_o}{2} \times [1 - \sin(\Delta\phi)]\,. \tag{B.8}$$

If one were to remove the quarter wave plate from the above set up, the intensity observed after the final analyzer would be

$$I(\Delta\phi) = \frac{I_o}{2}[1 - \cos(\Delta\phi)] = I_o \sin^2\left(\frac{\Delta\phi}{2}\right).$$

Therefore, introducing a quarter wave plate has shifted the output intensity function by $\pi/2$. The smallest $\Delta\phi$ that is expected from a phase change induced by an electro-optic crystal is $\Delta\phi = 0$. We can therefore use a Taylor series to approximate the intensity functions around the origin.

With a quarter wave plate present, we obtain the expansion

$$I(\Delta\phi) \approx I_o \left(\frac{1}{2} + \Delta\phi - \mathscr{O}(\Delta\phi^3) \right) \approx I_o \left(\frac{1}{2} + \Delta\phi \right) \tag{B.9}$$

and without the quarter wave plate we have

$$I(\Delta\phi) \approx I_o \left(\Delta\phi^2 - \mathscr{O}(\Delta\phi^4) \right) \approx I_o \Delta\phi^2. \tag{B.10}$$

When using the system with the quarter wave plate, a photodiode would detect an intensity variation that is proportional to the phase induced by the electro-optic crystal. In the lab, it is commonly referred as “E-mode", since the output modulations are proportional to a phase induced by the electro-optic crystal (more on this later). Removing the quarter wave plate, the output intensity is dependent on the square of the phase induced by the electro-optic crystal, and hence this system is commonly referred to as “E^2 mode".
If the analyzer polarizer is aligned vertically, one can show (through the same analysis as above) that the output intensity is then given by

$$I(\Delta\phi) = \frac{I_o}{2} \left[1 + \sin(\Delta\phi) \right]. \tag{B.11}$$

In experiment, a Wollaston prism can be used to separate the components of the light that exits the quarter wave plate. Doing so allows us to measure both the horizontal intensity (I_x) and the

vertical intensity (I_y) at the same time. To summarize,

$$\begin{cases} I_x = \frac{I_o}{2}(1-\sin(\Delta\phi)) \\ \\ I_y = \frac{I_o}{2}(1+\sin(\Delta\phi)). \end{cases} \tag{B.12}$$

Under the small angle approximation, these become

$$\begin{cases} I_x \approx \frac{I_o}{2}(1-\Delta\phi) \\ \\ I_y \approx \frac{I_o}{2}(1+\Delta\phi). \end{cases}$$

Therefore, by subtracting the two intensities above, we obtain a signal intensity $I_{\mathbf{sig}}$ that is directly proportional to the phase induced by an electro-optic crystal

$$I_{\text{Sig}} = \frac{I_o}{2}(1+\Delta\phi) - \frac{I_o}{2}(1-\Delta\phi) = I_o\Delta\phi. \tag{B.13}$$

In the laboratory, eqn. B.13 is referred to as the modulation ratio for a two-channel electro-optic sampling system. This is called two-channel because photodiodes are measuring I_x and I_y.

In an electro-optic crystal, the change in phase $\Delta\phi$ induced by transmission is related to an external electric field through a second order nonlinear polarization effect, called the Pockels effect [16]. In an electro-optic crystal such as ZnTe, it is possible to relate the change in phase ($\Delta\phi$) to the external field ($\mathbf{E}$) as follows [13, 16]

$$\Delta\phi = \frac{\omega L}{c} n_O^3 r_{41}\mathbf{E}, \tag{B.14}$$

where L is the crystal thickness, ω is the frequency of the light passing through the system (usually 800nm in our laboratory), c is the speed of light in vacuum, n_O is the index of refraction for ZnTe at 800nm, r_{41} is the electro-optic coefficient for ZnTe, and $\mathbf{E}$ is the applied external

electric field. Therefore, eqn. B.12 can be rewritten to include the external electric field

$$\begin{cases} I_x = \frac{I_o}{2}\left(1 - \sin\left(\frac{\omega L}{c} n_O^3 r_{41}\right)\right) \\ I_y = \frac{I_o}{2}\left(1 + \sin\left(\frac{\omega L}{c} n_O^3 r_{41}\right)\right). \end{cases} \tag{B.15}$$

Under the small angle approximation, we have

$$\begin{cases} I_x \approx \frac{I_o}{2}\left(1 - \frac{\omega L}{c} n_O^3 r_{41}\mathbf{E}\right) \\ I_y \approx \frac{I_o}{2}\left(1 + \frac{\omega L}{c} n_O^3 r_{41}\mathbf{E}\right). \end{cases}$$

From this, it is simple to show that

$$\frac{I_x - I_y}{I_o} = \frac{\omega L}{c} n_O^3 r_{41}\mathbf{E}. \tag{B.16}$$

Light is an electromagnetic wave. The electric field component of this wave can be used to induce phase modulations in the configuration described above. As such, by carefully synchronizing the arrival of two pulses of light, the electric field of one pulse (in this context a THz pulse) can modulate the phase of another pulse (usually 800nm, 50fs pulses). This produces a non-zero difference in $I_x - I_y$, which we can attribute to the instantaneous electric field of a THz pulse. By using a chopper, we can measure $I_o = I_x + I_y$ when no THz pulse is present, and $I_x - I_y$ when a THz pulse is present. We can now conclude by rewriting the equation above in terms of the electric field of a THz pulse $\mathbf{E}_{\mathrm{THz}}$

$$\frac{I_x - I_y}{I_x + I_y} = \frac{\omega L}{c} n_O^3 r_{41}\mathbf{E}_{\mathrm{THz}}. \tag{B.17}$$

B.3 Excited charge carriers

It is important to verify that the nonlinearity we seek is coming from intervalley scattering, and not from a the photoexcitation of free charge carriers. For example, the imaging beam typically has a power of

$$P_{\text{img}} < 10mW \tag{B.18}$$

In the strongest case, a maximum of 10mW illuminates our sample. From this we can estimate the number of charge carriers that are excited across the band gap, assuming that each photon in this bundle excites an electron-hole pair. If this number is reasonably small compared to the number of dopants (around $10^{18}cm^{-3}$), then we can conclude that these charge carriers will impose a negligible effect on the transient conductivity of the sample.

The number of photons in a pulse of light can be calculated from the power of the pulse through

$$N_{\text{Phot}} = \frac{\text{Power} \times \text{Rep. time}}{\text{Photon Energy}} = \frac{10mW \times 1ms}{1.55eV \times 1.6 \times 10^{-19}eV/J} = 4.03 \times 10^{13} \text{ Photons} \tag{B.19}$$

Since energy must be conserved, and photons carry finite amounts of energy, the number of photons that pass the interface is just the transmittance times the initial amount,

$$\begin{aligned} N_{\text{inside}} &= T \times N_{\text{Phot}} \\ &= 0.67 \times 4.03 \times 10^{13} \\ &= 2.70 \times 10^{13} \text{ Photons} \end{aligned} \tag{B.20}$$

where, the transmittance is given by

$$T = \frac{n_{\text{InGaAs}}}{n_{\text{air}}} \left[\frac{n_{\text{air}} + n_{\text{air}}}{n_{\text{air}} + n_{\text{InGaAs}}} \right]^2, \tag{B.21}$$

and $n_{\text{InGaAs}} = 3.2$. Imagine now that these photons occupy a cylinder within the sample, having dimensions of $1.5cm$ diameter (measured from the beam), and $500nm$ height (thickness of sample). This results in a photon density of

$$\begin{aligned} n_{\text{inside}} &= \frac{2.70 \times 10^{13}}{\pi(0.75cm)^2(500nm)} \\ &= 3.06 \times 10^{23} \frac{\text{Photons}}{m^3} \\ &= 3.06 \times 10^{17} \frac{\text{Photons}}{cm^3} \end{aligned} \tag{B.22}$$

If every one of these photons was to excite a charge carrier, then the total density of excited carriers is given by

$$n_e = 3.06 \times 10^{17} cm^{-3} \tag{B.23}$$

B.4 Nonlinear wave equation

This section is devoted to providing a focused discussion around optical rectification in a non-centrosymmetric medium. To begin, Maxwell's equations provide the foundation of the propagation of light in the presence of matter. Maxwell's equations are as follows.

$$\vec{\nabla} \cdot \mathbf{E} = \frac{\rho}{\varepsilon_o} \tag{B.24}$$

$$\vec{\nabla} \cdot \mathbf{B} = 0 \tag{B.25}$$

$$\vec{\nabla} \times \mathbf{E} = -\frac{\partial \mathbf{B}}{\partial t} \tag{B.26}$$

$$\vec{\nabla} \times \mathbf{H} = \mathbf{J_f} + \frac{\partial \mathbf{D}}{\partial t} \tag{B.27}$$

Where the electric field strength $\mathbf{E}$ and the magnetic field strength $\mathbf{H}$ change in the presence of a material that has some charge density ρ. The presence of this charge density forces us to define two new quantities, the electric displacement $\mathbf{D}$ and the magnetic induction $\mathbf{B}$, which are related to their free space counterparts by

$$\begin{aligned} \mathbf{B} &= \mu_o (\mathbf{H} + \mathbf{M}) \\ \mathbf{D} &= \varepsilon_o \mathbf{E} + \mathbf{P}. \end{aligned} \tag{B.28}$$

These equations come together to form the wave equation in matter. To begin, we note that the curl of Eq(B.26) gives

$$\vec{\nabla} \times \left(\vec{\nabla} \times \mathbf{E} \right) = -\vec{\nabla} \times \frac{\partial \mathbf{B}}{\partial t} \tag{B.29}$$

Given Eq(B.28), the time derivative of $\mathbf{B}$ can be defined as

$$\frac{\partial \mathbf{B}}{\partial t} = \mu_o \left(\frac{\partial \mathbf{H}}{\partial t} + \frac{\partial \mathbf{M}}{\partial t} \right). \tag{B.30}$$

The curl of Eq(B.30) thus results in (noting that $\mathbf{M} = 0$ in a material with no initial magnetic field)

$$\vec{\nabla} \times \frac{\partial \mathbf{B}}{\partial t} = \mu_o \vec{\nabla} \times \left(\frac{\partial \mathbf{H}}{\partial t} \right).$$

Rearranging the order of differentiation yields

$$\vec{\nabla} \times \frac{\partial \mathbf{B}}{\partial t} = \mu_o \frac{\partial}{\partial t} \left(\vec{\nabla} \times \mathbf{H} \right). \tag{B.31}$$

Assuming that there are no sinks or sources of current in the material through which the light propagates, we can assume that $\mathbf{J_f} = 0$ since $\rho_f = 0$. This means that Eq(B.27) has the form

$$\vec{\nabla} \times \mathbf{H} = \frac{\partial \mathbf{D}}{\partial t},$$

so that Eq(B.31) becomes

$$\vec{\nabla} \times \frac{\partial \mathbf{B}}{\partial t} = \mu_o \frac{\partial^2 \mathbf{D}}{\partial t^2}.$$

Up to a minus sign, this is the right hand side of Eq(B.29). Using a vector identity

$$\vec{\nabla} \times \left(\vec{\nabla} \times \mathbf{A}\right) = \vec{\nabla}\left(\vec{\nabla} \cdot \mathbf{A}\right) - \nabla^2 \mathbf{A},$$

Eq(B.29) has the form

$$\vec{\nabla}\left(\vec{\nabla} \cdot \mathbf{E}\right) - \nabla^2 \mathbf{E} = -\mu_o \frac{\partial^2 \mathbf{D}}{\partial t^2}, \tag{B.32}$$

Since there are no free charge carriers, $\rho = 0$, meaning that [13],

$$\nabla(\vec{\nabla} \cdot \mathbf{E}) = 0$$

so that Eq(B.32) becomes

$$-\nabla^2 \mathbf{E} = -\mu_o \frac{\partial^2 \mathbf{D}}{\partial t^2},$$

Using the electric displacement equation of Eq(B.28), we can see that the second order time derivative is

$$-\mu_o \frac{\partial^2 \mathbf{D}}{\partial t^2} = -\mu_o \varepsilon_o \frac{\partial^2 \mathbf{E}}{\partial t^2} - \mu_o \frac{\partial^2 \mathbf{P}}{\partial t^2}$$

so that we arrive at the final equation of an electromagnetic wave propagating through matter

$$\nabla^2 \mathbf{E} - \frac{1}{c^2} \frac{\partial^2 \mathbf{E}}{\partial t^2} = \mu_o \frac{\partial^2 \mathbf{P}}{\partial t^2} \tag{B.33}$$

where $c = 1/\sqrt{\varepsilon_o \mu_o}$ is the speed of light in free space. The right hand side of eqn. (B.33) behaves as a source term in the wave equation. Let's expand the polarization into linear and nonlinear terms as follows,

$$\nabla^2 \mathbf{E} - \frac{1}{c^2}\frac{\partial^2 \mathbf{E}}{\partial t^2} = \underbrace{\mu_o \frac{\partial^2 \mathbf{P}^{(1)}}{\partial t^2}}_{\text{Linear term}} + \underbrace{\mu_o \frac{\partial^2 \mathbf{P}_{\text{NL}}}{\partial t^2}}_{\text{Nonlin. term}} \tag{B.34}$$

This is the nonlinear wave equation. Its constituents are discussed in more detail in Chapter 2, with emphasis on the THz generation through optical rectification.